THE UNIVERSITY OF SHEFFIELD

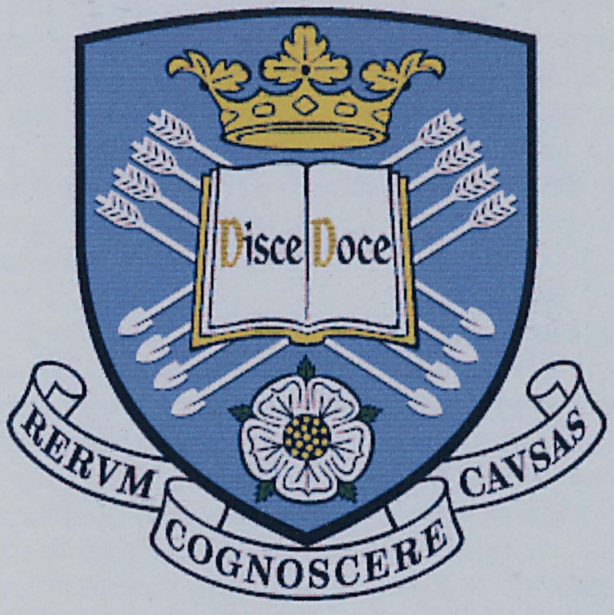

Advanced Transmission Electron Microscopy Studies of III-V Semiconductor Nanostructures

by

C. M. TEY

A thesis submitted for the degree of Doctor of Philosophy

Department of Electronic and Electrical Engineering

July 2006

Abstract

III-V semiconducting materials allow many novel optoelectronic devices, such as light emitting diodes and lasers, to be developed. Furthermore, recent development in crystal growth techniques allows the growth of low-dimensional semiconductor heterostructures. To achieve the best performance, the crystallinity and the growth mechanism of the devices have to be analysed. In this work, a JEOL JEM-2010F field emission gun transmission electron microscope (TEM) is employed to analyse the nanoscale semiconductor structures. Various techniques, such as conventional TEM, scanning TEM, high resolution TEM and energy-filtered TEM were employed to characterize the structural properties of III-V semiconducting materials.

In this thesis, advanced TEM analysis on InAs/GaAs quantum dots with InAlAs capping layer, GaInNAs/GaAs quantum wells and annealed low temperature-grown GaAs are presented. The former investigates the impact of varying the thicknesses of InAlAs in the combined two-level InAlAs-InGaAs capping layer on InAs/GaAs quantum dots. Based on the energy-filtered TEM images, the concentration of Al near the apex of the dots is significantly reduced. An increase in the height of the quantum dots has been observed when the thickness of InAlAs capping layer is increased. This is attributed to the suppression of indium atom detachment rate from the InAs dots during the capping process.

Effects of growth temperature on the structural properties of 1.6 μm GaInNAs/GaAs multiple quantum wells were also investigated. TEM studies show that compositional modulations and dislocations occurred in the sample grown at 400 °C and possible point defect formation in the sample grown at 350 °C. The photoluminescence intensities for samples grown at 350 and 400 °C are degraded dramatically, compared with the sample grown at 375 °C.

The effects of low temperature-growth GaAs annealed at different temperatures were systematically investigated by TEM. Along with other collaborative measurements, the arsenic precipitate parameters obtained from TEM images were employed to develop a semi-quantitative model based on Ostwald ripening to explain the precipitate formation. Furthermore, the "two-trap" model successfully explains the anomalous features in the carrier lifetime and resistivity trends in annealed low temperature-grown GaAs.

Acknowledgment

"I believe there is no philosophical high-road in science, with epistemological signposts. No, we are in a jungle and find our way by trial and error, building our road behind us as we proceed."
-- Max Born (1882-1970)

First and foremost, I would like to express my indebtedness and deepest gratitude to my supervisor, Prof A. G. Cullis for not only providing me the opportunity to undertake this degree, but also imparting his knowledge and wisdom. I would like to acknowledge and thank Dr. I. Ross and Dr. D. J. Norris for transferring their invaluable knowledge in electron microscopy techniques, especially Dr. I. Ross whose relentless enthusiasm has made me a better researcher.

Many thanks to Dr. I. S. Gregory from the University of Cambridge for his involvement and insights in the "annealed LT-GaAs" project. His work on XRD, TPRP and resistivity tests has been most helpful in formulating the "two-trap" model for arsenic precipitates. I would also like to thank Dr. H. Y. Liu for believing in my capabilities and collaborating with me in many projects. I am further indebted to the other staff in the EPSRC Central Facility, such as Dr. T. Wang, Dr. M. Hopkinson, Dr. G. Hill and Dr. A. Krysa, for their kind assistance and work discussions.

My sincere appreciation is extended to my colleagues and friends: San Lin, Fabio, Paolo, Isaac, Rob, Wei Sin, Marina, Yang Qiu and Dave. Without their companionship and support, I would have been unable to finish this thesis. Mr. A. Walker's contribution in ensuring smooth operation in the sample preparation room and the TEM room has been most appreciated. I would also like to thank Mrs. H. Levesley for her efficient secretarial support and the staff of the Sorby Centre for their assistance.

Finally, this thesis is dedicated to my family, who have supported and encouraged me over the years (as well as encouraging me to complete my thesis).

Published Work

1. *Effects of growth temperature on the structural and optical properties of 1.6 μm GaInNAs/GaAs multiple quantum wells*, H. Y. Liu, **C. M. Tey**, C. Y. Jin, S. L .Liew, P. Navaretti, M. Hopkinson, and A. G. Cullis, Appl. Phys. Lett., **88** (2006) 191907.
2. *Two-trap model for carrier lifetime and resistivity behavior in partially annealed GaAs grown at low temperature*, I. S. Gregory, **C. M. Tey**, A. G. Cullis, M. J. Evans, H. E. Beere, and I. Farrer, Phys. Rev. B., **73** (2006) 195201.
3. *Structural studies of a combined InAl-InGaAs capping layer on 1.3 μm InAs/GaAs quantum dots*, **C. M. Tey**, H. Y. Liu, A. G. Cullis, I. M. Ross, and M. Hopkinson, J. Cryst. Growth, **285** (2006) 17.
4. *Mechanism for improvements of optical properties of 1.3-mu m InAs/GaAs quantum dots by a combined InAlAs-InGaAs cap layer*, H. Y. Liu, **C. M. Tey**, I. R. Sellers, T. J. Badcock, D. J. Mowbray, M. S. Skolnick, R. Beanland, M. Hopkinson, A. G. Cullis, J. Appl. Phys., **98** (2005) 083516.
5. *Structural analysis of the effects of a combined InAlAs-InGaAs capping layer in 1.3 μm InAs quantum dots*, **C. M. Tey**, A. G. Cullis, H. Y. Liu, I. M. Ross, and M. Hopkinson, Proc. Microsc. of Semiconducting Mat. 2005 Springer Press **107** (2005) 261.
6. *Influence of In composition on the photoluminescence emission of In(Ga)As quantum dot bilayers*, M. A. Migliorato, M. J. Steer, W. M. Soong, **C. M. Tey**, H. Y. Liu, S. L. Liew, P. Navaretti, D. J. Norris, A. G. Cullis, M. Hopkinson, Physica E, **26** (2005) 124.
7. *High-performance distributed feedback quantum cascade lasers grown by metalorganic vapor phase epitaxy*, R. P. Green, L. R. Wilson, E. A. Zibik, D. G. Revin, J. W. Cockburn, C. Pflugl, W. Schrenk, G. Strasser, A. B. Krysa, J. S. Roberts, **C. M .Tey**, A. G. Cullis, Appl. Phys. Lett., **85** (2004) 5529.
8. *MOVPE grown quantum cascade lasers: Single mode performance and structural quality*, R. P. Green, L. R. Wilson, D. G. Revin, E. A. Zibik, J. W. Cockburn, A. B. Krysa, **C. M. Tey**, J. S. Roberts, A. G. Cullis, C. Pflugl, W. Schrenk, G. Strasser, P. Offermans, P. M. Koenraad, J. H. Wolter, 2005 Conf. on Lasers & Electro-optics (CLEO), **1-3** (2005) 254.

List of Contents

Abstract i

Acknowledgement ii

Published Work iii

List of Contents iv

Chapter 1: Introduction 1

1.1 Contribution of transmission electron microscopy 1

1.2 Objectives of the work 2

1.3 Outline of thesis 4

1.4 References 5

Chapter 2: Literature review 6

2.1 Historical Development of LT-GaAs 6

2.2 LT-GaAs devices 7

2.3 Growth and structural properties of LT-GaAs 8

2.3.1 Structural properties of LT-GaAs 8

2.3.2 MBE GaAs growth processes 9

2.3.2.1 Introduction to MBE 9

2.3.2.2 MBE GaAs growth dynamics 10

2.4 Excess arsenic in as-grown LT-GaAs 12

2.4.1 Antisite defects 13

2.4.2 Gallium vacancies 13

2.4.3 Interstitial defects 13

2.5 Introduction of GaInNAs material system 14

2.6 Growth and structural properties of GaInNAs 16
2.6.1 Material properties of GaInNAs 16
2.6.2 GaInNAs epitaxial growth techniques 17
2.7 Difficulties with GaInNAs 18
2.8 Introduction of QDs 19
2.9 Development of quantum dot heterostructure lasers and other applications for quantum dots 23
2.10 Fabrication techniques for quantum dots 24
2.10.1 The lithographic patterning and etching techniques 24
2.10.2 Self-organized growth of QDs 25
2.11 References 29

Chapter 3: Transmission Electron Microscopy 37

3.1 Introduction 37
3.2 The structure of TEM 39
3.2.1 Electron Sources 39
3.2.2 The condenser system 42
3.2.3 The specimen chamber 43
3.2.4 The objective and intermediate lenses 44
3.2.5 The projector and the display system 45
3.3 Aberrations in microscopy 46
3.3.1 Spherical aberration 46
3.3.2 Chromatic aberration 48
3.3.3 Astigmatism 49
3.4 Preparation of TEM specimens 49
3.4.1 Plan view specimen 50
3.4.2 Cross-sectional specimen 52
3.5 Ion milling 54
3.6 TEM imaging and spectroscopy 57

3.6.1 Diffraction patterns 58
3.6.2 Conventional transmission electron microscopy 59
3.6.3 High resolution transmission electron microscopy 61
3.6.4 Scanning transmission electron microscopy 64
3.6.5 Electron energy loss spectroscopy and energy filtered transmission electron microscopy 67
3.7 References 70

Chapter 4: Structural studies of InAlAs-InGaAs capping layer on InAs/GaAs quantum dots with 1.3-μm emission 74
4.1 Introduction 74
4.2 Experimental procedure 77
4.3 Results and discussion 79
4.3.1 HAADF-STEM results 79
4.3.2 EFTEM results 84
4.3.3 Surface chemical potential model 87
4.3.4 PL results 90
4.4 Conclusions 92
4.5 References 92

Chapter 5: Influence of growth temperature on near 1.55-μm GaInNAs/GaAs multiple quantum well 97
5.1 Introduction 97
5.2 Experimental procedure 98
5.3 Results and discussion 100
5.3.1 PL results 100
5.3.2 XRD results 102
5.3.3 CTEM results 103

5.3.4 BF/HAADF STEM results 105
5.3.5 HRTEM results 108
5.4 Conclusions 110
5.5 References 111

Chapter 6: Two-trap model for precipitate formation in partially-annealed low-temperature-grown GaAs 114

6.1 Introduction 114
6.2 The two-trap model 115
6.3 Experimental procedure 118
6.4 Results and discussion 123
6.4.1 XRD results 123
6.4.2 TEM results 125
6.4.3 Time resolved photoreflectance results 132
6.4.4 Resistivity test 134
6.5 Conclusion 135
6.6 References 136

Chapter 7: Conclusions and Outlook 139

7.1 Conclusions 139
7.2 Suggestions for future work 142
7.3 References 144

Chapter 1

Introduction

1.1 Contribution of transmission electron microscopy

The constant demand for faster, denser, lower power-consuming and more reliable semiconductor devices is driving the microelectronic and optoelectronic semiconductor world. In order to achieve better performance, semiconductor growth technology and lithography are used to facilitate the miniaturization of electronic devices, with dimensions down to the nanoscale. For further development to be achieved, a detailed understanding of semiconductor structural properties is essential. In order to achieve that, it is essential to exploit the various transmission electron microscopy techniques to conduct nanoscale analysis of materials using the highest spatial resolution.

In this work, the samples were examined using a JEOL JEM-2010F FEGTEM. Using the high resolution TEM (HRTEM) technique, high instrumental resolution (~0.19 nm) is achievable to provide information on the atomic scale and regarding strain fields. Conventional TEM (CTEM) techniques, such as bright field (BF) and dark field (DF) TEM imaging can be used to characterize various properties of the semiconductor material. For example, DF images using the (002) diffraction condition can be used to determine composition whereas (220) BF images can used to image the strain field of a cross-sectional sample. By tilting a cross-sectional specimen to allow imaging under the DF (113) diffraction condition, the density of quantum dots in individual layers can be measured. Scanning TEM (STEM) with attached detectors collects scattered electrons to produce diffraction contrast images or atomic number (Z)-contrast images. Electron energy loss spectroscopy (EELS) and energy dispersive x-ray spectroscopy (EDX) can be applied for compositional

analysis. Energy-filtered TEM (EFTEM) and X-ray mapping can also be used to provide a two-dimensional compositional map.

1.2 Objectives of the work

Although much research has been conducted, III-V semiconductor technology will continue to be a dynamic field with the advent of new device physics and growth technologies, coupled with new device fabrication techniques. The aim of this thesis is to investigate the structural properties of different types of III-V semiconductor material using various TEM techniques. Along with collaborative optical and/or electrical experimental results, novel ideas regarding the growth mechanism are presented.

In this work, three different III-V semiconductor material systems are investigated: InAs/GaAs quantum dots (QDs) with an InAlAs capping layer, GaInNAs/GaAs quantum wells (QWs) and annealed low temperature-growth GaAs (LT-GaAs).

Indeed, investigations on self-assembled InAs/GaAs QDs grown via the Stranski-Krastanow growth mode have been extensively carried out. This is mainly spurred by the prospect of three-dimensional confinement of carriers in order to improve the performance of lasers with 1.3 μm emission wavelength. The deposition of an InGaAs capping layer onto QDs is designed to achieve the desired wavelength of 1.3 μm while preserving the QD size [1]. Nonetheless, the InGaAs capping layer reduces the confinement potential, and hence reducing the energy separation between the discrete energy levels of the QDs [2]. As a result, a combined InAlAs-InGaAs capping has been devised to rectify the detrimental effect. Optical studies show that the photoluminescence (PL) intensity of 1.3 μm InAs/GaAs QDs is increased tremendously when the InAlAs capping layer thickness is increased from 1.5 to 6.0 nm. However, the precise origin of optical improvements due to the Al-containing capping layer have been unclear: several alternative models have previously been proposed [3-5]. This present study aims to use various TEM techniques, such as STEM and EFTEM, to qualitatively

determine the size of QDs and the distribution of elemental compositions. Based on the obtained TEM results, it aims to investigate the growth mechanism of the Al-containing capping layer.

Traditionally, the InP-based material system has been used for devices operating at the 1.3-μm and 1.55-μm emission wavelengths. However, the material system has the disadvantages of high threshold current and relatively low characteristic temperature T_o due to poor carrier confinement [6]. Hence, nitrogen-containing GaAs-based III-V alloys, such as GaInNAs quantum wells have been proposed to solve this problem because an increasing N content results in a systematic red-shift of the band-edge luminescence [7]. However, the crystal quality of GaInNAs material deteriorates dramatically with increasing N content due to the large miscibility gap which leads to phase separation [8]. To avoid phase separation, the GaInNAs quantum wells are grown at a lower growth temperature. Since no in-depth structural analysis has been conducted, this work aims to investigate the effects of growth temperature on the structural properties of 1.55-μm emission GaInNAs quantum wells, using CTEM, STEM and HRTEM. Based on the experimental results, the most probable growth mechanism for the structure is presented.

Growth at low temperature of GaAs suppresses the out-diffusion of arsenic, allowing an excess to be incorporated. As a result, the excess arsenic may be present as point defects [9]. Although as-grown LT-GaAs has an extremely low carrier lifetime (~90 ps) due to the rapid trapping of carriers, the material tends to have a low resistivity. As both characteristics are necessary for the implementation of photoconductive devices, the low resistivity problem is overcame by annealing the LT-GaAs material, thus creating arsenic precipitates due to point defect migration. Typically, the annealing process is conducted at a high temperature of approximately 600 °C: this is a temperature regime where the resistivity of the material is increased dramatically but the trapping lifetime is deteriorated significantly. Consequently, there is a lack of experimental and theoretical work on "partially-annealed" LT-GaAs where point defects co-exist with arsenic precipitates. The aim of this work is to present a quantitative model of the effects of point defects and precipitates based on experimental results. A

series of LT-GaAs samples annealed at different temperatures are analysed by TEM along with other complementary methods: MBE growth (University of Cambridge), X-ray diffraction (XRD), time-resolved photoreflectance (TRPR), and resistivity tests (Teraview Ltd.).

1.3 Outline of thesis

This thesis is organized into seven chapters as outlined below:

Chapter 2 gives a literature review covering the materials investigated in this thesis. It is separated into three main sections. The first section gives an introduction to the development of LT-GaAs and associated devices, along with a brief description of the molecular beam epitaxy (MBE) growth. The second section gives an overview of the GaInNAs material system. The last section summarizes the development, the physics and the fabrication techniques of QDs.

Chapter 3 is also separated into three main sections. The first section briefly reviews the physical structure of TEM and the aberrations and imperfection of TEM lenses. The second section describes the TEM sample preparation procedures. Lastly, the third section covers the various techniques of TEM imaging and spectroscopy.

Chapter 4 is dedicated to the structural analysis of InAs/GaAs QD samples with different InAlAs capping layer thicknesses. STEM imaging is conducted to obtain Z-contrast images of the QDs. Furthermore, EFTEM imaging has also been applied to qualitatively map the Al distribution in the vicinity of the QDs. From the observations, a growth mechanism based on the surface chemical potential of the Al-containing capping layer is proposed. The problems associated with using CTEM and HRTEM for compositional analysis of QDs are also discussed.

Chapter 5 reports a structural study on GaInNAs/GaAs multiquantum wells (MQWs) with different growth temperatures. Results from the XRD and PL

measurements are compared with the TEM images. CTEM, STEM and HRTEM images are obtained to investigate the interface sharpness and crystallinity of the grown heterostructures.

In **Chapter 6**, a series of LT-GaAs samples systematically annealed at different temperatures are analysed. This work introduces a semi-quantitative model for "partially-annealed" LT-GaAs samples based on experimental results from TEM images, XRD, TRPR, and resistivity tests.

Chapter 7 summarises the results and conclusions for the thesis and suggests some further research areas as a potential continuation of the present work.

1.4 References

[1] K. Nishi, H. Saito, S. Sugou, Appl. Phys. Lett., **74** (1999) 1111.

[2] K. Mukai, Y. Nakata, K. Otsubo, M. Sugawara, N. Yokohama, and H. Ishikawa, Appl. Phys. Lett., **76** (2000) 3349.

[3] M. Arzberger, U. Käsberger, G. Bőhm, and G. Abstreiter, Appl. Phys. Lett., **75** (1999) 3968.

[4] F. Ferdos, S. M. Wang, Y. Q. Wei, M. Sadeghi, Q. X. Zhao, A. Larsson, J. Cryst. Growth, **251** (2003) 145.

[5] A. F. Tsatsul'nikov, A. R. Kovsh, A. E. Zhukov, Yu. M. Shernyakov, Yu. G. Musikhin, V. M. Ustinov, N. A. Bert, P. S. Kop'ev, Zh. I. Alferov, A. M. Mintairov, J. L. Merz, N. N. Ledentsov, and D. Bimberg, J. Appl. Phys., **88** (2000) 6272.

[6] H. Temkin, D. Coblentz, R. A. Logan, J. P. Van der Ziel, T. Tanbun-Ek, R. D. Yadvish, and A. M. Sergent, Appl. Phys. Lett., **62** (1993) 2402.

[7] M. Kondow, K. Uomi, A. Niwa, T. Kitatani, S. Watahiki, and Y. Yazawa, Jpn. J. Appl. Phys., **35** (1996) 1273.

[8] I. A. Buyanova, W. M. Chen, G. Pozina, J. P. Bergman, B. Monemar, H. P. Xin, and C. W. Tu, Appl. Phys. Lett., **75** (1999) 501.

[9] X. Liu, A. Prasad, J. Nishio, E. R. Weber, Z. Liliental-Weber, and W. Walukiewicz, Appl. Phys. Lett., **67** (1995) 279.

Chapter 2

Literature Review

This chapter is organized in three major sections. In **Section (I)**, an introduction on the development of and devices based on LT-GaAs is described. After an introduction on the structural properties of LT-GaAs, the MBE epitaxial growth technique is briefly explained. Likewise, **Section (II)** gives an introduction on the material properties of the GaInNAs material system, before describing the epitaxial growth techniques and its difficulties. In **Section (III)**, an introduction on the historical development of QDs and the physics of quantum confinement is described, prior to a summary of QD fabrication techniques.

(I) LT-GaAs

2.1 Historical Development of LT-GaAs

MBE GaAs is generally grown at a substrate temperature of $T_s \sim 580\text{-}600\ ^{\circ}C$ because this condition produces material with high concentration of shallow donor and acceptor, while greatly reducing the number of deep donors (at least an order of magnitude) [1]. But since the late 1970s, attempts have been made to grow MBE GaAs at temperatures lower than the usual growth temperature. The motivation for use of a lower growth temperature includes the increase of the concentration of deep traps [2], and the production of more efficient and abrupt Si-doping [3, 4]. Low temperature MBE GaAs (LT-GaAs) was first described by Murotani *et al.* in 1978, and subsequently used as a highly resistive buffer layer beneath a GaAs power field effect transistor (FET) [5]. However, the use of LT-GaAs as buffer layer is fraught with difficulties. The epitaxial GaAs channel layer is shown non-conducting due to defect diffusion from the LT-GaAs

buffer layer [6], whereas Metze and Calawa demonstrated an abrupt decrease of carrier mobility when $T_G < 500$ °C at normal growth rate [3].

In 1988, Smith *et al.* [7] published a widely regarded paper which demonstrated that backgating/sidegating effects and light sensitivity in GaAs metal-semiconductor FETs (MESFETs) can be eliminated by employing LT-GaAs grown at 200 °C and annealed at 600 °C as a buffer layer. Soon after, Smith *et al.* [8] also demonstrated the first reported use of LT-GaAs for photoconductive applications. A response time of 1.6 ps was cited, while no PL was observed. Yin *et al.* have utilized LT-GaAs on top of the MESFET structure where the high trap density of LT-GaAs reduces the surface fields of the FET, suppresses gate leakage, and significantly increases the gate-drain breakdown voltage [9]. The breakdown field was seen to increase from 80 $kVcm^{-1}$ to 320 $kVcm^{-1}$ as the growth temperature decreases from 300 °C to 200 °C, compared to 10 $kVcm^{-1}$ for SI-GaAs [10]. This property of as-grown LT-GaAs suggests useful applications as an insulator for FETs or enhancement of the performance of power devices.

2.2 LT-GaAs devices

As mentioned earlier, the used of LT-GaAs as a buffer layer has been shown to reduce "backgating" for MESFET and other heterostructure FET devices. Furthermore, parasitic source-drain current between the buffer-substrate regions is greatly reduced. As a result, fabrication of large-scale integrated circuits is possible. The use of LT-GaAs as a passivation layer on top of the active channel has greatly increased the breakdown voltage and saturation current, and produces better high power FETs [9]. MBE LT-GaAs is also a promising material for ultrafast photoconductive switches [11] and broad-band photodetectors (PDs) [12], as well as tunable sources of terahertz radiation by photomixing [13]. The dynamic behaviour of these devices is based on the non-stoichiometric nature of

LT GaAs accompanied with a high concentration of traps resulting in low carrier lifetime.

2.3 Growth and structural properties of LT-GaAs

2.3.1 Structural properties of LT-GaAs

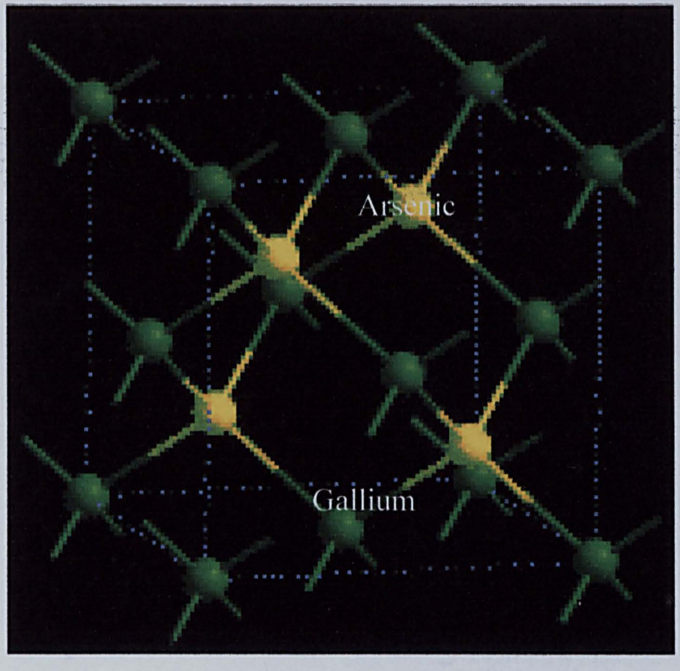

Fig. 2.1 Zinc-blende crystal structure of GaAs, where the yellow atoms are arsenic, whereas the green ones are gallium atoms.

GaAs is a III-V compound semiconductor and its crystal structure is the cubic sphalerite (zinc-blende) lattice, as shown in Fig 2.1, with mutually interpenetrating face-centred cubic lattices of Ga and As [14]. Ideally, GaAs has a 50:50 atomic ratio of Ga and As, with a characteristic lattice parameter of 5.65 Å [15]. However, growth at temperatures significantly below the usual 600 °C results in the suppression of out-diffusion of arsenic (non-stoichiometric growth), allowing an excess to be incorporated. Kaminska *et al.* have observed that LT-GaAs contains as much as 1.0-1.5 % excess arsenic and has a 0.5 % lattice expansion for as-grown LT-GaAs [16, 17]. It was mentioned that adjusting the

Ga:As ratio away from the stoichiometric compound introduces point defects. The excess arsenic in as-grown LT-GaAs manifests inself as three distinct types of point defects: the Ga vacancy (V_{Ga}), the arsenic antisite (As_{Ga}) and the arsenic interstitial (As_i) [18]. Details of these point defects are further explained in Section 2.4. For growth temperatures below 190 °C, Liliental-Weber *et al.* has shown that pyramidal defects with polycrystalline cores surrounded by microtwins, dislocations and stacking faults are formed if a critical thickness is exceeded [19].

2.3.2 MBE GaAs growth processes

2.3.2.1 Introduction to MBE

MBE is a technique for epitaxial growth via the interaction between atomic or molecular beams on a heated crystalline substrate surface in ultra-high vacuum (UHV) conditions. There are many variants of MBE techniques, differentiated mainly by their sources. However, typically MBE employs the molecular flow regime, using solid sources. A more complete description of the MBE growth is available from Ref [20, 21] and references therein. Hence, only a brief outline is shown below. Generally, the basic elements of an MBE deposition system are: a UHV growth chamber, a vacuum interlock arrangement (buffer section), a substrate holder and a set of effusion cells containing materials to be deposited.

The UHV growth chamber has a rotating substrate holder to produce uniform epitaxial growth across the wafer surface. The base pressure of the growth chamber, which is maintained by ion- or cryo-pumps, is typically $\sim 10^{-10}$ torr. Individual elemental beams are formed in heated Knudsen effusion cells, in which the inner crucible is made of pyrolytic boron nitride. The beam intensities are controlled by the cell temperatures and are constantly monitored by ion gauges. Most MBE systems are equipped with electro-pneumatically driven shutters which allow abrupt changes in composition or doping level to be

produced. The buffer interlock system is involved in the preparation and storage of the wafers before entering the growth chamber without breaking the vacuum. Here, the substrate can be placed on a heated stage to desorb gases and water vapour before being loaded into the UHV growth chamber.

Because of the ultrahigh vacuum environment of the MBE growth, a number of diagnostic techniques can be used to monitor various stages of the processes. The vacuum quality can be monitored with a mass spectrometer, the total pressure in the system can be measured with a Bayert-Alpert ion gauge, and a second such gauge placed in the substrate position can be used to quantify the flux of atoms from the Knudsen cells [21]. The growth rate (typically between 0.1 and 10 $\mu m hour^{-1}$) and surface structure may be monitored *in situ* by reflection high energy electron diffraction (RHEED). The RHEED system comprises a 10-15 keV electron gun on one side of the growth chamber aligned at glancing angle to the substrate, with a phosphor screen on the other side. The diffraction patterns produced are related to the surface structure and morphology of the substrate or deposited layers. For example, streaks indicate surface planarity, whereas spots indicate three-dimensional surface structures. Using RHEED, the patterns can be used to detect the desorption of volatile oxides during substrate heat cleaning, the presence of three dimensional growth mode, the growth rate, and the occurrence of "surface reconstruction".

2.3.2.2 MBE GaAs growth dynamics

The growth dynamics of MBE GaAs can be described in four stages: the adsorption of atoms or molecules to the substrate surface, surface migration and dissociation, incorporation into the lattice sites, and the thermal desorption of residual species [15]. Source materials are usually elemental and all group III elements, i.e. Ga, produce monatomic beams. An arsenic flux comprises either As_2 dimer or As_4 tetramer molecules. When evaporation happens directly from the heated elemental source, the arsenic flux consists entirely of tetratomic

molecules. Dimers are produced either by evaporation of appropriate III-V compounds or by using a two-zone Knudsen cell to dissociate As_4 to As_2 molecules [22, 23]. Arthur reported that at normal growth temperature of ~600°C, there was no desorption of Ga at the GaAs surface and the sticking coefficient of Ga was close to unity [24]. The adsorption process of Ga is generally independent of the substrate temperature. The stoichiometry of GaAs is generally kinetically controlled by the characteristics of the arsenic flux and the rate of growth is controlled by the Ga flux [24].

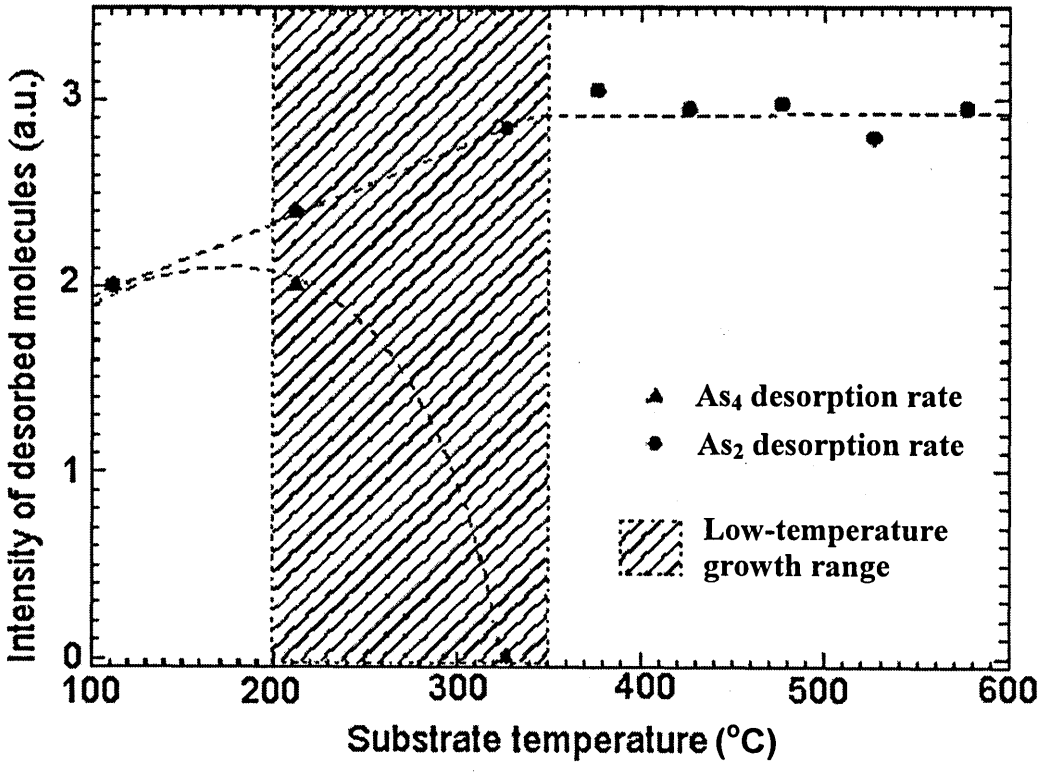

Fig. 2.2 Relative desorption rate of As_2 and As_4 for an incident As_2 flux as a function of growth temperature [25]. Low temperature growth occurs when the As_2 desorption rate falls from saturation and is indicated in the hatched region.

The dimer As_2 molecules are absorbed onto the Ga-rich GaAs surface in a mobile, weakly bound precursor state. The basic process for As_2 incorporation during epitaxial growth is a simple first-order dissociative chemisorption on

surface Ga atoms. The maximum value of the As_2 sticking coefficient is unity when the surface is covered with a complete monolayer of Ga atoms [24, 25]. Foxon and Joyce [25] state that the sticking coefficient of incident As_2 increases with increasing temperature and is also dependent on the surface Ga adatom population. The desorbed As_2 molecules from the surface are made up of either from the dissociation of GaAs or from incident As_2 molecules not chemisorbed. Below ~330 °C, some incident As_2 molecules can combine on the growth surface to form As_4 before desorbing as shown in Fig. 2.2 Conventional MBE growth at temperatures ~600 °C has a relatively high desorption rate. However, Fig. 2.2 shows that the desorption rate for As_2 molecules decreases when the temperature falls below 350 °C. This may be regarded as the threshold for low temperature growth.

The mechanism for the adsorption of As_4 molecules is more complex and is explained by the pair-wise dissociation of As_4 molecules chemisorbed on adjacent Ga atoms [21]. From any two As_4 molecules, both molecules are dissociated to allow four As atoms to become incorporated into the lattice, while the other four As atoms desorb as an As_4 molecule. Hence, the maximum sticking coefficient of As_4 never exceeds 0.5 [26]. The growth process is determined by both the growth temperature and the incident As_4 flux.

2.4 Excess arsenic in as-grown LT-GaAs

The structural and electronic data of dominant defects in LT-GaAs grown by MBE have been extensively characterized. MBE GaAs grown at 200 °C has an excess arsenic concentration of 1%-2%, as detected by Auger electron spectroscopy (AES) [27] and x-ray diffraction [16, 17].The excess arsenic is redistributed and manifested into several different forms: Ga vacancy (V_{Ga}), arsenic antisite (As_{Ga}), arsenic interstitial (As_i) and small complexes of these defects. A brief overview of the point defects is presented below.

2.4.1 Antisite defects

The first solid evidence of the presence of arsenic antisite (As_{Ga}) defects was the observation from the electron paramagnetic resonance four-line spectrum and the concentration observed is ~5 x 10^{18} cm^{-3} [17]. As_{Ga} defects occur when arsenic atoms occupy gallium lattice sites. The antisite defects essentially behave as deep level donors similar to EL2 (i.e. second electron level in the bandgap) defects in SI-GaAs crystals [28]. These have an energy level approximately 0.75 eV above the valence band edge [29]. The ionised defects have a large cross section for trapping electrons and may trap electrons from the conduction band to become neutral.

2.4.2 Gallium vacancies

Gallium vacancies (V_{Ga}) in as-grown LT-GaAs can be observed from the S-parameter characteristic of the annihilation γ-ray spectrum [30] and positron annihilation studies [31]. The positron annihilation study by Bliss *et al.* gave an excess V_{Ga} concentration in the order of 10^{19} cm^{-3} [31]. Gallium vacancies act as shallow acceptors, situated approximately 0.3 eV above the valance band edge [32]. Furthermore, V_{Ga} provides a mechanism for the diffusion of As_{Ga} antisites according to the vacancy-assisted diffusion model proposed by Bliss *et al.* [33].

2.4.3 Interstitial defects

The presence of arsenic interstitials (As_i) in LT-GaAs is still under dispute. Modelling work by Chen *et al.* shows that a significant proportion of excess arsenic, which results in the increase of lattice parameter in LT-GaAs, is attributed to As_i couples, instead of As_{Ga} [34]. Indeed, particle-induced x-ray emission and ion channelling measurements confirmed the presence of As_i and that As_i defects lie close to the arsenic lattice sites [35]. However, first principle calculations show that the formation energy of the As_i defect is several electron

volts higher than that of the As_{Ga} defect, meaning that As_i should exist in negligible amount in LT-GaAs [36]. In any case, the ionisation energy for As_i defects is relatively large, compared to other defect types; hence they are unlikely to play a significant role in electron trapping.

Although As_i may not be electrically active, other defect types like V_{ga} and As_{Ga} influence not only the carrier trapping lifetime, but also the mobility and the resistivity of the bulk LT-GaAs. The point defects lower the carrier mobility when compared to conventional GaAs due to the decreased scattering lifetime. Furthermore, the hopping conduction between the mid-gap trapping states introduced by point defects decreases the overall resistivity of LT-GaAs [37]. The observed high breakdown voltage arises because of the hopping nature of the conductivity. Despite its short trapping lifetime and high breakdown voltage, the low mobility and resistivity of LT-GaAs does not allow use of the material in photoconductive devices such as detectors and receivers for terahertz photomixers [13]. The resistivity of LT-GaAs may be increased by annealing the material, transforming the excess arsenic into arsenic precipitates. Details of annealing properties and arsenic precipitates will be further discussed in Chapter 6.

(II) GaInNAs Quantum Wells

2.5 Introduction of GaInNAs material system

In order to operate at the important telecommunication wavelengths of 1.3 and 1.55-μm, semiconductor lasers require materials with bandgaps around 0.95 and 0.78 eV, respectively. The potential candidates are as shown in Fig. 2.3. One of the crucial requirements for the long wavelength semiconductor lasers to be commercially viable is that they must be fairly lattice matched with either InP or GaAs. Hence the potential choices are presented at the intersection of the dashed horizontal lines (representing the wavelengths) and the dotted vertical lines below GaAs and InP (defining the lattice parameters). Before the 1990s,

GaInAsP on InP was the only material system used for long wavelength applications, since there was no known material system lattice matched to GaAs that would emit >1.1-μm.

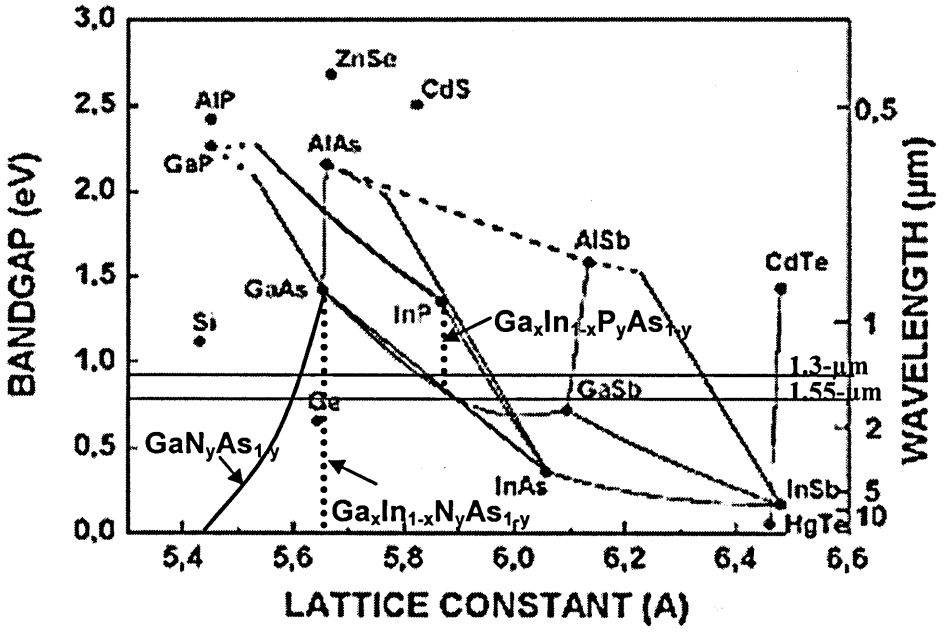

Fig. 2.3 Bandgap energy versus lattice constant of III-V alloys with lines of lattice match for GaInNAs to GaAs and for GaInAsP to InP in the region applicable to long wavelength region. (Modified from Ref [42])

However, Kondow *et al.* has shown that the GaInNAs material system, which can be grown pseudomorphically on GaAs substrate, is capable of having a bandgap energy suitable for long wavelength telecommunication laser operating at 1.3 and 1.55-μm. [38, 39] The GaInNAs/GaAs materials system provides an attractive alternative to the classical GaInAsP/InP because of several main issues [40]:

a) It is very difficult to meet the requirement for the growth of distributed Bragg reflectors (DBR) for InP-based vertical cavity surface-emitting lasers (VCSELs) due to insufficient refractive index contrast in the InP/GaInAsP material system. Furthermore, both the thermal and electrical conductivities of the

InP/GaInAsP materials system are too low to fulfil the requirements of high reflectivity, coupled with low thermal and electrical resistance.

b) The GaInNAs/GaAs materials system provides a better electron confinement (larger conduction band offset, ΔE_c) and larger electron effective mass compared to the GaInAsP/InP material system. The small conduction band offset of the GaInAsP/InP material causes a low temperature threshold T_o in VCSELs. Thus, GaInNAs/GaAs VCSEL provides a higher T_o, higher temperature stability, and a better match of the conduction band and valence band density of states. The electron effective mass increase with N content also indicates a flattening of the conduction band at the Γ point. [41]

c) Compositional control and uniformity of growth of GaInNAs grown by MBE is relatively easier compared to that of As/P control in InGaAsP using MOCVD. As a result, this will translate into better yield and lower cost of production.

d) The GaInNAs/GaAs material system based devices can easily be assimilated into the existing GaAs high-speed electronics. This will provide low cost, high speed integrated devices for communication or optoelectronic networks.

e) A type-I band line-up can also be achieved for the GaInNAs/GaAs materials system.

2.6 Growth and structural properties of GaInNAs

2.6.1 Material properties of GaInNAs

Contrary to the general rule for alloy semiconductors where decreasing lattice parameter normally increases the bandgap energy, $GaAs_{1-x}N_x$ alloys ($0<x<0.015$) show a systematic red-shift of the band-edge luminescence with increasing N content, or bandgap bowing as shown in Fig 2.3 [43, 44] This phenomenon can be explained by the large electronegativity of N, as compared to

other constituent atoms [45], where the electronegativity of N is 3.00, while that of P, As and Sb is around the range from 1.31 to 1.64. [46] The large electronegativity of N and its small covalent radius cause a very strong negative bowing parameter, hence the addition of N into GaAs or InGaAs strongly reduces the bandgap energy [39].

For the GaInNAs novel material system, the addition of In increases the lattice constant, while adding N reduces the compressive strain in the overall GaInNAs material. Thus, GaInNAs can be lattice-matched with the underlying GaAs substrate by adjusting the In and N content. Generally, $Ga_{1-x}In_xN_yAs_{1-y}$ alloys with a small concentration of nitrogen ($y \leq 0.02\%$) can be grown lattice matched with the GaAs substrate when $x \approx 3y$ [47]. Furthermore, both the addition of In and N decreases the bandgap energy of GaInNAs material system, thus rapidly reaching the long wavelength emission region.

2.6.2 GaInNAs epitaxial growth techniques

One of the most important difficulties of GaInNAs growth is the metastability of the alloy material. The GaInNAs material system exists in different basic crystal structures and different regions of growth compatibility, hence creating a miscibility gap in the alloys. This is because InGaN is a hexagonal crystal grown at high temperature, whereas InGaAs is zinc-blende crystal grown at relatively low temperature [40, 48-50]. Hence, when the growth temperature is increased, the metastable alloy tends to phase separate into microscopic regions of InGaN and InGaAs [40, 48-50]. Therefore, to overcome the low solubility of N in GaInNAs, the growth of the material system has to be performed at much lower temperature.

Because the growth temperature for GaInNAs is too low to use both ammonia and arsine as the N and As precursor sources, respectively, growth by metal-organic chemical vapour deposition (MOCVD) is extremely challenging. Because of the large growth temperature difference of InGaAs and InGaN, a very

reactive N source is needed. However, difficult N alternative precursor sources and nonlinear incorporation ratios of the precursors greatly complicate the growth mechanism [40].

Metastable GaInNAs growth by MBE also encounters many obstacles. Firstly, the nitrogen plasma source used in MBE causes ion-induced damage to the growth surface, introducing point defects and surface roughening. Dislocations and clustering effects generated in the GaInNAs layers not only degrade the crystal quality, but also reduce the average N content in the GaInNAs layers due to N fluctuation. The effects of ion-induced damage can be minimized by improving the stability of the plasma source [51], installing an ion collector [52] and/or annealing [53-55]. Furthermore, growth temperature control is extremely important for GaInNAs growth. If the growth temperature exceeds a critical value, the MBE growth of GaInNAs which begins with two-dimensional planar growth is interrupted and three-dimensional coherent islands are formed [56, 57]. On the other hand, the V/III ratio, which was previously regarded as less important than the growth temperature, is extremely critical for the growth of high quality GaInNAs epitaxial layers [58]. The beneficial effect of a low V/III ratio is attributed to the reduction of As interstitials [59], Ga vacancies [60] and antisite defects [61].

2.7 Difficulties with GaInNAs

Indeed, encouraging results of GaInNAs-based QW lasers operating in the 1.3-μm region have been successfully demonstrated by several groups [62-65]. At present however, there are still obstacles in obtaining high-quality near-1.55-μm GaInNAs materials and devices. Nitrogen incorporation into InGaAs in excess of 1% results in strong quenching of the PL luminescesce and broadening of the PL linewidth [66, 67]. In order to reach the 1.55-μm wavelength region, relatively high percentages of N (~3%) are incorporated, hence degrading the optical properties rapidly. Furthermore, the relatively high N composition required to reach this wavelength range encourages phase

separation and the formation of dislocations, even in the case of relatively small lattice mismatch with the substrate [56, 68].

Therefore, GaInNAs multiquantum wells (MQW) heterostructures are typically annealed to improve the crystal alloy quality. *In situ* annealing or *ex situ* rapid thermal annealing (RTA) at around 600 °C was reported to significantly improve the PL intensity and linewidth, while slightly blueshifting the PL wavelength [69, 70]. However, high temperature RTA (~900 °C) is also reported to improve the PL properties, but greatly alters the wavelength [71]. The optical property improvement is probably due to the removal of defects and dislocations which act as non-radiative centers [69]. Pan *et al.* proposed that the blueshift of the annealed GaInNAs PL emission peak is attributed to the interdiffusion of In-Ga at the interface of the GaInNAs QWs and the GaAs barrier layers. Nonetheless, using secondary ion mass spectrometry (SIMS) and nuclear reaction analysis measurements, Spruytte *et al.* showed that the nitrogen out-diffusion from the GaInNAs QWs is predominantly responsible for the PL emission shift [72].

(III) Quantum Dots

2.8 Introduction of QDs

Since the 1970s, thanks to the rapid development and advances in thin film epitaxial growth techniques like the MBE and MOCVD, the first low dimensional heterostructure, known as quantum wells, were developed. Although there were many motivations spurring the heterostructure technology, the capability to realize carrier confinement is one of the most important aspects. The bandstructure of a crystalline semiconductor is the representation of the allowed energy levels for electrons and holes as a function of their momentum or wave vector (k). Significant modifications of the bandstructure have been achieved by restricting the motion of carriers to two-dimensions via

QWs. Generally, QWs are formed by sandwiching a layer of material of low bandgap in between a matrix with a material of higher bandgap.

The electron energy in a solid (infinite body) is a multi-valued function of momentum resulting in energy bands, which constitute continuous densities of states. However, if the carriers in a solid are limited to a layer of thickness on the order of de Broglie wavelength, one can observe the effects of size quantization, where a quantisation of the allowed energy levels emerges from the energy spectrum. The energy of the n-th quantum level of a QW of width L restricted by two infinite barriers is given as follows by the solution of the Schrödinger's equation for a QW [73]:

$$E_n = \frac{\hbar^2}{2m}\left(\frac{\pi}{L}\right)^2 n^2 \tag{2.1}$$

However, continued efforts are being dedicated to further reduce the dimensionality of nanostructures so that the carriers are confined such that their motions are restricted to one, and ultimately zero dimension. This is because the reduced dimensionalities have been predicted to improve the performance of lasers giving for example, very low threshold current, greater temperature stability and narrower spectral linewidth [74-76].

The density of states (DOS), which is the number of available electronic states *per unit volume per unit energy* around an energy E [77], changes with the dimensionality of the nanostructures as shown in Fig 2.4. In the case of laser applications, ideal QDs can provide a much more favourable DOS because QDs only allow energy states which correspond to discrete quantum energy levels of the QDs as a result of carrier localisation in all three dimensions and breakdown of the basic bandstructure model. Furthermore, size-quantized heterostructures increase the DOS for the charge carriers at the band edges. Ideally, a QD has an infinite DOS at the band edges. We can also decrease the temperature sensitivity of the laser threshold current by reducing the dimensionality of the

nanostructures, because when the temperature increases, the high energy tail of the Fermi distribution of the injected carriers enters an energy range that contains a much reduced number of energy states [78]. Besides that, the laser differential-gain (gain increase resulting from the injection of extra electron-hole pairs) increases with lower nanostructure dimensionality because the effective spread of the available electronic states is reduced (narrower linewidth) [79].

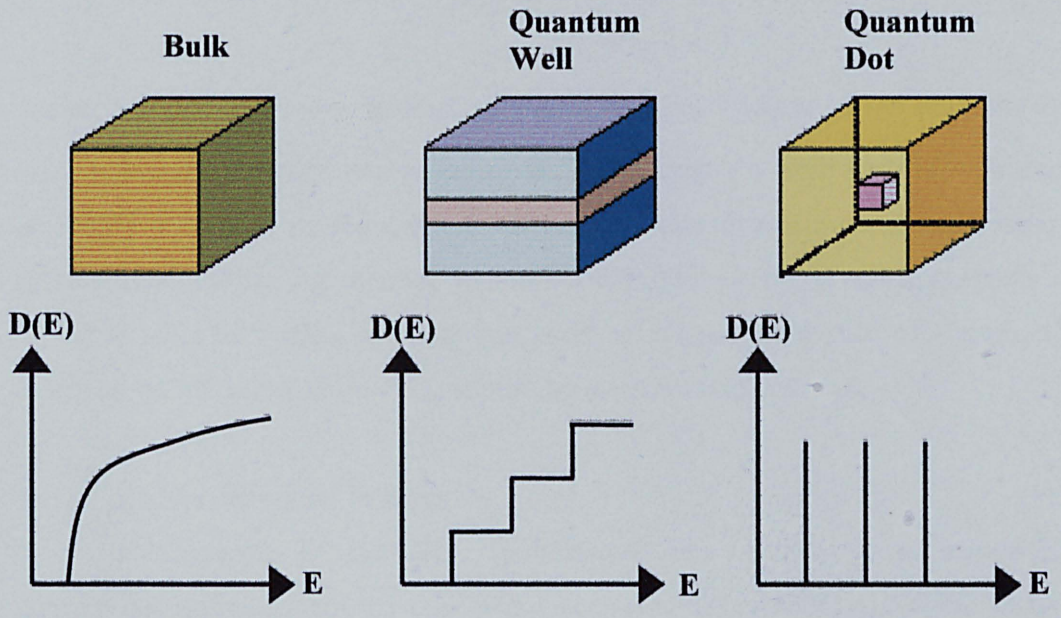

Fig 2.4 The density of electronic states in bulk material (a), quantum wells (b) and quantum dots (c) with the formulas of density of states shown, respectively.

Quantum dots, also known as nanocrystals or "quantum boxes", are nanoscale particles made up usually of thousands of atoms, while behaving like a single gigantic atom. QDs are also regarded as "artificial atoms" because of their

delta-function-like energy states. However, the quantum dots have to fulfil the following requirements in order to make useful devices at room temperature [80]:

A. Size

In very small QDs, the separation between the electronic states and the barrier potential is too small, resulting in thermal evaporation of carriers from the QDs at finite temperature. Hence, the lower size limit of a QD should exceed the value:

$$D_{\min} = \frac{\pi\hbar}{\sqrt{\left(2m_e^*\Delta E_c\right)}} \tag{2.2}$$

where ΔE_c is the energy discontinuity between band edges of the narrow- and wide-bandgap semiconductors. However, there is also a limit for the maximum size of a QD as a prerequisite to utilise the zero-dimensionality confinement effects. Besides that, the thermal population of higher energy levels in larger QDs, is undesirable in certain applications such as lasers. As a rule of thumb, the diameter of In(Ga)As/GaAs QDs should be approximately 20 nm.

B. Uniformity and Density

Fluctuations of the QDs geometrical size results in corresponding fluctuations of the quantum levels, where such fluctuations are typically Gaussian. Hence, the delta-function-like energy peaks of an ideal QD array are also transformed into a Gaussian distribution. For certain applications that require a narrow energy spectrum for high integrated gains, such as QD lasers, the inhomogeneous energy broadening would be undesirable. Gérard *et al.* has attributed the size fluctuations of the QDs to the asynchronous nucleation of islands due to variations of wetting layer thickness [81]. Furthermore, if device operation is based on many QDs, e.g. QD lasers, there should be a minimum packing density or volume filling factor in order to overcome losses.

C. Material Quality

It is essential that the density of point defects and dislocations in a QD and its interface to the surrounding matrix should be kept as low as possible. This is

because the defects provide non-radiative recombination centres that reduce optical efficiency.

2.9 Development of quantum dot heterostructure lasers and other applications for quantum dots

Since QD lasers were proposed by Dingle and Henry [82] in 1976, and later evolved by Arakawa and Sakaki [74], there have been considerable efforts in developing the theory and applications for QDs. Despite the much anticipated development of early predictions, the development of QD lasers has been a much more challenging task, as compared to QW heterostructure lasers. However, the real application of QDs to lasers was finally realised when self-organized growth (SOG) was developed, where dense arrays of uniform and coherent QDs are grown. Details of the SOG of QDs are further elaborated in Section 2.10.2. The breakthrough means that cost effective manufacturing of QD devices came into effect, where hundreds of billions of QDs can be formed, without making any significant changes to the present growth equipment and post-growth processing technology [83]. In 1994, Mukai *et al.* demonstrated the photoluminescence of QD heterostructures in the 1.3-μm wavelength range [84]. This is followed by the first demonstration of room temperature ground-state lasing at 1.3-μm wavelength from a GaAs-based QD heterostructure laser [85]. Today, QD lasers are able to achieve extremely low threshold current densities in the sub-50 A/cm^2 regime, which is much better than what QW lasers is capable of [86, 87].

Recently, QDs have been introduced as one of the most promising candidates for solid state quantum computation and cryptography. It is commonly known that ordinary (classical) computers process and store information as binary digits called bits. If one uses the excitation state of an electron-hole pair localized in a QD island to represent the binary states, the existence (non-existence) of an exciton corresponds to a logical one (zero). By using adjacent QDs, these could

be coupled using the dipole-dipole interaction [88]. Quantum cryptography utilizes QDs as photon emitters, where the frequency of the emitted photons depends on the number of electron-hole pairs present in each dot [89]. Therefore, after the application of spectral filtering, a single-photon pulse can be obtained and any acts of measurement (eavesdropping) will perturb the system [90]. Furthermore, in modern biology and medical analysis, luminescent QDs are researched as biomarkers for selective imaging of tumour cells in living animals, using fluorescence spectroscopy [91].

2.10 Fabrication techniques for quantum dots

Recent developments in advanced crystal growth techniques, especially in MBE [92, 93] and MOCVD [94, 95] has made it possible to precisely carry out atomic layer epitaxy. There are mainly two types of techniques used to fabricate QDs; one by lithographic patterning and etching technique and the other by self-assembly formation.

2.10.1 Lithographic patterning and etching techniques

Originally, the fabrication of QDs was based on lateral patterning of two-dimensional heterostructures. Generally, the nanoscale features were patterned lithographically onto an existing semiconductor wafer with a QW structure. Following the lithographic process, the patterned top barrier material of a quantum well is then defined by selective wet-chemical etching [96] or by the reactive ion beam technique [97].

The lithographic patterning of QDs has several advantages [98], where an almost uniform and arbitrary structure of QDs can be realised depending on the resolution of the lithographic and etching process techniques. The resolution of lithographic techniques, such as electron and focused ion beam lithography, x-ray lithography and optical lithography, is also continuously improving. Besides that,

the lithographic patterning and etching technique is easily compatible with modern VLSI (very large scale integration) semiconductor technology. Nonetheless, the destructive etching process always introduces surface defects and introduces irregularities in the shape of the nanostructures. As a result, non-radiative recombination centres are introduced and thus reduce optical efficiency.

2.10.2 Self-organized growth of QDs

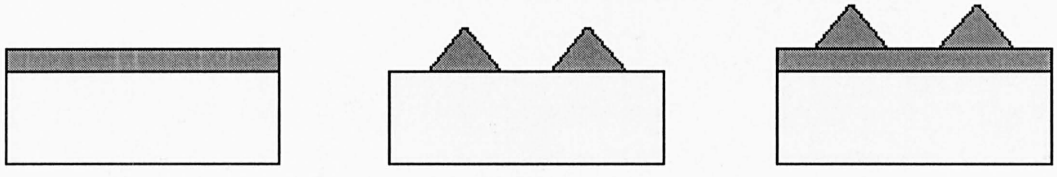

Fig. 2.5 Schematic diagrams of the three epitaxial growth modes: (a) Frank-van der Merwe (FM), (b) Volmer-Weber (VW) and (c) Stranski-Krastanow (S-K).

In principle, there are three well-known growth modes, as shown in Fig. 2.5, by which thin epitaxial films can grow on crystalline substrates [99]: Frank-van der Merwe (FM) [100], Volmer-Weber (VW) [101], and Stranski-Krastanow (S-K) [102]. The growth mode depends primarily on the magnitude of strain introduced during epitaxial growth and the interface energy [103]. If the sum of surface energy α_1 and interface energy α_{12} is less than the energy of the substrate surface, α_2, the FM mode is applicable. Hence, in systems where the lattice-mismatch is very small (~1%), the FM growth mode, or the two dimensional layer-by-layer growth mode, is normally dominant, where the deposited materials are bounded strongly to the substrate. In the opposite case, systems where the lattice-mismatch in large, i.e. $\alpha_1 + \alpha_{12} > \alpha_2$, the surface energy will drive the growth mechanism into the VW mode, also known as island growth mode. However, there is also an intermediate growth mode where two-dimensional layers were followed by island growth, the S-K growth mode, first described by Stranski and Krastanow [102].

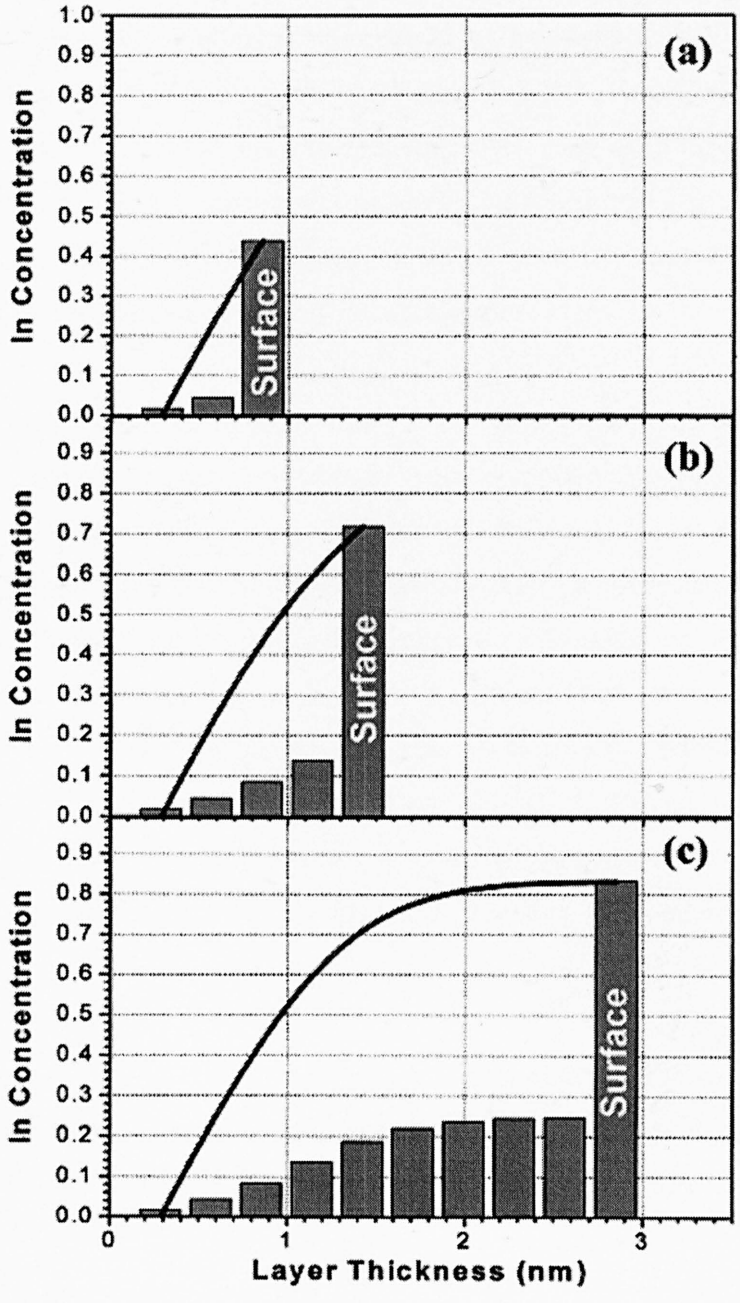

Fig 2.6 Composition variations of In element, based on the Fukatsu/Dehaese segregation model, in the near surface of $In_xGa_{1-x}As$ monolayers (shown with bars) with deposition layer thickness of (a) 3 MLs, (b) 5MLs and (c) 10 MLs. The deposition flux is 25% In and the surface In concentration variation is tracked by the solid line [104].

Strain relaxation and island formation in the S-K growth mode for lattice-mismatched semiconductor epitaxial layer has been studied extensively, especially for the In(Ga)As/GaAs [105-107], InP/(In)GaP [108, 109], GaSb/GaAs [110] and Si/SiGe [111-113] material system. In the case of the In(Ga)As/GaAs material system, the lattice mismatch reaches 7.2%. During S-K growth, the first few monolayers of deposited strained epitaxial material, also known as the wetting layer, form a two-dimensional pseudomorphic layer.

There has been much research on the formulation of theoretical models based on energy calculations and rate equations in order to explain the two-dimensional to three-dimensional transition during S-K growth [114, 115]. It was generally considered that, when the two-dimensional islands exceed a critical size, they should transform into three-dimensional islands. The elastic relaxation on the facet edges, renormalization of the surface energy of the facets, and interaction between neighbouring islands via the substrate were claimed to be the driving forces for the transition [116]. Nevertheless, recent studies by Walther *et al.* [117, 118] and Cullis *et al.* [104] have shed more light on the mechanism relating to the growth of the initial wetting layer and the critical thickness which it must attain for the S-K transition.

Using the $In_xGa_{1-x}As/GaAs$ system as a reference, Cullis *et al.* [104, 119] proposed that strain introduced by the vertical segregation of In element from the deposited material on the surface of the initial flat wetting-layer controls the critical point at which the transition to island occurs (hereafter referred to as the WCNH mechanism). Based on the Fukatsu/Dehaese segregation model [120, 121], the WCNH mechanism model considers the exchange of the group III species between the top two layers during growth. Hence, the surface layer demonstrates a very significant deviation from the deposition flux concentration, as shown in Fig 2.6. For example, if a relatively dilute ($x = 0.25$) alloy is deposited, the surface monolayer will attain a saturation concentration of 80-85 % for an initial wetting layer thickness of 2.5 nm. It has been shown that a deposition flux of 25 % In (or a misfit of $\geq$ 1.8 %) is approximately the minimum that will

induce the S-K transition [106]. Therefore, the critical surface In concentration for S-K transition is also equivalent to the mentioned figure of 80-85 % In. It is then predicted that the S-K transition occurs for any deposition flux provided that the surface In concentration reaches this critical level. Using the segregation model, the critical wetting layer thickness for the transition can be measured, depending on the indium mole fraction of the deposited material, as shown in Fig. 2.7.

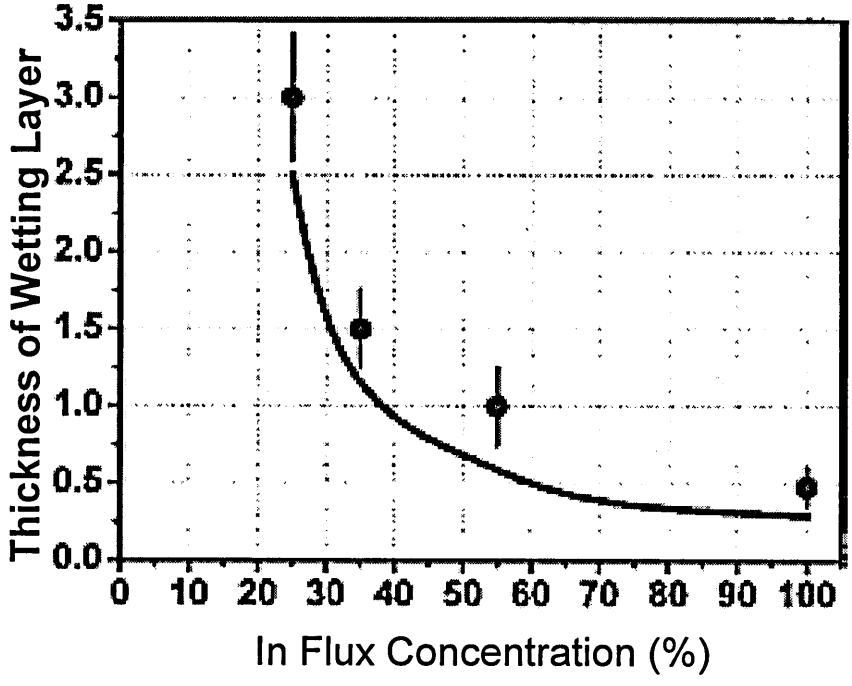

Fig. 2.7 Variations of the critical thickness for the S-K transition as a function of the In concentration: the measured values are given as data points whereas theoretically predicted values based upon the WCNH mechanism are presented as continuous curve [113].

The WCNH mechanism states that the critical surface concentration of In (and associated strain) must build up before the S-K transition occurs. However, the large and increasing strain on the surface layer makes it very difficult for the deposited atoms to be incorporated into this layer, hence increasing the density of adatoms. The thermodynamic representation of this transition is illustrated in

Fig. 2.8 where the free energy of the surface adatoms and atomic clusters gradually rises (point A→B) due to the increasing adatom concentration and number density of unstable growth nuclei [119]. As ever larger nuclei are formed, at certain point the critical nuclei appear (point C) where the expansion of which leads to the formation of stable islands. The islands are excellent sinks for adatoms. As a result, further growth of islands leads to a rapid decrease in adatom concentration and surface free energy. Indeed, the WCNH mechanism is responsible for the formation of QDs in the present work.

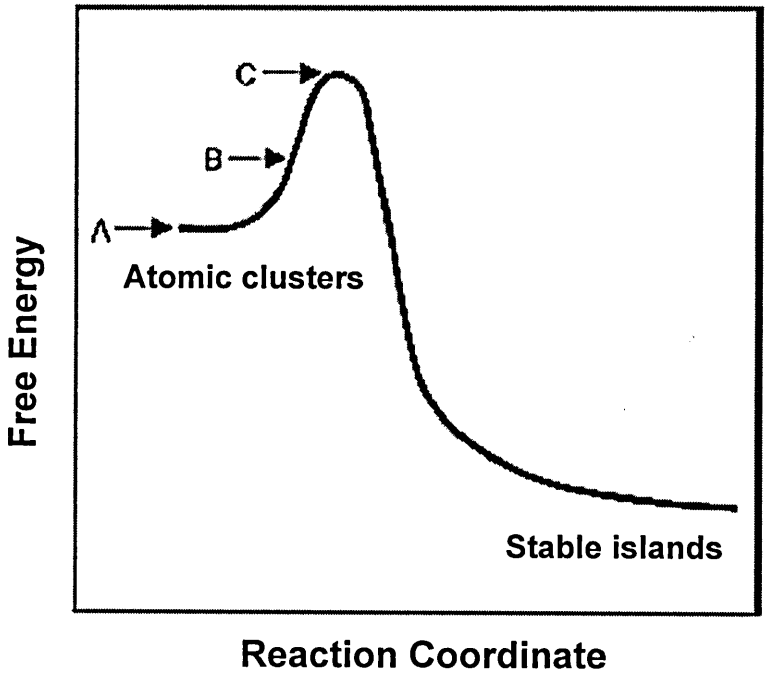

Fig. 2.8 Schematic illustration of free energy variation for surface atomic clusters and stable islands during progression of S–K islanding transition [118].

2.11 References

[1] H. Sakaki, in R. J. Malik (ed.), *III-V Semiconductor Materials and Devices*, North-Holland, Amsterdam, (1989), p. 217.

[2] R. A. Stall, C. E. C. Wood, P. D. Kirchner, and L. F. Eastman, Electron. Lett., **16** (1980) 171.

[3] G. M. Metze, and A. R. Calawa, Appl. Phys. Lett., **42** (1983) 818.

[4] C. E. C. Wood, J. Woodcock, and J. J. Harris, Inst. Phys. Conf. Ser., **45** (1979) 29.

[5] T. Murotani, T. Shimanoe, and S. Mitsui, J. Cryst. Growth, **45** (1978) 302.

[6] R. Stall, C. Wood, P. Kirchner, and L. Eastman, Electron. Lett., **16** (1980) 171.

[7] F. Smith, A. Calawa, C. L. Chen, M. Manfra, and L. Mahoney, Electron. Device Lett., **9** (1988) 77.

[8] F. W. Smith, H. Q. Le, V. Diadiuk, M. A. Hollis, A. R. Calawa, S. Gupta, M. Frankel, D. R. Dykaar, G. A. Mouron, and T. Y. Hsiang, Appl. Phys. Lett., **54** (1989) 890.

[9] L. W. Yin, Y. Hwang, J. H. Lee, R. M. Kolbas, R. J. Trew, and U. K. Mishra, IEEE Electron. Device Lett., **11** (1990) 561.

[10] J. K. Luo, H. Thomas, D. V. Morgan, D. Westwood and R. H. Williams, Semicond. Sci. Technol., **9** (1994) 2199.

[11] M. Y. Frankel, J. F. Whitaker, G. A. Mourou, F. W. Smith, and A. R. Calawa, IEEE Trans. Electron. Devices, **37** (1990) 2493.

[12] Y. Chen, S. Williamson, T. Brock, F. W. Smith, and A. R. Calawa, Appl. Phys. Lett., **59** (1991) 1984.

[13] I. S. Gregory, W. R. Tribe, B. E. Cole, C. Baker, M. J. Evans, I. V. Bradley, E. H. Linfield, A. G. Davies, and M. Missous, Electron. Lett., **40** (2004) 143.

[14] C. Y. Chang and F. Kai, *GaAs High-Speed Devices*, Wiley and sons, New York, (1994).

[15] L. Pavesi, *Properties of Gallium Arsenide*, INSPEC, EMIS Datareviews series 2, (1990).

[16] M. Kaminska, Z. Liliental-Weber, E. R. Weber, T. George, J. B. Kortright, F. W. Smith, B-Y. Tsaur, and A. R. Calawa, Appl. Phys. Lett., **54** (1989) 1881.

[17] M. Kaminska, E. R. Weber, Z. Liliental-Weber, and R. Leon, J. Vac. Sci. Technol., **B7** (1989) 710.

[18] X. Liu, A. Prasad, J. Nishio, E. R. Weber, Z. Liliental-Weber, and W. Walukiewicz, Appl. Phys. Lett., **67** (1995) 279.

[19] Z. Liliental-Weber, W. Swider, K. M. Yu, J. B. Kortright, F. W. Smith, and A. R. Calawa, Appl. Phys. Lett., **58** (1991) 2153.

[20] B. R. Pamplin (ed.), *Molecular Beam Epitaxy*, Pergamon Press, Oxford, (1980).

[21] B. A. Joyce, Rep. Prog. Phys., **48** (1985) 1637.

[22] C. T. Foxon, B. A. Joyce, R. F. C. Farrow, and R. M. Griffiths, J. Phys. D: Appl. Phys., **7** (1974) 2422.

[23] J. H. Neave, P. Blood, and B. A. Joyce, Appl. Phys. Lett., **36** (1980) 311.

[24] J. R. Arthur, J. Appl. Phys., **28** (1968) 4032.

[25] C. T. Foxon, and B. A. Joyce, Surf. Sci., **64** (1977) 293.

[26] C. T. Foxon, and B. A. Joyce, Surf. Sci., **50** (1975) 434.

[27] S. Gupta, J. F. Whitaker, and G. A. Mourou, J. Quantum Electron., **28** (1992) 2464.

[28] N. D. Jäger, A. K. Verma, P. Dreszer, N. Newman, Z. Liliental-Weber, M. Van Schilfgaarde, and E. R. Weber, J. Electron. Mat., **22** (1993) 1499.

[29] Y. H. Chen, Z. G. Wang, and Z. Yang, J. Appli. Phys., **87** (2000) 2923.

[30] J. L. Lee, A. Uedono, and S. Tanigawa, J. Appl. Phys., **67** (1990) 6153.

[31] D. E. Bliss, W. Walukiewicz, J. W. Ager III, E. E. Haller, and K. T. Chan, J. Appl. Phys., **71** (1992) 1699.

[32] M. Stellmacher, J. Nagle, J. F. Lampin, P. Santoro, J. Vaneecloo, and A. Alexandrou, J. Appl. Phys., **88** (2000) 6026.

[33] D. E. Bliss, W. Walukiewicz, and E. E. Haller, J. Electron. Mater., **22** (1993) 1401.

[34] N. F. Chen, Y. T. Wang, H. J. He, L. Y. Lin, Jpn. J. Appl. Phys., **35** (1996) L1238.

[35] K. M. Yu, M. Kaminska, and Z. Liliental-Weber, J. Appl. Phys., **72** (1992) 2850.

[36] S. B. Zhang, and J. E. Northrup, Phys. Rev. Lett., **67** (1991) 2339.

[37] H. Yamamoto, Z. Q. Fang, and D. C. Look, Appl. Phys. Lett., **57** (1990) 1537.

[38] M. Kondow, K. Uomi, A, Niwa, T. Kitatani, S. Watahiki, and Y. Yazawa, *Proc. 1995 Solid State Device and Mat.*, Osaka, Japan (1995) 1016.

[39] M. Kondow, K. Uomi, A, Niwa, T. Kitatani, S. Watahiki, and Y. Yazawa, Jpn. J. Appl. Phys., **35** (1996) 1273.

[40] J. S. Harris Jr., Semicond. Sc. Technol., **17** (2002) 880.

[41] C. Skierbiszewski , P. Perlin, P. Wisniewski, W. Knap, T. Suski, W. Walukiewicz, W. Shan, K. M. Yu, J. W. Ager, E. E. Haller, J. F. Geisz, J. M. Olson, Appl. Phys. Lett., **76** (2000) 2409.

[42] http://www.iaf.fraunhofer.de/eng/kk/design-sensor-antim.htm

[43] M. Weyers, M. Sato and H. Ando, Jpn. J. Appl. Phys., **31** (1992) L853.

[44] M. Kondow, K. Uomi, K. Hosomi, and T. Mozume, Jpn. J. Appl. Phys., **33** (1994) L1056.

[45] S. Sakai, Y. Ueta, and Y. Terauchi, Jpn. J. Appl. Phys., **32** (1993) 4413.

[46] J. C. Phillips, *Bonds and Bands in Semiconductors*, Academic, New York, (1973) p.54.

[47] M. Kondow, T. Kitatani, S. Nakatsuka, M. C. Larson, K. Nakahara, Y. Yazawa, M. Okai, K. Uomi, IEEE J. Sel. Top. Quantum Elec., **3** (1997) 719.

[48] S. G. Spruytte, M. C. Larson, W. Wampler, C. Coldren, P. Krispin, H. E. Peterson, S. Picraux, K. Ploog, and J. S. Harris, J. Cryst. Growth, **227-228** (2001) 506.

[49] J. C. Harmand, G. Ungaro, L. Largeau, and G. LeRoux, Appl. Phys. Lett., **77** (2000) 2482.

[50] C. Jin, Y. Qiu, S. A. Nikishin, and H. Temkin, Appl. Phys. Lett., **74** (1999) 3516.

[51] R. J. Molnar, R. Singh, and T. D. Moustakas, J. Electron. Mater., **24** (1995) 275.

[52] A. Utsumi , Y. Furukawa , H. Yonezu , Y. Yoshizumi , Y. Morita , and A. Wakahara, Phys. Status Solidi A, **202** (2005) 758.

[53] Z. Pan , L. H. Li , W. Zhang , X. U. Wang , Y. W. Lin, and R. H. Wu, J. Cryst. Growth, **227** (2001) 516.

[54] T. S. Kim, J. Y. Park, T. V. Cuong, H. G. Kim, H. J. Lee, E. K. Suh, and C. H. Hong, J. Cryst. Growth, **267** (2004) 412.

[55] M. Albrecht, V. Grillo, T. Remmele, H. P. Strunk, A. Y. Egorov, G. Dumitras, H. Riechert, A. Kaschner, R. Heitz, and A. Hoffmann, Appl. Phys. Lett., **81** (2002) 2719.

[56] M. Herrera, D. Gonzalez, R. Garcia, M. Hopkinson, P. Navaretti, M. Gutierrez, and H. Y. Liu, IEE Proc.-Optoelectron., **151** (2004) 385.

[57] X. Yang, M. J. Jurkovic, J. B. Herouz, and W. I. Wang, Appl. Phys. Lett., **75** (1999) 178.

[58] G. Jaschke, R. Averbeck, L. Geelhaar, and H. Riechert, J. Cryst. Growth, **278** (2005) 224.

[59] R. Yano, Y. Hirayama, S. Miyashita, H. Sasabu, N. Uesugi, S. Uehara, Phys. Lett. A, **289** (2001) 93.

[60] X. Liu, A. Prasad, J. Nishio, E.R. Weber, Z. Liliental-Weber, W. Walukiewicz, Appl. Phys. Lett., **67** (1995) 279.

[61] R. Yano, Y. Hirayama, S. Miyashita, H. Sasabu, N. Uesugi, S. Uehara, J. Appl. Phys., **94** (2003) 3966.

[62] C. W. Coldren, M. C. Larson, S. G. Spruytte, and J. S. Harris, Electron. Lett., **36** (2000) 951.

[63] B. Borchert, A. Y. Egorov, S. Illek, M. Komainda, and H. Riechert, Electron. Lett., **35** (1999) 2204.

[64] M. C. Larson, M. Kondow, T. Kitatani, K. Nakahara, K. Tamura, H. Inoue, and H. Oumi, IEEE Photon. Technol. Lett., **10** (1998) 188.

[65] W. Li, T. Jouhti, Ch. S. Peng, J. Konttinen, P. Laukkanen, E. Pavelescu, M. Dumitrescu, and M. Pessa, Appl. Phys. Lett., **79** (2001) 3386.

[66] H. P. Xin and C. W. Tu, Appl. Phys. Lett., **72** (1998) 2442.

[67] S. G. Spruytte, C. Coldren, J. S. Harris, W. Wampler, P. Krispin, K. Ploog, and M. C. Larson, J. Appl. Phys., **89** (2001) 4401.

[68] I. A. Buyanova, W. M. Chen, G. Pozina, J. P. Bergman, B. Monemar, H. P. Xin, and C. W. Tu, Appl. Phys. Lett., **75** (1999) 501.

[69] Z. Pan, L. H. Li, W. Zhang, Y. W. Lin, and R. H. Wu, Appl. Phys. Lett., **77** (2000) 1280.

[70] T. Kitatani, K. Nakahara, M. Kondow, K. Uomi, and T. Tanaka, J. Cryst. Growth, **209** (2000) 345.

[71] H. P. Xin, K. L. Kavanagh, M. Kondow, and C. W. Tu, J. Cryst. Growth, **202** (1999) 419.

[72] S. G. Spruytte, C. Coldren, J. S. Harris, W. Wampler, P. Krispin, K. Ploog, and M. C. Larson, J. Appl. Phys., **89** (2001) 4401.

[73] A. I. M. Rae, *Quantum Mechanics*, IOP Publishing, 3rd edition, (1992)

[74] Y. Arakawa and H. Sakaki, Appl. Phys. Lett., **40** (1981) 939.

[75] K. Shum, J. Appl. Phys., **69** (1991) 6484.

[76] Y. Arakawa, K. Vahala, A. Yariv, and K. Lau, Appl. Phys. Lett., **48** (1986) 384.

[77] J. Singh, *Physics of Semiconductors and their Heterostructures*, McGraw Hill, (1993) p. 16-17.

[78] T. T. J. M. Berendschot, H. A. J. M. Reinen, H. J. A. Bluyssen, C. Harder and H. P. Meier, Appl. Phys. Lett. **54** (1989) 1287.

[79] Y. Arakawa, K. Vahala, A. Yariv, and K. Lau, Appl. Phys. Lett., **47** (1985) 1142.

[80] D. Bimberg, M. Grundmann, and N. N. Ledentsov, *Quantum Dot Heterostructures*,John Wiley and sons, Chichester, (1999), pp. 6-8.

[81] J. M. Gérard, J. B. Génin, J. Lefebvre, J. M. Moison, N. Lebouché and F. Barthe, J. Cryst. Growth, **150** (1995) 351.

[82] R. Dingle and C. H. Henry, (1976) US Patent 3982207.

[83] N. N. Ledentsov, M. Grundmann, F. Heinrichsdorff, D. Bimberg, V. M. Ustinov, A. E. Zhukov, M. V. Maximov, Z. I. Alferov, and J. A. Lott, IEEE J. Sel. Top Quant. El., **6** (2000) 439.

[84] K. Mukai, N. Ohtsuka, M. Sugawara, S. Yamazaki, Jpn. J. Appl. Phys., **33** (1994) L1710.

[85] D. L. Huffaker, G. Park, Z. Zou, O. B. Shchekin, and D. G. Deppe, Appl. Phys. Lett., **73** (1998) 2564.

[86] G. Park, O. B Shchekin, D. L. Huffaker, and D. G. Deppe, IEEE Photonic Tech Lett., **12** (2000) 230.

[87] H. Y. Liu, I. R. Sellers, T. J. Badcock, D. J. Mowbray, M. S. Skolnick, K. M. Groom, M. Gutierrez, M. Hopkinson, J. S. Ng, J. P. R. David, and R. Beanland, Appl. Phys. Lett., **85** (2004) 704.

[88] H. Kamada and H. Gotoh, Semicond. Sci. Technol., **19** (2004) S392.

[89] N. Gisin, G. Ribordy, W. Tittel and H. Zbinden, Rev. Mod. Phys., **74** (2002) 145.

[90] J. M. Gerard, and B. Gayral, J. Lightwave Tech., **17** (1999) 2089.

[91] X. Gao, Y. Cui, R. M. Levenson, L. W. K. Chung, and S. Nie., Nat. Biotechnol., **22** (2004) 969.

[92] Y. W. Mo, D. E. Savage, B. S. Swartzentruber, and M. G. Lagally, Phys. Rev. Lett., **65** (1990) 1020.

[93] J. M. Moison, F. Houzay, F. Barthe, L. Leprince, E. Andre, and O. Vatel, Appl. Phys. Lett., **64** (1994) 196.

[94] N. Carlsson, W. Seifert, A. Petersson, P. Castrillo, M. E. Pistol, and L. Samuelson, Appl. Phys. Lett., **65** (1994) 3093.

[95] R. Notzel, R. J. Temmyo, H. Kamada, T. Furuta, and T. Tamamura, Appl. Phys. Lett., **65** (1994) 457.

[96] A. Schmidt, A. Forchel, J. Straka, I. Gyuro, P. Speier, and E. Zielinski, J. Vac. Sci. Technol. B **10** (1992) 2896.

[97] J. S. Weiner, J. M. Calleja, A. Pinczuk, A. Schmeller, B. S. Dennis, A. R. Goñi, L. N. Pfeiffer, and K. W. West, Appl. Phys. Lett., **63** (1994) 237.

[98] D. Bimberg, M. Grundmann, and N. N. Ledentsov, *Quantum Dot Heterostructures*,John Wiley and sons, Chichester, (1999), p. 9.

[99] E. Bauer, Z. Kristallogr., **110** (1958) 372.

[100] F. C. Frank and J. H. Van der Merwe, Proc. R. Soc. Lon. Ser. A, **198** (1949) 205.

[101] M. Volmer and A. Weber, Z. Phys. Chem. (Munich), **119** (1926) 205.

[102] I. N. Stranski and L. Krastanow, Sitzungsber. d. Akad. d. Wissenschaften in Wien, Abt. IIb, Band, **146** (1937) 797.

[103] D. Bimberg, M. Grundmann, and N. N. Ledentsov, *Quantum Dot Heterostructures,* John Wiley and sons, Chichester, (1999), p. 38.

[104] A. G. Cullis, D. J. Norris, T. Walther, M. A. Migliorato, and M. Hopkinson, Phys. Rev. B, **66** (2002) 081305(R).

[105] S. Guha, A. Madhukar, and K. C. Rajkumar, Appl. Phys. Lett., **57** (1990) 2110.

[106] A. G. Cullis, A. J. Pidduck, and M. T. Emeny, J. Cryst. Growth, **158** (1996) 15.

[107] J. M. Moison, J. M. Moison, F. Houzay, F. Barthe, L. Leprince, E. André, and O. Vatel, Appl. Phys. Lett., **64** (1994) 196.

[108] N. Carlsson, W. Seifert, A. Petersson, P. Castrillo, M. E. Pistol, and L. Samuelson, Appl. Phys. Lett., **65** (1994) 3093.

[109] P. M. Petroff and S. P. Denbaars, Superlattices Microstruct., **15** (1994) 15.

[110] B. R. Bennett, B. V. Shanabrook, P. M. Thibado, L. J. Whitman and R. Magno, J. Cryst. Growth, **175/176** (1997) 888.

[111] D. J. Eaglesham and M. Cerullo, Phys. Rev. Lett., **64** (1990) 1943.

[112] I. Goldfarb and G. A. D. Briggs, J. Cryst. Growth **198/199** (1999) 1032.

[113] D. E. Jesson, M. Kastner, and B. Voigtlander, Phys. Rev. Lett., **84** (2000) 330.

[114] V. A. Shchukin, N. N. Ledentsov, P. S. Kop'ev, and D. Bimberg, Phys. Rev. Letts., **75** (1995) 2968.

[115] J. Tersoff, Phys. Rev. Letts., **81** (1998) 3183.

[116] P. Bhattacharya, S. Ghosh, and A.D. Stiff-Roberts, Annu. Rev. Mater. Res., **34** (2004) 1–40.

[117] T. Walther, A. G. Cullis, D. J. Norris, and M. Hopkinson, Phys. Rev. Letts., **86** (2001) 2381.

[118] T. Walther, A. G. Cullis, D. J. Norris, and M. Hopkinson, Microscopy of Semiconducting Materials, edited by A. G. Cullis and J. L. Hutchison (IOPP, Bristol, 2001) 85-88.

[119] A. G. Cullis, D. J. Norris, M. A. Migliorato, M. Hopkinson, Appl. Surf. Sci., **244** (2005) 65.

[120] S. Fukatsu, K. Fujita, H. Yaguchi, Y. Shiraki, and R. Ito, Appl. Phys. Lett., **59** (1991) 2103.

[121] O. Dehaese, X. Wallart, and F. Mollot, Appl. Phys. Lett., **66** (1995) 52.

Chapter 3

Transmission Electron Microscopy

3.1 Introduction

Microscopy is a system that generally reveals a very small 'object' as a magnified 'image'. The basic principles of electron microscopy are almost identical to those of light microscopy, except that electron microscopes use electron waves as opposed to light waves as used by light microscope. However, according to the Rayleigh's criterion for resolution,

$$\delta = \frac{0.61\lambda}{\mu \sin \beta} \tag{3.1}$$

where δ is the smallest distance that can be resolved, λ is the wavelength of the radiation, μ is the refractive index of the viewing medium and β is the semi-angle of collection of the magnifying lens, the resolution of light microscopy is only approximately 300 nm. The rapid development in optoelectronic and electronic devices demands more miniaturization and sophistication in semiconductor engineering. As it becomes increasingly important to analyse the growth processes and the microstructures of the semiconductors on the nanoscale, sophisticated equipment and techniques capable of analysing the microstructure on the atomic scale is indispensable.

In the transmission electron microscope (TEM), the de Broglie wavelength is of the order of a few nm and the point resolution of high end modern TEM is approximately 0.1 nm. Although the point resolution is quite far from the theoretical wavelength limit of resolution due to aberrations and imperfections in the microscope lenses (further discussed in Section 3.3), the TEM is still capable of providing atomic resolution. Furthermore, charged particles like electrons provide strong interaction with matter. The electrons in the TEM undergo several

interactions within an interaction volume which produces a wide range of secondary signals from the specimen as shown in Fig. 3.1. The interaction of the electron beam with matter provides much information that can be used for compositional analysis. For example, the inelastic scattering of electrons can be utilized for analytical electron microscopy, such as energy-dispersive EDX, EELS and EFTEM.

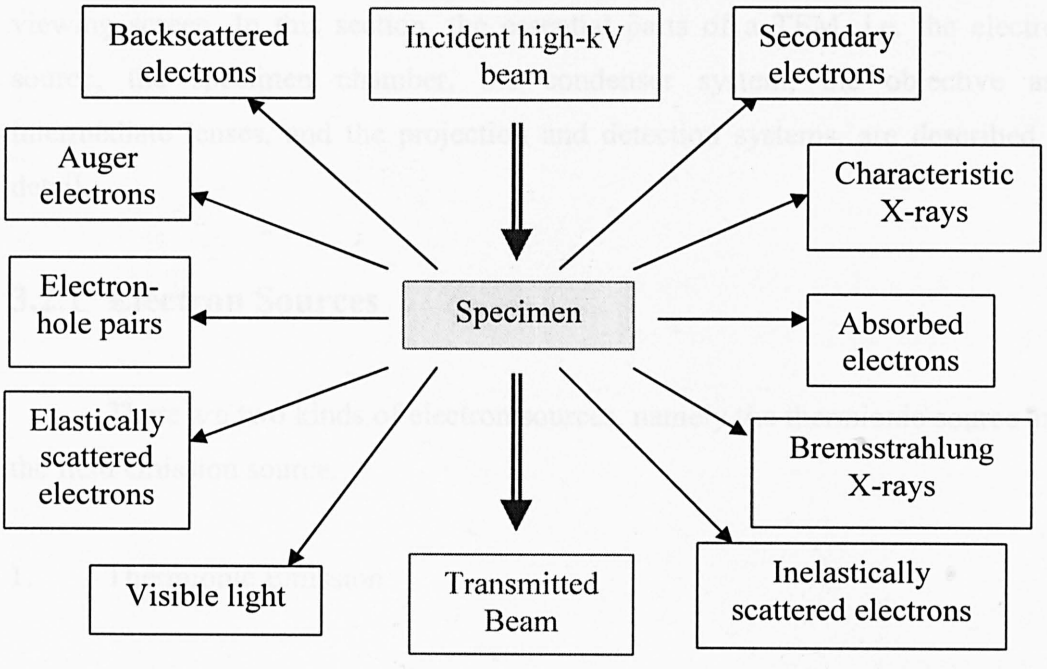

Fig. 3.1 Signals generated when high-energy electron beam interact with a thin specimen.

This chapter is in three parts. The first part provides a brief introduction on the physical structure of TEM and the aberrations and imperfections of TEM lenses. The second part largely describes the TEM sample preparation procedures. Lastly, the third part focuses on a description of TEM imaging and spectroscopy techniques.

PART I

3.2 The structure of TEM

As mentioned earlier, the major components of a TEM are analogous to those of a light microscope. The condenser system acts as a collimator to control the electron beam before it reached the specimen. Subsequently, the objective and projection lenses magnify the image before it is displayed on a fluorescent viewing screen. In this section, the essential parts of a TEM, i.e. the electron source, the specimen chamber, the condenser system, the objective and intermediate lenses, and the projection and detection systems, are described in detail.

3.2.1 Electron Sources

There are two kinds of electron sources, namely the thermionic source and the field emission source.

1. Thermionic Emission

A thermionic source produces electrons when heated to a high temperature, by providing internal electrons with sufficient energy to overcome the natural barrier or "work function" (Φ). Naturally, the only viable materials are either refractory (high melting point) materials or those with low work function [1]. The physics of thermionic emission follows Richardson's Law [2]:

$$J = AT^2 e^{-\frac{\phi}{kT}} \tag{3.2}$$

where J is the current density from the source, k is Boltzmann's constant and A is Richardson's constant. Indeed, heating up the thermionic source to a certain temperature T will overcome Φ, thus facilitating electron escape and provides higher J. However, the source life is shortened through evaporation and/or

oxidation at higher temperatures. As a compromise, the thermionic source is usually operated "under-saturation".

Tungsten and lanthanum hexaboride (LaB_6) are commonly used as thermionic sources. Although tungsten filament has a relatively high work function, tungsten has the highest melting point of metals (3695 K) and hence an ample supply of electrons can be obtained below the melting point. On the other hand, LaB_6 which has a low work function (~3.0 eV) is also commonly used as a thermionic source.

2. Field Emission

The principle behind the field emission gun (FEG) is that the strength of an electric field, E, is largely increased at the sharp end of the electron gun. As a large voltage is applied to a spherical point of radius, r, then:

$$E = \frac{V}{r} \tag{3.3}$$

The extremely high electric field lowers the work function barrier of the metal surface sufficiently for electrons to tunnel out of the material. The brightness from a field emission source, which is a few orders of magnitude higher than thermionic sources, depends strongly on the applied force, F, according to the Fowler-Nordheim equation [3]:

$$I = 6.2\times10^{-6}\frac{(E_f/\Phi)^{1/2}F^2}{(E_f+\Phi)}\exp(\frac{-6.8\times10^9\Phi^{3/2}}{F})Am^{-2} \tag{3.4}$$

where I is the field emission current and E_f is the Fermi energy. However, this process imposes severe stress on the tip (which is <0.1 μm) and the material has to be strong. The material also has to be free from any contaminant and oxide. This requirement is achieved by operating in UHV ($<10^{-11}$ torr). Alternatively, we can keep the tip in pristine condition whilst operating in poorer vacuum by heating it. Usually, the material used is a tungsten tip, grown with <310> orientation.

UNIVERSITY
OF SHEFFIELD
LIBRARY

3. Comparisons of Guns

	Units	Tungsten	LaB_6	Field Emission
Work function	eV	4.5	2.4	4.5
Richardson's constant	A/m^2K^2	6×10^5	4×10^5	-
Operating temperature	K	2700	1700	300
Current density	A/m2	5×10^5	10^6	10^{10}
Crossover size	μm	50	10	<0.01
Brightness	$A/m^2/srad$	10^9	5×10^{10}	$>10^{13}$
Energy spread	eV	1.5	0.9	0.3
Emission current stability	%/hr	<0.1	<0.1	1-5
Vacuum	Pa	10^{-2}	10^{-4}	10^{-8}
Lifetime	hr	100	500	>1000

Table 3.1 Characteristics of three principle sources operating at 100kV.

Tungsten electron sources provide the poorest electron beam characteristics. However, they are the cheapest, robust, reliable and easily replaceable. LaB_6 crystals can be produced with a fine tip, giving a much higher beam current density, improved coherency and energy spread than for tungsten sources. As for FEG, the current density and the brightness generated are a few orders of magnitude higher than for a LaB_6 source. Furthermore, FEG which has an extremely small source size means that the beam has high spatial coherence and the energy spread is extremely small, but also means that it is unable to illuminate large areas of the specimen without losing its intensity. FEG is very expensive due to the need for UHV conditions. Most of the important characteristics of the three guns operating at 100kV are summarised below in Table 3.1. It is noted that under normal circumstances, the highest kV is chosen because the gun is brightest. The resolution is also potentially better because of the shorter wavelength. The heating effect due to the electron beam is also smaller

because the cross section for inelastic scatter is smaller. Nonetheless, for lighter and more beam-sensitive materials, such as ceramics and polymers, lower operating voltages may be better [4].

3.2.2 The condenser system

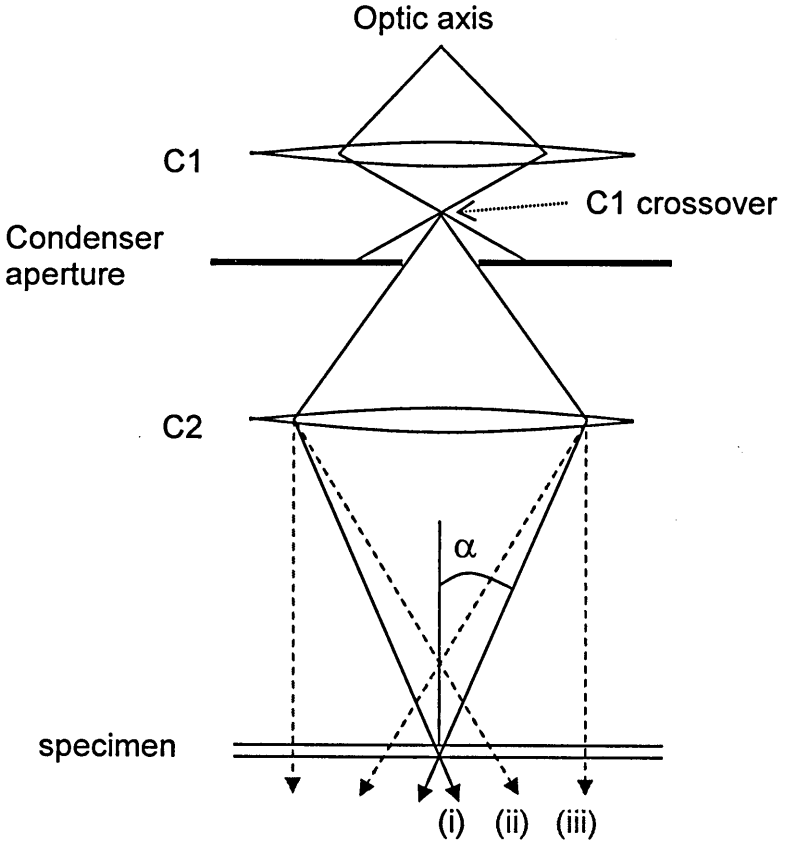

Fig. 3.2 The two-lenses condenser system in TEM. (i), (ii) and (iii) show the focused, overfocused and underfocused beams respectively.

The condenser system delivers the desired intensity of electrons from the electron gun to the specimen under the control of the operator. It consists of two or more condenser lenses, used to demagnify the beam from the source and control its diameter as it hits the specimen [5]. An aperture exists between the

condenser lenses which can be used to control the convergence angle. A smaller condenser aperture results in a smaller angle of beam convergence, α, and therefore increases the coherence of the beam. Furthermore, the size of condenser aperture affects both the intensity of the beam (a smaller aperture provides less intensity) and the image quality (electrons further from the optic axis will be more affected by spherical aberration).

The first condenser lens, C1 or "spot size" controller, determines the demagnification of the gun crossover whereas the second lens, C2, provides control of the convergence angle α of the beam and the area of illumination at the specimen as shown in Fig. 3.2. Underfocusing C2 (ray (iii)) results in a larger area of illumination, as well as a more parallel beam. In order to obtain a focused beam on the specimen, the convergence angle is increased (ray (i)). In general, parallel beams are used for diffraction contrast TEM images and HRTEM images. Instead, convergent beam electron diffraction (CBED) pattern would need a small spot size, a large condenser aperture with the beam focused onto the specimen [5].

3.2.3 The specimen chamber

It is crucial that the specimen holder is placed precisely inside the objective lens within a small gap. The narrow gap allows a short lens focal length which reduces the effect of spherical and chromatic aberrations (further discussed in Section 3.3). However, it should be able to be moved several millimetres and tilted by large angles. An important consideration is that the specimen should not move laterally while tilted. This is especially true when the specimen is in the eucentric plane, which is when the specimen is at the intersection of the axis of tilt and the optical axis. Specimen drifts in the specimen stage can be compensated using a piezo stage and a computer-based image correlation facility.

3.2.4 The objective and intermediate lenses

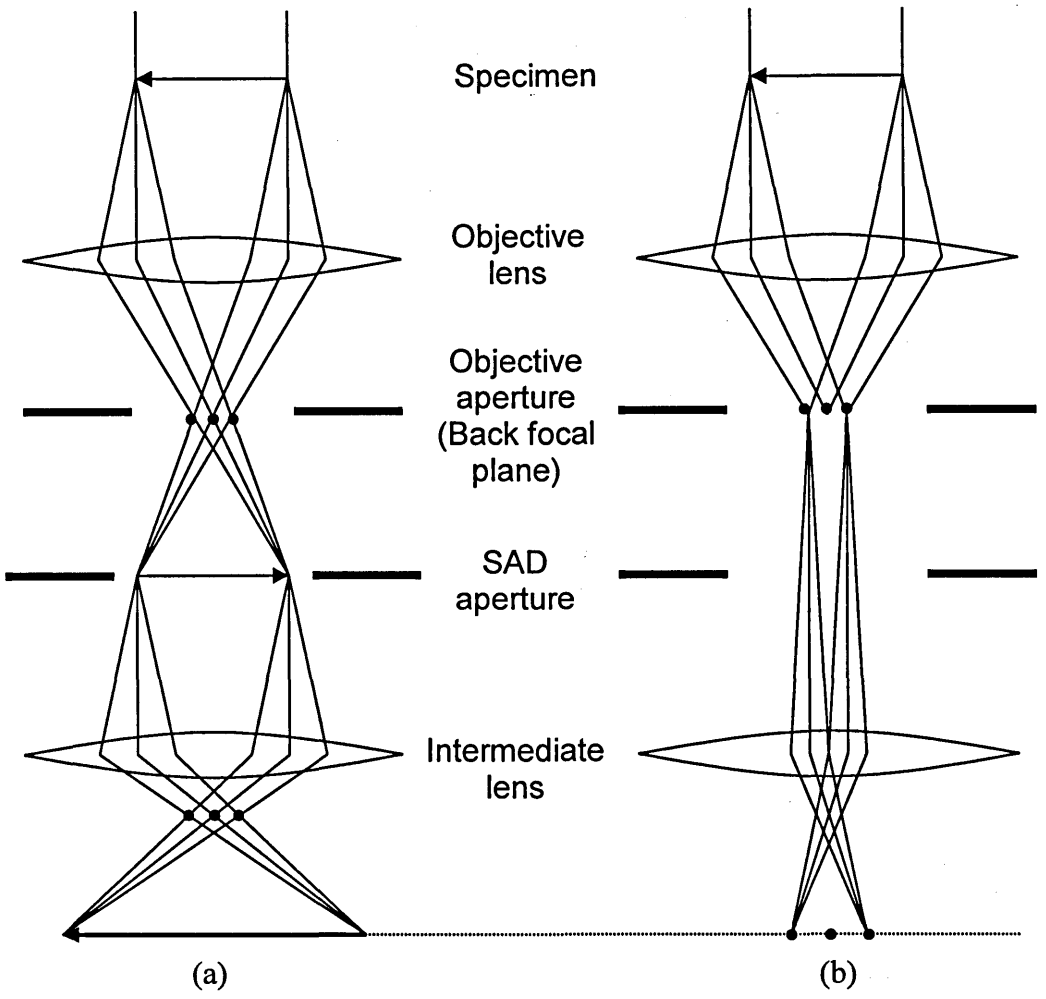

Fig. 3.3 The objective and intermediate lenses. (a) In imaging mode. (b) In diffraction mode (modified from Ref [6]).

The role of the objective lens is to form the first intermediate image and diffraction pattern, which are then enlarged by subsequent projector lenses. The intermediate lens can be switched between the imaging mode and the diffraction mode, as shown in Fig. 3.3. In the image mode, the lens is focused on the image plane of the objective lens. The magnification of the final image projected onto the viewing screen depends on the strength of the projector lenses. In the diffraction mode, the intermediate lens is focused on the back focal plane and the diffraction pattern is projected onto the viewing screen.

The selected area diffraction (SAD) aperture, which is inserted at the first intermediate image plane, reduces the extend of illuminated regions to select the area of interest (Fig 3.4). Furthermore, it is useful to reduce the effect of spherical aberration on the diffraction pattern by removing the transmitted electrons outside the selected region. The objective aperture, which is located below the objective lens at the back focal plane, is used to select the diffracted electron beams that are allowed to contribute to the final image. For HRTEM images, a large aperture has to be used. For a bright-field (BF) image, the objective aperture is used to block all electron beams, except the direct beam. For a dark-field (DF) image, all but one of the diffracted beams is blocked (see Section 3.6).

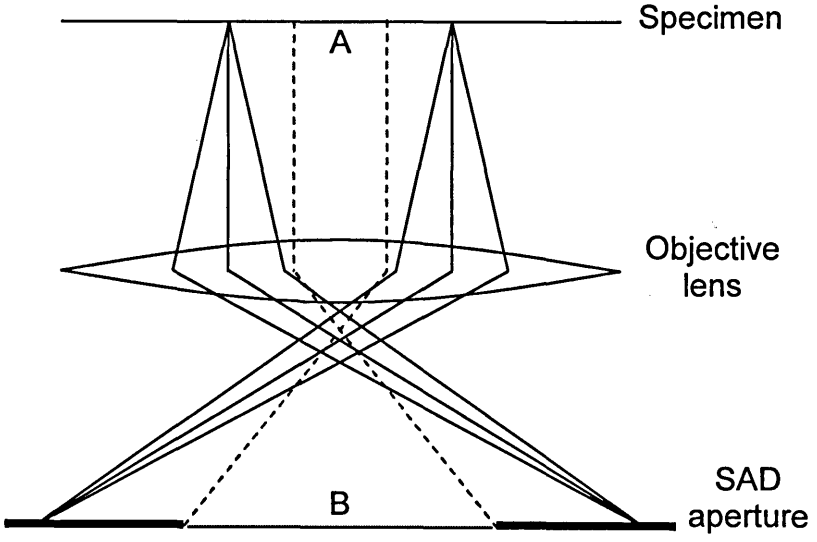

Fig. 3.4 Schematic diagram of SAD aperture which selects area B in the intermediate image is optically equivalent to selecting a smaller area A at the specimen.

3.2.5 The projector and the display system

The image produced by the objective lens is further magnified by a series of intermediate and projector lenses. Using several lenses, magnification of up to one million is easily achieved. Some microscopes have an energy filter to block inelastically scattered electrons which degrades image quality. It is also used in

quantitative interpretation of diffracted pattern intensities. Energy filters placed below the camera can give significant improvement to the image quality, as well as being part of an electron energy loss spectroscopy system.

The detection system is used to convert electron intensity in the TEM into an analogue image on a fluorescent viewing screen. Photographic plates and charge-coupled device (CCD) array cameras are utilised to record images. However, CCD camera usage is more widespread as its output can be computed with image processing software. The CCD camera can also be cooled to reduce noise and a longer exposure time is possible.

3.3 Aberrations in microscopy

In considering the image formation in electron microscopy, it is assumed that the image formed is only dependent of the final magnification since the paraxial electron beams were assumed constant and energetically homogeneous. These assumptions in a 'real' electron microscope are not justified because of lens aberrations or imperfections. An electromagnetic field is used in electron microscope lenses to deflect electron beams. However, the mechanically-flawed lens design and pole-piece fabrications, along with the mutual repulsion of electrons in constricted points (such as apertures, etc.) and the energy spread of electron beams result in loss of quality and resolution in the image [7]. The lens aberrations primarily responsible for the loss of performance in the microscope are spherical aberration, chromatic aberration and astigmatism.

3.3.1 Spherical aberration

Spherical aberration is the most important of a family of monochromatic aberrations. This aberration is caused by the lens field operating inhomogeneously away from the optic axis. The problem arises because the further off axis the electron beam, the more strongly it bends back towards the axis, thus to a focus

nearer to the lens, as shown in Fig. 3.5. As a result, a point object is imaged as an intense central bright region with a surrounding halo at the Gaussian image plane [8]. Hence, the resolution limited by spherical aberration is given by:

$$r_s = C_s \beta^3 \tag{3.5}$$

where C_s is the spherical aberration coefficient.

Typically, C_s is approximately equal to the focal length, hence a short focal length is preferable for HRTEM imaging. From Eq. (3.5), the maximum semiangle of collection of the aperture, β, strongly affects the resolution limited by spherical aberration. This clearly indicates that a smaller aperture results in improved resolution. Spherical aberration is most important in the objective lens as it degrades the final image in TEM. Besides that, spherical aberration in condenser lens will limit the resolution of the finest electron beam spot, affecting the performance of STEM [8]. In recent years, aberration correctors, utilizing octupoles and sextupoles lenses, are incorporated into electron microscopes to neutralize the effects of spherical aberrations [10, 11].

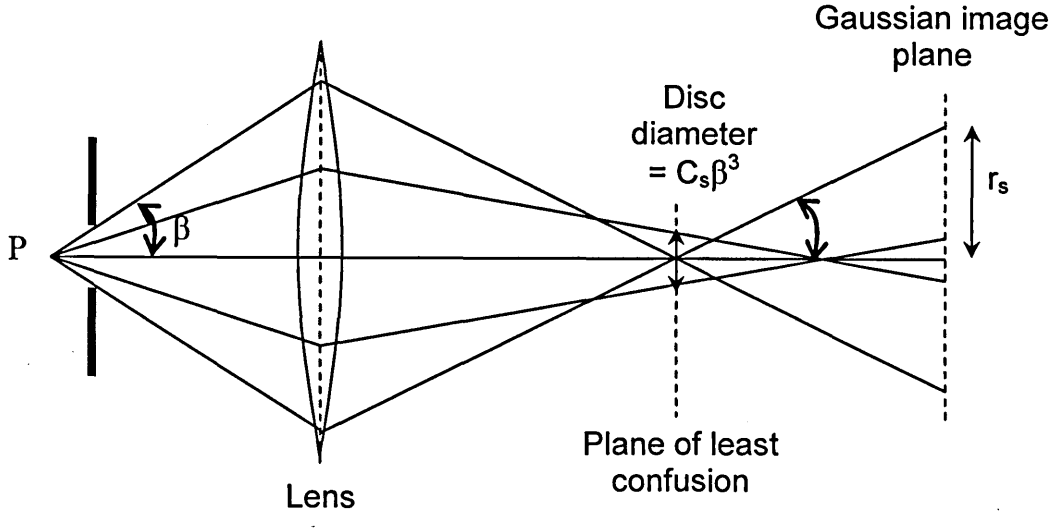

Fig. 3.5 Ray diagram illustrating spherical aberration in lens with associated disc of least confusion and a larger aberration disc at the Gaussian image plane (Modified from Ref [9]).

3.3.2 Chromatic aberration

Chromatic aberration depends on the spectrum of wavelengths and hence energy of the electrons. The electromagnetic lenses bend electrons of lower energy more strongly than electrons with higher energy. Thus, a point in the object P is brought into focus as a disc (Fig. 3.6). The radius of this disc is given by [8]:

$$r_c = C_c \frac{\Delta E}{E_o} \beta \tag{3.6}$$

where C_c is the chromatic aberration coefficient (like C_s it is approximately equal to the focal length), ΔE is the energy loss of the electrons, E_o is the initial beam energy.

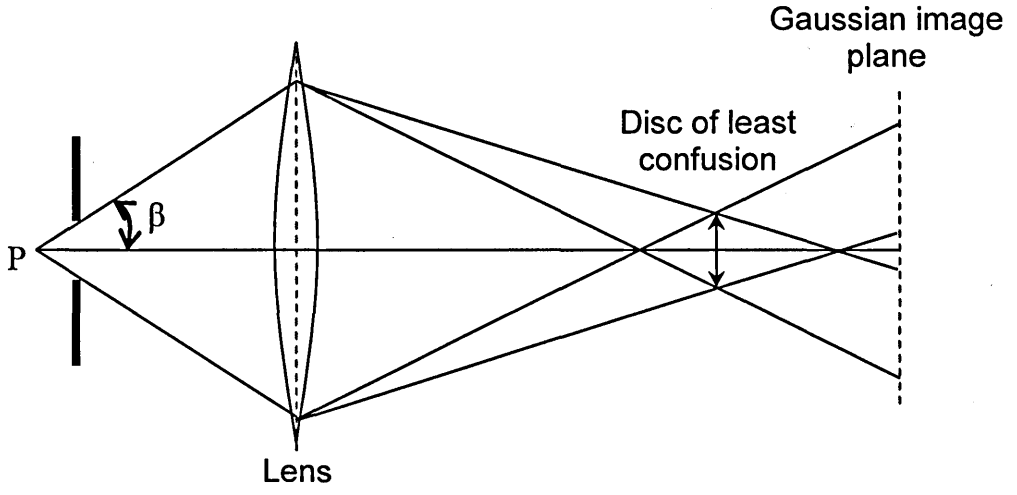

Fig. 3.6 Ray diagram illustrating chromatic aberration in lens. Light of shorter wavelength is brought into focus nearer to the lens compared to longer wavelength (Modified from Ref [9]).

The stability of the electron source and electromagnetic lenses is critical as these determine the spread of wavelengths emitted. However, modern FEGTEMs have excellent high tension power supplies and the variation of electron energy is negligible. Unfortunately, chromatic aberrations also occur

after interactions between the electron beam and the specimen where a whole range of electron energies emerge due to inelastic scattering. Similar to spherical aberration, smaller lens aperture improves the resolution of the image. A thicker specimen which results in greater energy loss will also degrade the resolution of the image due to chromatic aberration. Recently, a monochromator can be installed in a TEM or STEM to reduce the effects of chromatic aberrations [12, 13]. A monochromator is a precision energy filter which reduces the energy spread of the electron beam by dispersing the beam to a slit which excludes electrons of differing energies.

3.3.3 Astigmatism

Astigmatism occurs when electrons are affected by a nonuniform magnetic field as they spiral down the optic axis [8]. As a result, electron beams traversing in the horizontal plane are focused at a different point to those traversing in the vertical plane. This aberration arises due to physical imperfection in the electromagnetic lenses which causes local variations in the strength of the magnetic field. Furthermore, contamination in the column may also charge up and deflect the electron beam. A variety of combinations of astigmatism causes a distortion in the final image by:

$$r_a = \beta \Delta f \tag{3.7}$$

where Δf is the maximum difference in focus induced by astigmatism. Nonetheless, astigmatism can be easily corrected using stigmators, which are small octupoles that introduce a compensating field to counteract the asymmetric field.

PART II

3.4 Preparation of TEM specimens

In order to optimize the analytical results from a single TEM specimen, meticulous specimen preparation is very important. In particular, there is always a

risk that artefacts, which will limit the resolution of TEM imaging or cause misinterpretation of TEM images, might be introduced during the process of thinning the sample to electron-transparency. Furthermore, the TEM specimen should have a large, uniformly thin and stable electron-transparently thinned region. For semiconducting materials, the etching and electro-polishing TEM sample preparation techniques are not widely employed since there is rarely a chemical recipe that has the similar etching rate for all the components of semiconducting material [14]. Hence, an updated version of the traditional TEM sample preparation method which was developed by Bravman and Sinclair [15] was employed and is described below.

There are two kinds of mechanical sample preparation techniques, i.e. cross-sectional and plan view. The cross-sectional technique is normally used for studying the interfacial and inner structure of a sample. One of the most widely cross-sectioned samples is the semiconductor device, often grown epitaxially hence having numerous interfaces. With a cross-sectional specimen, one can determine the epitaxial layer thickness, its chemical composition and its structural integrity at the interface. Of course, a plan view specimen allows the TEM user to examine a larger area of interest of a semiconductor sample. This is mainly because the grown epitaxial layer is usually very much thinner than the overall thickness of the sample. Very near-surface information and the overall defect density can be obtained from plan view specimens. In both cases, the TEM specimens need to be thinned to electron transparency in the areas of interest by mechanical polishing and argon ion milling. Generally, a thinner specimen is better because inelastic scattering and dynamical scattering will be minimised, hence improving the quality of the TEM image and diffraction pattern. The following are the steps for making plan view and cross-sectional specimens, respectively.

3.4.1 Plan view specimen

Firstly, approximately 1 cm^2 of sample is mounted onto a piece of glass slide using low temperature wax, with the back of the sample facing upwards.

Secondly, the glass slide is waxed and placed onto a metal cylinder, which is part of a polishing block, as shown in Fig. 3.7. The polishing block and the metal cylinder are uniquely made from the same block of steel to give extra stability while grinding and polishing. Following that, the sample is mechanically ground with the polishing block, using different grades of silicon carbide abrasive papers, ranging from 240 (52 μm), 400 (22 μm), 800 (10 μm) and 1200 (5 μm) grit sizes according in this order. The grinding process should thin the specimen down to approximately 20-30 μm. A very thin sample is important because it reduces the total ion milling time, as well as producing a larger thin area with less thickness variation after ion milling.

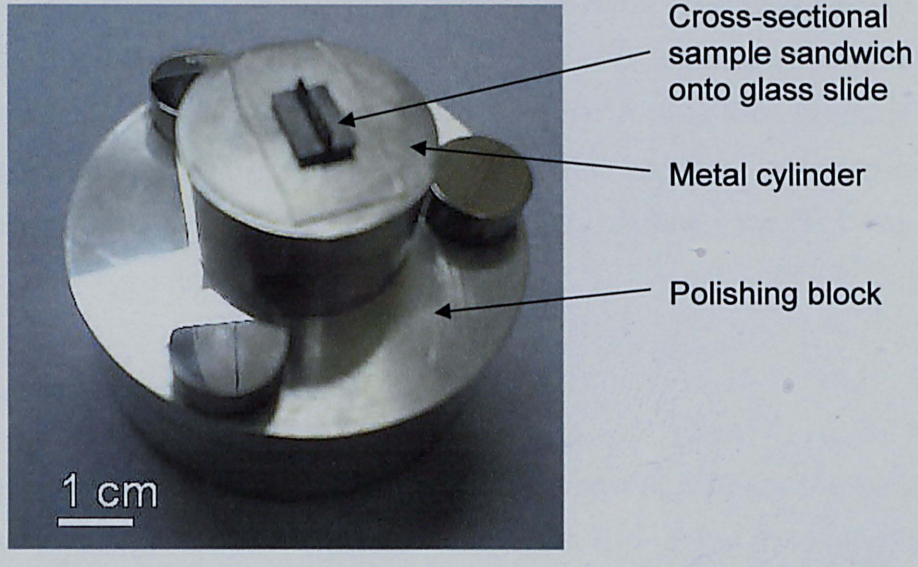

Fig. 3.7 Polishing block with sample sandwich and glass slide attached onto metal cylinder.

Subsequently, the sample is placed onto a polishing wheel with the polishing block. Polishing is an important aspect for sample preparation as the treated surface serves as one side of the final TEM specimen. Hence, it is important to reduce preparation-induced artefacts. The substance used for polishing is an ultra-fine diamond compound, starting from the 3-μm and followed by the 1 μm grit size compound (this may be followed by the ¼ μm

compound, if required). The polishing operation aims to produce a scratch-free planar surface on the sample, in preparation for ion beam milling.

Lastly, a 3.05 mm ceramic washer is glued onto the polished specimen using Defcon 5-minute two-part epoxy, to provide extra support. A ceramic washer is normally used instead of a brass or metal washer because it has a better thickness-strength ratio. Nonetheless, the ceramic washer is brittle and might cause a specimen-charging problem in the TEM holder. Although the washer offers a convenient way of moving the specimen with tweezers, it needs to be thinned sufficiently (<50 μm) in order to avoid blocking the beams of low angle ion beam milling which is to follow. After the glue has been cured, the excess material outside of the washer is carefully removed using a scalpel. Next, the specimen is removed from the glass slide, cleaned of residual wax with warm n-buthyl acetate and ethanol. The specimen is then carefully wiped clean with a small brush or a small piece of filter paper, as any wax or debris residue would produce artefacts during ion milling, before being transferred to the argon ion miller (see Section 3.5).

3.4.2 Cross-sectional specimen

The active sides of two rectangular pieces of sample (approximately 3mm x 10mm each) are bonded glued together using Gatan G-1 epoxy resin, which consists of two components, the hardener and the resin, with a mixing ratio of 1:10. This specialized epoxy is vacuum-compatible and resistant to most solvents. Besides that, the epoxy does not erode quickly when subjected to energetic ion beams and can be studied in a TEM hot stage at temperatures in excess of 1000°C [16]. At the sides of the sandwiched sample, silicon backing blocks are used to sandwich the glued pieces of sample, as shown in Fig. 3.8. Besides providing mechanical support during clamping, the silicon backing block is useful in preserving the sample surface during mechanical grinding and from frontal sputtering during ion milling. Furthermore, the silicon backing block can serve as

a "thickness indicator". As the specimen is mechanically-ground sufficiently thin (20-30 μm), red light is transmitted through the silicon backing block.

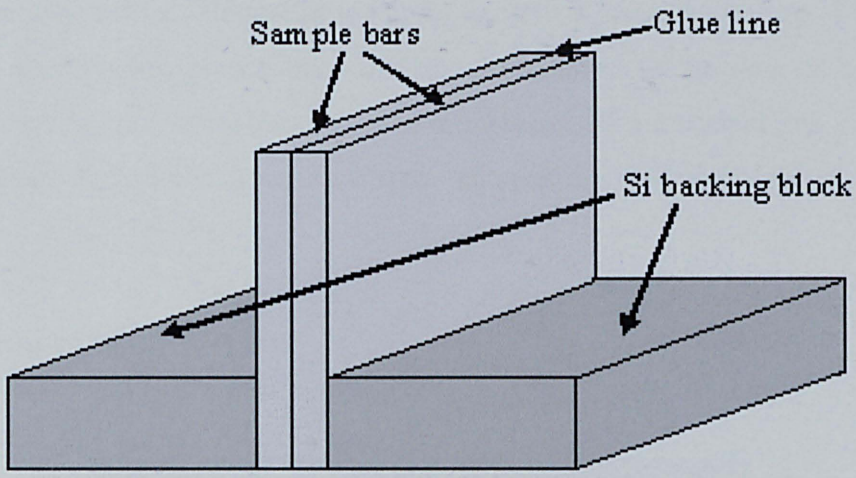

Fig. 3.8 Schematic diagram of cross-sectional sample sandwich

The sample sandwich is then inserted into a metal clamping device (Fig. 3.9) with spring-loaded vise, controlled by a screw, to hold the sandwich in place while ensuring the glue line is as thin as possible. In order to cure the epoxy, the glued sandwich is then baked in an oven at 100 °C for approximately 40 minutes and cooled down at room temperature. During this process, adequate pressure is applied, using the spring-loaded vise, onto the sandwiched sample, to ensure that the glue layer is as thin as possible (≤50 nm). This is necessary to ensure that the surface of the sample is not ion-eroded or damaged during the milling process.

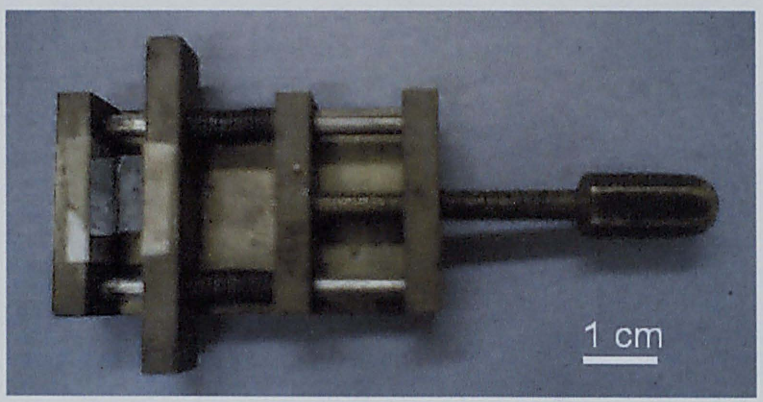

Fig. 3.9 A metal clamp with sample sandwich

Subsequently, the sample is mounted onto the glass slide and polishing block before it is ground and polished as described above for making plan view specimens. Next, the sample is turned over, and ground and polished in the same way until its thickness is approximately 20 μm. As before, 3.05 mm ceramic washers are placed onto the sample, centred at the area of interest. After removing excess material outside the washer with a scalpel and cleaning with warm n-buthyl acetate and ethanol, the specimen is transferred to the ion miller.

3.5 Ion milling

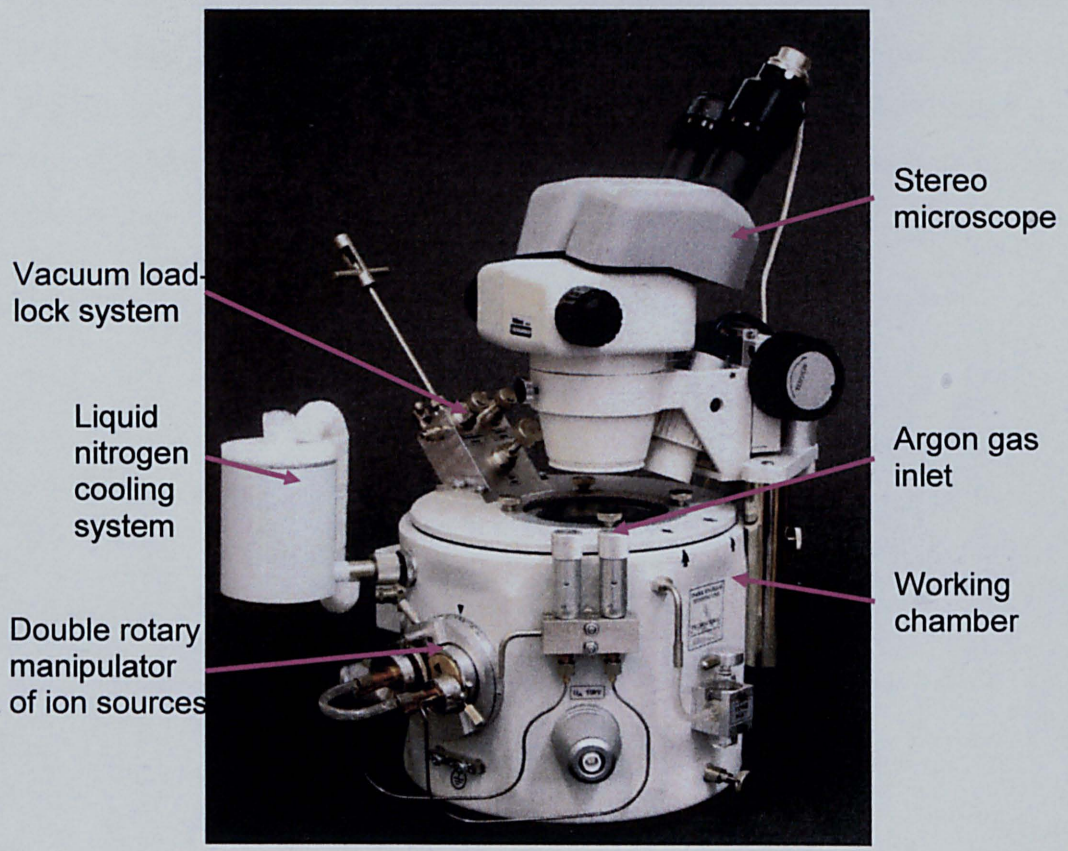

Fig. 3.10 Technoorg-Linda IV 4 miller (Note: the IV 3 model does not have the vacuum load-lock system)

Two different kinds of ion milling system have been available, namely the Leica EMRES 100 and the Technoorg-Linda IV 3 Argon Ion Beam Miller. The Technoorg-Linda IV 3 miller (Fig. 3.10), which is primarily used for this work, will be used as an example in this case.

After mounting a thinned and polished specimen onto a titanium specimen double sided holder, it is then loaded into the specimen chamber before allowing the chamber to vacuum pump until the operating vacuum of about $1x10^{-4}$ mbar. There are two high energy ion guns ("Teletwin" ion sources) in the ion miller. During ion-beam milling, argon (Ar) gas is ionised in the Teletwin ion source by ejected oscillating electrons. Ar atoms are chosen due to its high atomic number, inert nature and not naturally present in most samples [17]. The Ar ions are then accelerated from the gun through the cathode bore, bombarding the specimen. Upon impact on the specimen, the accelerated Ar ions displace atoms from the specimen, thus thinning and smoothing the intended specimen surface, a process known as sputtering.

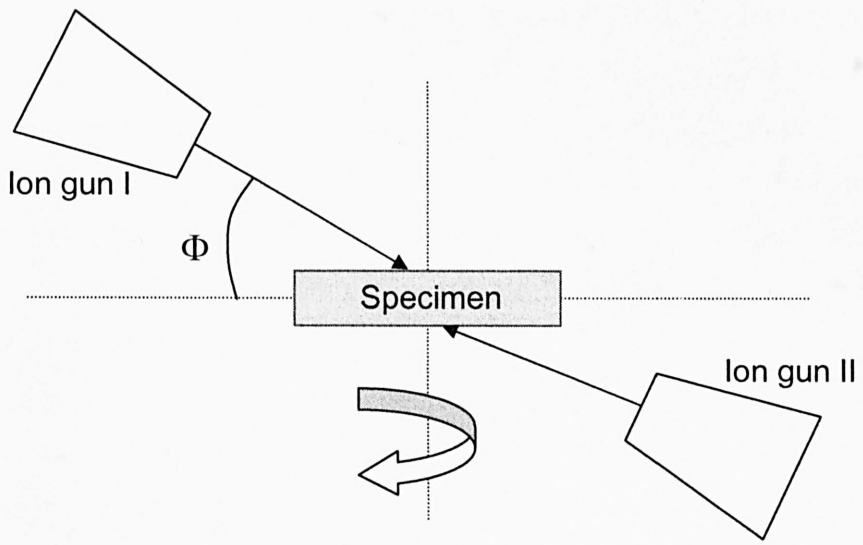

Fig. 3.11 Two ion guns tilted at angle Φ sputtering a specimen that is rotating or oscillating.

The theory of ion milling is very complex, where the sputtering rate and surface topographical quality is determined by numerous variables, namely the angle of ion incidence Φ (Fig. 3.11), rotation or oscillation, applied voltage and ion current of the ion guns, and sample heating. The ion guns are tilted to certain angles using the double rotary manipulator of ion sources. In general, the higher the ion milling angle, the higher the ion milling rate but the specimen surface also becomes rougher. The ion milling angles of $2^{\circ}<\Phi<8^{\circ}$ have been shown to be effective in preparing semiconducting materials with different milling rate [18]. Besides that, the application of low ion milling angles reduces thermal stress in the centre of the specimen [19]. In this work, the angle of incidence of approximately 7° is used, depending on the desired milling rate of the specimen and the thickness of the ceramic washer. Alternatively, milling can be initiated at a higher angle of incidence of $\sim 12^{\circ}$, before being lowered to around 7° much later, if the sample is extremely hard (e.g. GaN/Sapphire).

In practise, the specimen is rotated during ion milling to avoid the formation of unwanted directional grooves on the specimen surface (20). However, the oscillating mode (or rocking mode) is developed as it prevents damage or milling to the region of interest, which is normally in the vicinity of the glue line for cross section specimens. It is also known that the higher the ion gun voltage, the higher the ion milling rate. Nonetheless, it will also introduce a thicker amorphous layer and increases the roughness of the surface, which limits the resolution of TEM imaging. In practice, a high voltage is used initially (around 5 kV for GaAs), with the acceleration voltage reduced gradually just before perforation occurs until around 2 kV. Then, the sample is transferred to a Technoorg-Linda ion beam miller that is equipped with a low energy ion gun, with an operating range between 100V and 2 kV. Barna *et al.* has shown that non-detectable amorphisation of GaAs sputtered by milling ions of 0.25 kV [21, 22]. Furthermore, the high ion current density of the low energy gun is advantageous to prevent contamination as most of the ions impinging on the surface of the sample will be Ar ions [23].

The cooling of a specimen with liquid nitrogen during ion milling is advisable to avoid unwanted heating effects. It can also lead to cleaner surface because the materials sputtered during ion milling will be trapped on the surrounding cold area, instead of the thinned area. However, it is crucial that the specimen is allowed to warm up to room temperature after milling as the contaminant might redeposit onto the thinned area if the working chamber is opened immediately after milling. Another interesting feature of the Technoorg Linda miller is that it is also equipped with a sample holder having voltage bias. The sample holder voltage bias is useful to deflect the ion beam slightly in the vicinity of the sample to ensure a lower angle of incidence for ions impinging on the sample. While milling a plan view specimen, a glass cover slip is placed at the bottom of the specimen holder in order to prevent sputtering, redeposition of material and the destruction of features of interest in the specimen.

PART III

3.6 TEM imaging and spectroscopy

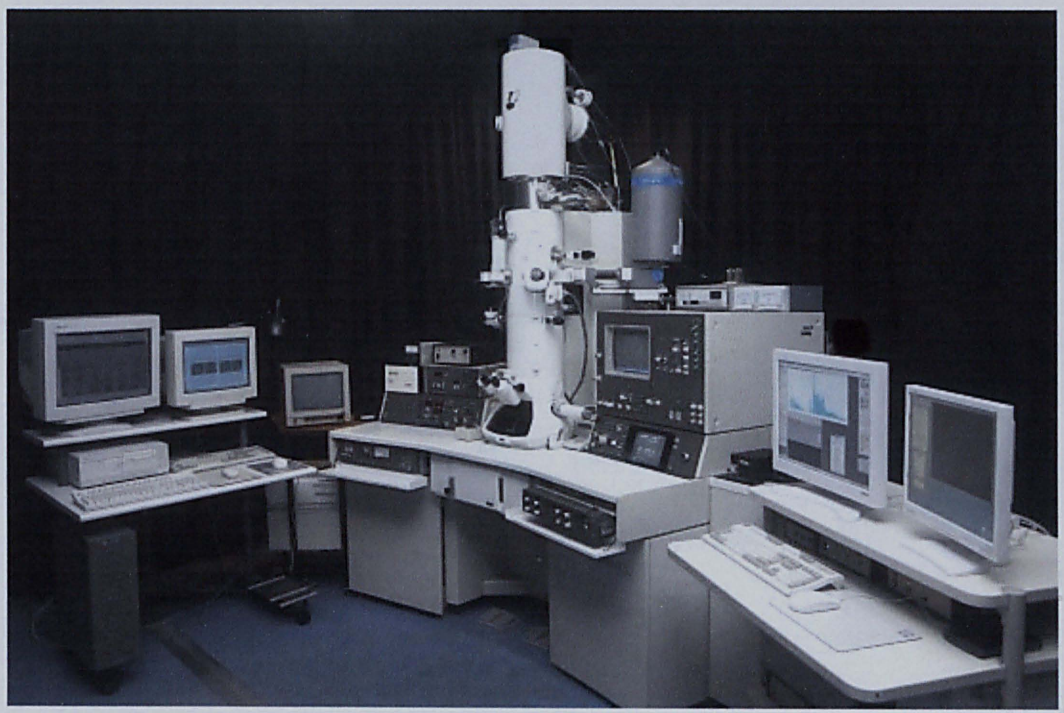

Fig. 3.12 JEOL JEM2010F field emission gun TEM in The University of Sheffield.

In this work, the TEM analysis is primarily carried out in a JEOL JEM2010F field emission gun TEM operating at 200 kV, as shown in Fig. 3.12. This instrument is able to provide structure analysis with a resolution of better than 0.19 nm by high-resolution imaging (C_s = 0.5 mm, C_c = 0.5 mm). The energy spread of the electron beam is approximately 1 eV. It is also equipped with a Gatan imaging energy filter (GIF), an EDX spectrometer, an EELS spectrometer, and a STEM unit with attached BF and HAADF detector. Furthermore, the JEOL JEM2010F employs a piezo-crystal specimen stage capable of translating a specimen with inter-atomic spacing accuracy. Therefore, the JEOL JEM2010F FEGTEM is specially equipped for both nanostructure imaging and spectroscopy.

3.6.1 Diffraction patterns

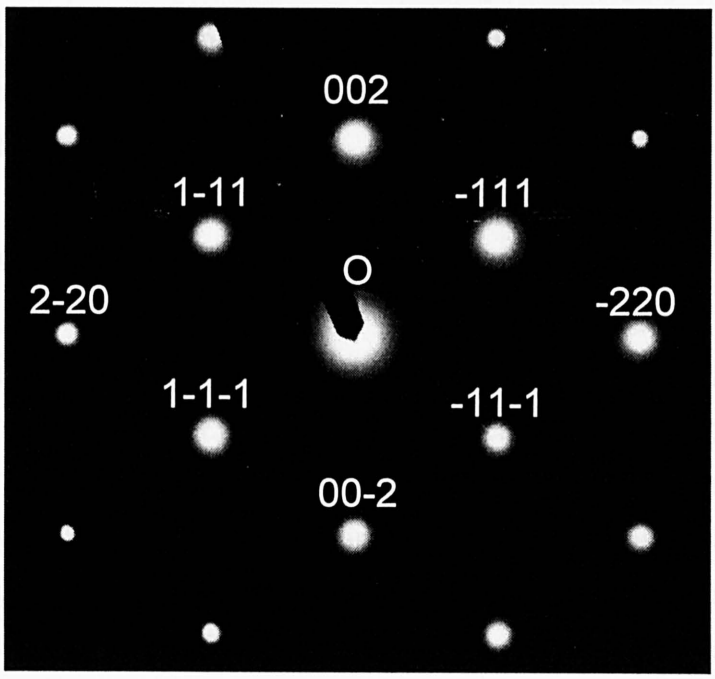

Fig. 3.13 Selected area TEM diffraction pattern from a GaAs crystal taken along the [011] zone axis. The directly transmitted beam is marked O, and the diffracted spots are indexed accordingly.

As mentioned in Section 3.2.4, a diffraction pattern is formed on the fluorescent screen if the intermediate lens is focused on the back focal plane of the objective lens in the TEM. As an electron beam passes through a specimen, the electrons that undergoes coherent elastic scattering are diffracted off the lattice planes according to the Bragg's law:

$$2d \sin \theta_B = n\lambda \tag{3.8}$$

where d is the atomic spacing, the integer n is the order of diffraction and θ_B is the Bragg angle. The electrons transmitted through the sample in a specific direction are brought into focus at the same point in the back focal plane. Indeed, the diffraction pattern can be used to provide crystallographic information.

A typical diffraction pattern from a GaAs crystal is shown in Fig. 3.13. The most intense spot is the transmitted beam, whereas the other spots define the directions in which the diffracted electron beams leave the crystal. The intensities of the diffracted spots are proportional to the square of the material structure factor, F_g. The scattering diffraction vector **g** is the vector from the transmitted beam to the diffracted beam.

3.6.2 Conventional TEM

Conventional TEM, which involves BF and DF imaging, utilizes diffraction contrast. For conventional TEM imaging, the objective aperture at the back focal plane is then used to allow either the transmitted beam or the diffracted beam to form the image. If only the transmitted direct beam is selected as shown in Fig.3.14 (a), a BF image is obtained. As opposed to BF, if any one diffracted beam is selected, then the resultant image is a DF image as illustrated in Figs. 3.14 (b) and (c).

In order to obtain good diffraction contrast for both BF and DF images, the specimen is tilted to "two-beam conditions", in which only one diffracted beam is strongly excited [24]. The DF image obtained under the two-beam condition contains specific orientation information. Anything that changes the

specimen atomic planes that results in Bragg diffraction will become visible, including dislocations, stacking faults and other crystallographic defects. Besides that, Bithell and Stobbs [25] have shown that the 200 reflection is chemically sensitive. The variation of dark field 200 contrast has been used to determine the composition of epitaxial layers [26]. For a III-V semiconductor material with composition of $A_xB_{(1-x)}C$ with atomic structure factors of F_A, F_B and F_C, the reflection intensity is given as [25]:

$$I \propto \left[xF_A + (1-x)F_B - F_C\right]^2 \tag{3.9}$$

In order to get the best contrast, especially for defect analysis, the specimen should not be exactly at Bragg condition (where the deviation parameter, **s** = 0). The deviation parameter **s** is a measure of the deviation from the Bragg condition of a reflection. Instead, the specimen should be tilted close to Bragg condition but with **s** small and positive to obtain the best possible strong beam contrast.

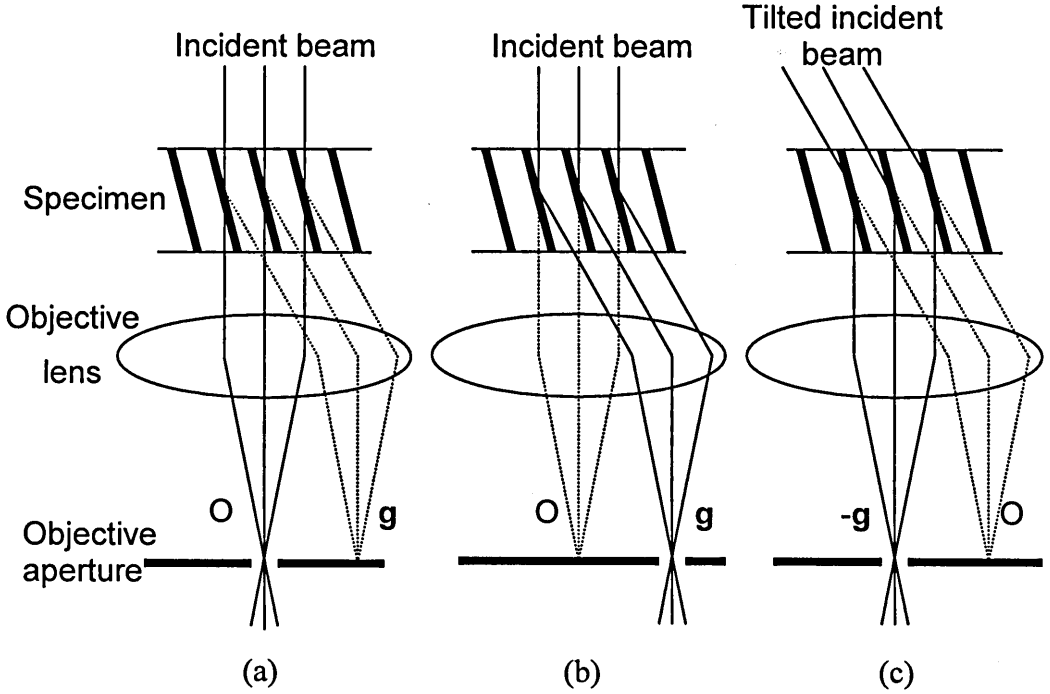

Fig. 3.14 Ray diagrams illustrate how the objective lens-aperture arrangement are used to produce (a) BF image, (b) "displaced-aperture" DF image and (c) "centred" dark field (CDF) image. 'O' and '**g**' represents the direct beam and the diffracted beam, respectively.

From Fig. 3.14 (b), the objective aperture is displaced off-axis to select a particular diffracted beam to obtain a "displaced-aperture" DF image. However, severe imaging aberrations are likely to be introduced since the imaging electrons are traversing far from the optic axis, where spherical aberration is large. The solution is to tilt the primary electron beam so that the chosen diffracted beam travels along the optic axis to the centred objective aperture as shown in Fig. 3.14 (c). In order to achieve that, the transmitted direct beam is tilted so that the weakly excited $-\mathbf{g}$ reflection is brought towards the centre of the screen. As the initially weakly excited $-\mathbf{g}$ beam approaches the optic axis, it becomes strongly excited [25].

3.6.3 High resolution transmission electron microscopy

High resolution TEM uses phase contrast to obtain high resolution structure images. As the coherent incident beam travels through the specimen, the transmitted scattered electrons incur phase changes. The relative phase change depends on many factors, such as the specimen thickness, orientation and scattering factor of the specimen, the coherence of the electron beam and the quality of the TEM lenses [27]. While phase contrast imaging can be used at low magnification, a very important application is HRTEM. A phase contrast image requires the selection of more than one beam. Each pair of diffraction spots selected by the objective aperture will in principle produce a set of interference fringes in the image which represent periodic parallel atomic planes. The strong bright and dark fringes are produced by the interactions of constructive and destructive interference of the electron waves when forming the phase contrast image.

In theory, the more beams collected, the higher the resolution of the lattice-fringe image. Therefore, normally the largest objective aperture is used. Furthermore, a crystalline specimen is normally tilted such that the incident beam is parallel to one of the zone axis in the crystal, to produce many strong diffracted beams. The many intersections of lattice fringes give rise to a pattern of dark (or bright) spots which correspond to individual atomic columns. Despite

the apparent clarity of HRTEM images, the direct interpretation of these contrasts is difficult as the image contrast changes with specimen thickness and lens focus [28]. Hence, most HRTEM images cannot be fully interpreted unless they are compared with a series of computer-generated images simulated from the likely structures [29, 30].

To obtain the best possible HRTEM image resolution, the microscope must be carefully aligned. Besides that, the objective astigmatism should also be corrected using the objective stigmators. Good HRTEM images require a flat and thin (<50 nm) TEM specimen to minimize inelastic scattering which degrades the image quality. High quality HRTEM imaging also requires a specimen that is free from artefacts such as contamination or and amorphous layer created due to ion beam damage and redeposition. Low energy ion milling during the final thinning can reduce such artefacts (See section 3.5) [31]. The theoretical image contrast of HRTEM which is governed by the Contrast Transfer Function (CTF), T(**u**), is given as [32]:

$$T(u) = 2A(u)E(u)\sin\chi(u) \tag{3.10}$$

where **u** is the reciprocal-lattice vector with the spatial frequencies in nm^{-1}, T(**u**) is the contrast transfer function, A(**u**) is the aperture function, E(**u**) is the envelope function and χ(**u**) is the phase distortion function. The phase distortion function, χ(**u**), which describes the phase difference that is introduced by spherical aberration and defocus is given as [33]:

$$\chi(u) = \pi\Delta f\lambda u^2 + \frac{1}{2}\pi C_s\lambda^3 u^4 \tag{3.11}$$

where λ is the electron wavelength, **u** is the recriprocal-lattice vector, C_s is the spherical aberration coefficient, and Δf is the defocus of the objective lens.

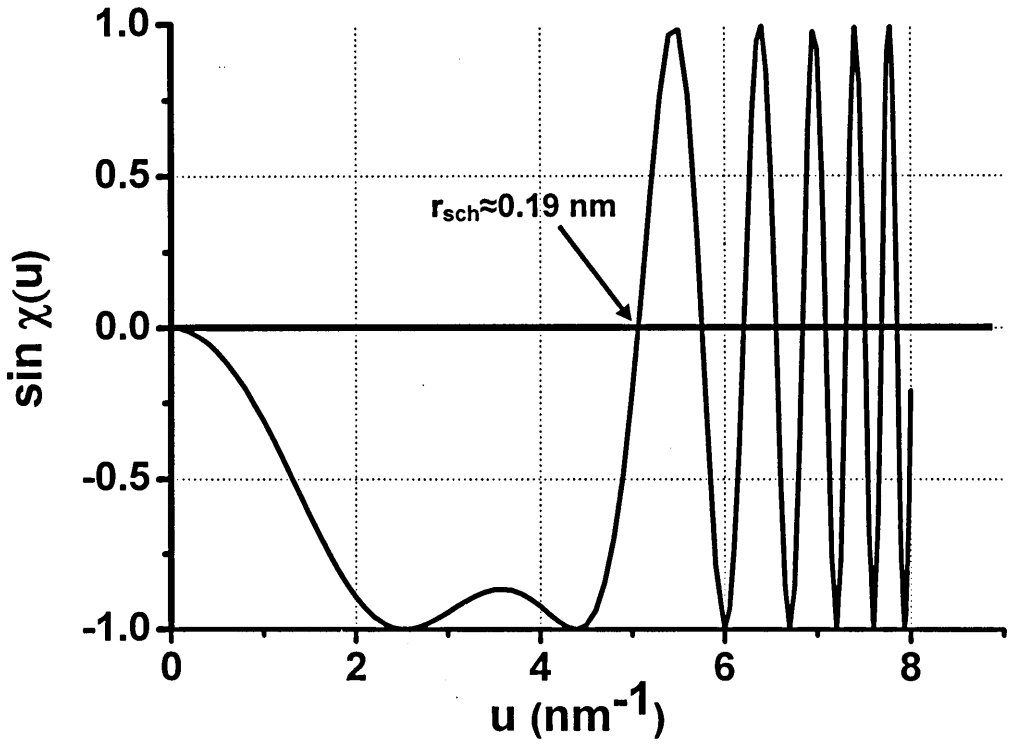

Fig. 3.15 Plot of the phase distortion function sin $\chi(\mathbf{u})$ against **u** at Scherzer defocus for JEOL JEM2010F FEGTEM operating at 200kV.

Since A(**u**) and E(**u**) is fixed for a given microscope, $\chi(\mathbf{u})$ determines the the phase contrast image resolution of the HRTEM. From Eq. (3.11), $\chi(\mathbf{u})$ depends strongly on the values of C_s (the lenses quality), λ (the accelerating voltage, where $\lambda = \frac{h}{\sqrt{2meV}}$), Δf and **u**. The instrumental point resolution, which represents the limit where the image is directly interpretable, is defined by the first intersection between the sin $\chi(\mathbf{u})$ curve and the **u**-axis.

Scherzer (1949) discovered that the transfer function can be optimised by applying a particular defocus to balance the effect of C_s [32]. The "Scherzer defocus", Δf_{sch}, is defined by:

$$\Delta f_{Sch} = -(\frac{4}{3} C_s \lambda)^{\frac{1}{2}} \qquad (3.12)$$

The crossover at **u**-axis with Δf_{sch} is given as:

$$u_{sch} = 1.51 C_s^{-\frac{1}{4}} \lambda^{-\frac{3}{4}} \tag{3.13}$$

Hence, the ideal resolution of HRTEM image at Scherzer defocus, r_{sch}, which is the reciprocal of u_{sch}, is defined by:

$$r_{sch} = 0.66 C_s^{\frac{1}{4}} \lambda^{\frac{3}{4}} \tag{3.14}$$

From Eq. (3.14), the instrumental resolution limit for the JEOL JEM2010F FEGTEM operating at 200kV (C_s = 0.5 mm and $\lambda \approx 0.00251$ nm) is calculated as approximately 0.19 nm. The ideal CTF (represented by sin $\chi(\mathbf{u})$) for this TEM is plotted as a function of u in Fig. 3.15. Negative sin $\chi(\mathbf{u})$ results in positive phase contrast where atoms appear dark against a bright background. Conversely, for a positive sin $\chi(\mathbf{u})$, the opposite occurs.

3.6.4 Scanning transmission electron microscopy

STEM utilises a convergent atomic-scale electron probe which scans across the specimen and collects the transmitted elastically scattered electrons with annular detectors. The resolution of a STEM image is limited by the diameter of the probing beam. In order to achieve a very fine probe size, the C1 lens is strongly excited to create a crossover between both the condenser lenses, and hence a large demagnification of the electron source is achieved. Subsequently, the C2 condenser lens and other gun lenses are used to tune the electron probe further [34]. As shown in Fig. 3.16, the STEM scanning coils between the C2 condenser lens and the upper objective lens pole-piece deflect the electron beam, while ensuring that the beam is parallel to the optic axis.

The tuning and optimization of the electron beam can be performed readily with the electron "Ronchigram" or "shadow image" [35, 36]. Any slight misalignment of the lenses, especially the condenser lens astigmatism, results in distortions in the Ronchigram pattern (circularly symmetric when perfectly aligned as seen in Fig. 3.17). Furthermore, the presence or absence of interference fringes in the Ronchigram can help to indicate the amount of incoherent beam

broadening due to instabilities and the effects of a finite source size. Also, at large defocus, the specimen can be tilted to the desired zone axis because the crystal Kikuchi lines in the Ronchigram can be clearly seen. Kikuchi lines, which are caused by the interaction between elastically and inelastically scattered electrons, may be used to determine the orientation of a crystalline specimen. In this work, the STEM images are taken along the <110> zone axis; the reasons are given in the following section.

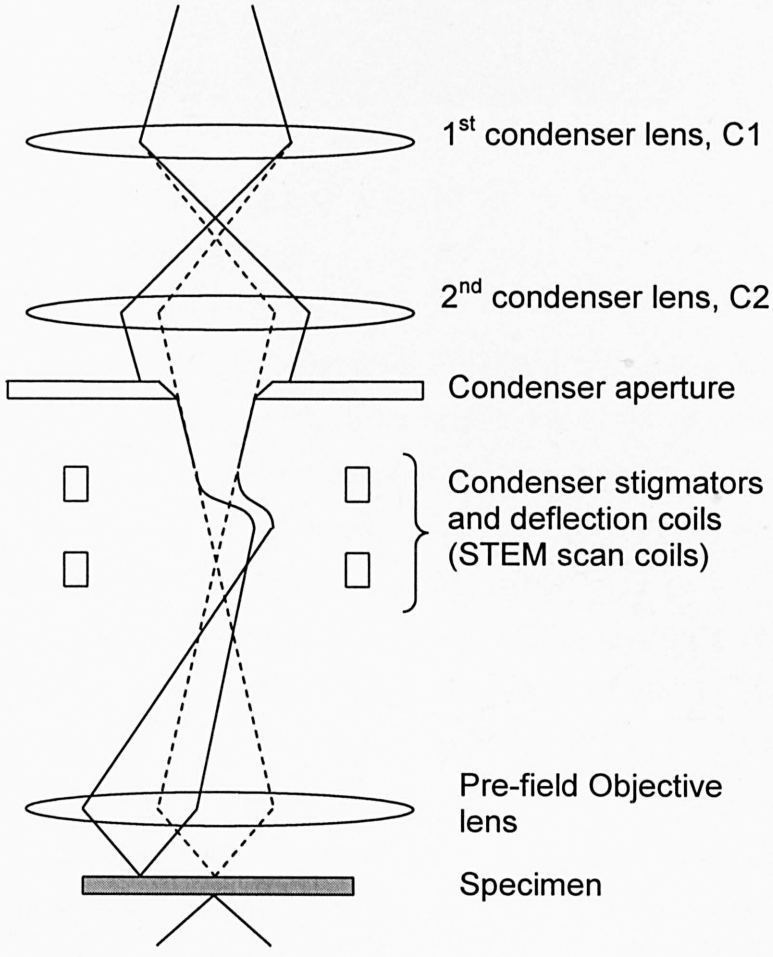

Fig. 3.16 Schematic ray diagram showing convergent electron probe for STEM image formation using STEM scan coils.

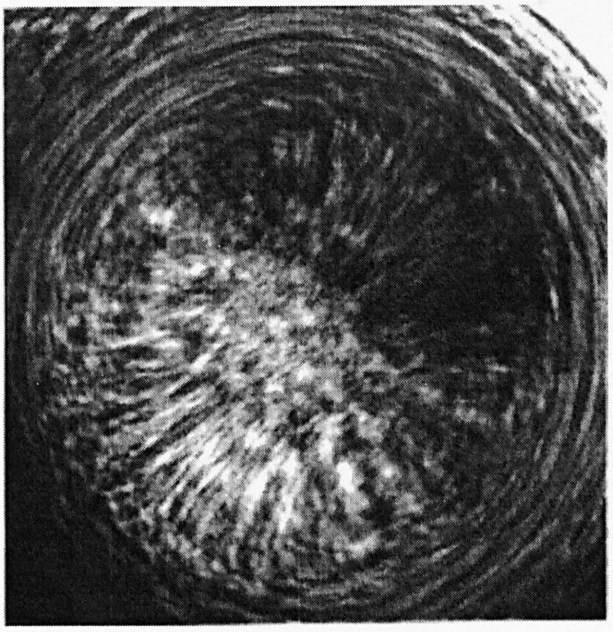

Fig. 3.17 Typical Ronchigrams obtained at the amorphous edge of a specimen (modified from Ref [36]).

In this work, the JEOL JEM2010F FEGTEM was equipped with a BF and a HAADF detector. The main difference between the BF and HAADF detector for STEM is the collection angle. A BF detector collects electrons that are scattered less than 10 mrad, whereas the HAADF image is formed from electrons that are scattered more than 50 mrad. The principle of forming BF and DF images in STEM is comparable to that of diffraction contrast in conventional TEM, where the BF detector collects the direct beam and the HAADF detector collects the diffracted beams. However, the resultant diffraction contrast STEM image will generally be poorer to that of conventional TEM image, due to the different imaging conditions. At smaller collection angle, the diffraction contrast can be increased at the expense of increased noise in the STEM image [37]. Nevertheless, in general STEM diffraction contrast images compare unfavourably with conventional TEM images.

As mentioned earlier, HAADF imaging collects high-angle scattered electrons (50-150 mrad). HAADF images are also known as Z-contrast images

because the intensity of the images depends very strongly on the composition; proportional to Z^2 where Z is the atomic number of the material [38]. For a thin crystalline material tilted to a major zone-axis, if the probe size is relatively fine compared to the atomic spacing, HAADF images with atomic resolution can be produced, where the intensity of an individual atomic column directly reflects its composition [36, 38]. Hence, in principle, an HAADF image of a specimen with uniform thickness represents an elemental map. Furthermore, HAADF images have the advantage where the imaging contrast is generally unaffected by small changes in the objective lens defocus and specimen thickness [37].

3.6.5 Electron energy loss spectroscopy and energy filtered transmission electron microscopy

Electron energy loss spectroscopy is the study on the energy distribution of scattered electrons that have interacted inelastically with the specimen. Inelastic scattering occurs due to Coulomb interactions between incident electrons and the "atomic electrons" surrounding the nucleus. During the event of an inelastic scattering, the inner-shell electron can make an upward transition to an unoccupied electron state above the Fermi level only if it absorbs energy that is equal to or greater than its original binding energy [39]. As a result, the transmitted incident electrons lose a similar amount of energy, forming an ionization edge in an EELS spectrum as shown in Fig. 3.18. Since the inner-shell binding energy depends on the atomic number of the scattering atom, the ionization edges in the EELS spectrum would identify the elements that are present in the specimen. Fig. 3.19 shows an EELS spectrum with zero-loss peak and low loss region. The zero-loss peak, which represents transmitted electrons without any significant or no energy loss, is usually used to determine the overall resolution of the spectrum. The low loss region, which extends from 5-50 eV, is contributed by the excitation of electrons in the outermost atomic orbitals. Also, the low loss region is dominated by collective, resonant oscillations of the valence electrons known as plasmons [40].

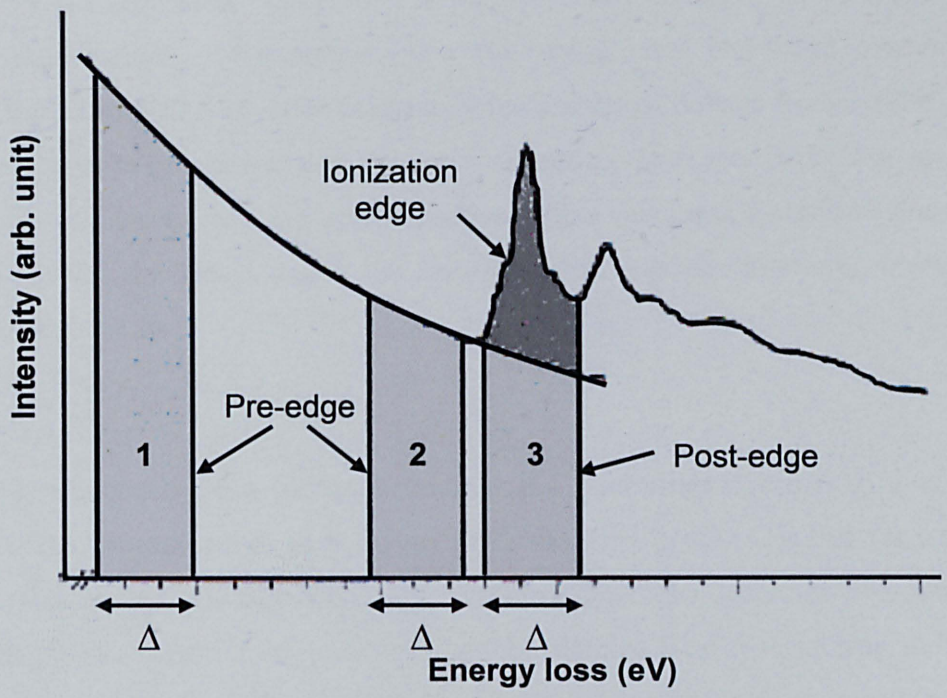

Fig. 3.18 Schematic diagram of an EELS spectrum showing an ionization edge with the three-window background subtraction method. The positions of pre-edge and post-edge energy windows, with an energy window width Δ, are indicated with shaded areas.

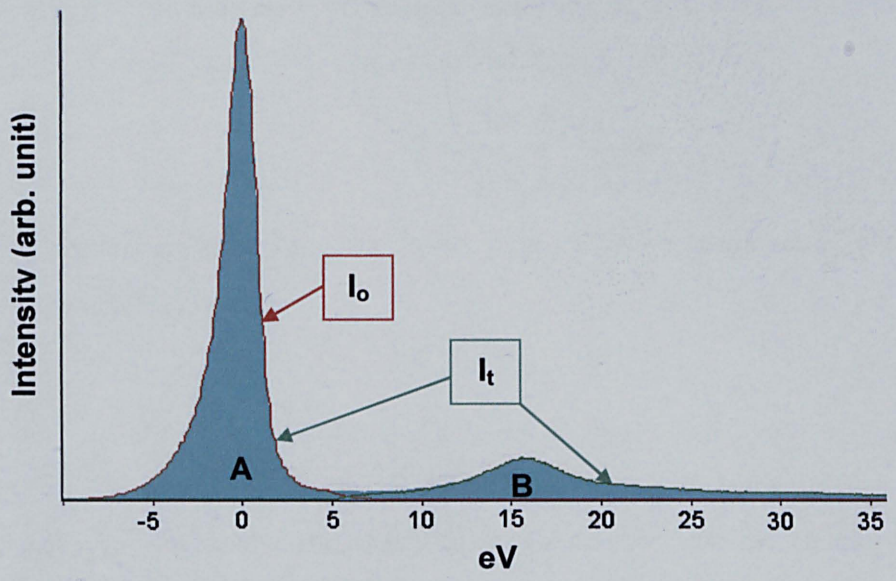

Fig. 3.19 EELS spectrum showing the definations of the zero-loss intensity I_o and the total intensity I_t required to measure specimen thickness via the log-ration method. "A" denotes the zero-loss peak whereas B is the low loss region which extends from 5 to 50 eV.

In this work, sometimes it was necessary to know the thickness of a TEM specimen, for example when converting areal elemental concentration provided by EELS or when calculating the density of defects from a TEM image. It is generally known that inelastic scattering increases with the specimen thickness. Hence, a good approximation of the thickness t can be obtained by comparing the area I_o under the zero-loss peak with the total area I_t under the spectrum [41]:

$$\frac{t}{\lambda_t} = In\left(\frac{I_t}{I_o}\right) \tag{3.15}$$

where λ_t is the mean free path for inelastic scattering. Hosoi *et al.* has shown that the formula gives an accuracy of ±10% for $t/\lambda_t < 5$ [42]. But for $t/\lambda_t < 0.1$, surface excitations may cause an overestimation of the specimen thickness [43]. The absolute specimen thickness can be obtained by determining λ_t for the specimen [44]:

$$\lambda_t = \frac{106FE_o}{E_m In\left(2\beta\frac{E_o}{E_m}\right)} \tag{3.16}$$

where β is the collection semiangle (in mrad), E_o is the incident electron energy (in keV) and F is a relativistic correction factor defined by:

$$F = \frac{1+E_o/1022}{\left(1+E_o/511\right)^2} \tag{3.17}$$

E_m, which is the average energy loss (in eV) for a material of average atomic number Z, is given by:

$$E_m \approx 7.6Z^{0.36} \tag{3.18}$$

Elemental mapping in EFTEM is obtained by selecting a range of energy loss which corresponds to an inner-shell ionization edge to produce two-dimensional chemical information from the imaged area. This is achieved by employing a magnetic prism spectrometer with an energy selecting slit to allow the transmission of electrons of a particular energy loss. However, every inner-shell ionization edge is superimposed on a strong background signal, as

shown in Fig. 3.18. To obtain a reliable elemental map, a suitable background subtraction method must be employed to obtain the intensity of the ionization edge intensity of interest.

There are two commonly used methods to eliminate the background signals in elemental mapping. The first method involves dividing the post-edge image with a pre-edge image, yielding a "jump-ratio" image [45]. A jump ratio image is largely unaffected by the variations in specimen thickness and diffraction effects [46]. However, this method is unsuitable for quantitative analysis due to plural-scattering background components [47]. In this work, the background subtraction is conducted using the "three-window" method [46]. As shown in Fig. 3.18, the three-window method involves recording two pre-edge images and a post-edge image with the same energy slit width. The two pre-edge images are used to extrapolate the background image. The background image is then subtracted from the post-edge image in order to obtain an elemental map, where the image intensity is proportional to the elemental concentration. Although there are numerous background subtraction fittings (such as power-law, polynomial and log-polynomial), the fit of the background intensity employed in the present work is the power-law fit [48]:

$$I = AE^{-r} \tag{3.19}$$

where I is the intensity, E is the energy loss from the two pre-edges, and A and r are two fitting parameters.

3.7 References

[1] S. Wischnitzer, *Introduction to Electron Microscopy*, Third Edition, Pergamon Press, Singapore, (1989), pp. 38-56.

[2] D. B. Williams and C. B. Carter, *Transmission Electron Microscopy*, Plenum Press, New York, (1996), p. 69.

[3] P. J. Goodhew, J. Humphreys, R. Beanland, *Electron Microscopy and Analysis,* Third Edition, Taylor and Francis, (2001), p.26.

[4] D. B. Williams and C. B. Carter, *Transmission Electron Microscopy*, Plenum Press, New York, (1996), pp.69-77.

[5] P. J. Goodhew, J. Humphreys, R. Beanland, *Electron Microscopy and Analysis,* Third Edition, Taylor and Francis, (2001), pp.67-69.

[6] P. J. Goodhew, J. Humphreys, R. Beanland, *Electron Microscopy and Analysis,* Third Edition, Taylor and Francis, (2001), pp.71, 72.

[7] L. E. Murr, *Electron and ion microscopy and microanalysis: principles and applications*, Second Edition, Marcel Dekker, (1991), pp. 120-132.

[8] D. B. Williams and C. B. Carter, *Transmission Electron Microscopy*, Plenum Press, (1996), pp.97-99.

[9] P. J. Goodhew, J. Humphreys, R. Beanland, (2001), *Electron Microscopy and Analysis,* Third Edition, Taylor and Francis, pp.14-16.

[10] M. Haider, G. Braunshausen, E. Schwan, Optik, **99** (1995) 167.

[11] O. L. Krivanek, N, Dellby, A. R. Lupini, Ultramicroscopy, **78** (1999) 1.

[12] H. Rose, Optik, **85** (1990) 95.

[13] H. W. Mook, P. Kruit, Ultramicroscopy, **81** (2000) 129.

[14] R. Anderson, Microsc. Microanal., **4** (1999) 467.

[15] J. C. Bravman, R. Sinclair, J. Elec. Microsc. Tech., **1** (1984) 53.

[16] Data Sheet G-1/G-2 Epoxy, Gatan Inc., P/N 601.00005, revision 2.

[17] D. B. Williams and C. B. Carter, *Transmission Electron Microscopy*, Plenum Press, New York, (1996), p. 163.

[18] A. Barna, Mater. Res. Soc. Proc., **254** (1992) 3.

[19] B. Viguier, A. Mortensen, Ultramicroscopy, **87** (2001) 123.

[20] P. J. Goodhew, *Practical Methods in Electron Microscopy*, Vol. 11, Elsevier, (1985), p.107.

[21] A. Barna, B. Pecz, M. Menyhard, Ultramicroscopy, **70** (1997) 161.

[22] A. Barna, B. Pecz, M. Menyhard, Micron, **30** (1999) 267.

[23] J. C. G. Carpenter, J. A. Jackman, J. P. McCaffrey, R. Alani, J. Mic. Soc. America, **1** (1995) 175.

[24] D. B. Williams and C. B. Carter, *Transmission Electron Microscopy*, Plenum Press, New York, (1996), p. 361.

[25] E. G. Bithell and W. M. Stobbs, Philos. Mag. A, **60** (1989) 39.

[26] R. Beanland, Ultramicroscopy, **102** (2005) 115.

[27] D. B. Williams and C. B. Carter, *Transmission Electron Microscopy*, Plenum Press, New York, (1996), p. 441.

[28] P. J. Goodhew, J. Humphreys, R. Beanland, *Electron Microscopy and Analysis,* Third Edition, Taylor and Francis, (2001), pp. 106-108.

[29] L. Olsen, J. C. H. Spence, Philos. Mag. A, **43** (1980) 945.

[30] D. Cherns, J. C. H. Spence, G. R. Anstis, J. L. Hutchison, Philos. Mag. A, **46** (1982) 849.

[31] N. G. Chew, A. G. Cullis, Ultramicroscopy, **23** (1987) 175.

[32] D. B. Williams and C. B. Carter, *Transmission Electron Microscopy*, Plenum Press, New York, (1996), pp. 459-466.

[33] J. M. Cowley, *Imaging Theory in High-Resolution Transmission Electron Microscopy and Associated Techniques*, edited by P. Buseck, J. Cowley, and L. Eyring, Oxford University Press, (1992) p. 38.

[34] N. D. Browning, I. Arslan, Y. Ito, E. M. James, R. F. Klie, P. Moeck, T. Topuria, and Y. Xin, J. Electron Microscopy, **50** (2001) 205.

[35] J. M. Cowley, J. Elec. Microsc. Tech., **3** (1986) 25.

[36] N. D. Browning, E. M. James, K. Kishida, I. Arslan, J. P. Buban, J. A. Zaborac, S. J. Pennycook, Y. Xin, and G. Duscher, Rev. Adv. Mat. Sci., **1** (2000) 1.

[37] D. B. Williams and C. B. Carter, *Transmission Electron Microscopy*, Plenum Press, New York, (1996), pp. 364-366.

[38] S. J. Pennycook, Annu. Rev. Mater. Sci., **22** (1992) 171.

[39] R. F. Egerton, *Electron Energy Loss Spectroscopy in the Electron Microscope*, Plenum, New York, (1996), pp. 2-7.

[40] R. Brydson, *Electron Energy Loss Spectroscopy*, BIOS, Oxford, (2001), pp. 29-32.

[41] D. B. Williams and C. B. Carter, *Transmission Electron Microscopy*, Plenum Press, New York, (1996), pp. 678-679.

[42] J. Hosoi, T. Oikawa, M. Inoue, Y. Kokubo, and K. Hama, Ultramicroscopy, **7** (1981) 147.

[43] P. E. Batson, Ultramicroscopy, **50** (1993) 1.

[44] R. F. Egerton, *Electron Energy Loss Spectroscopy in the Electron Microscope*, Plenum, New York, (1996), pp. 302-307.

[45] A. J. Grubbens, O. L. Krivanek, Ultramicroscopy, **51** (1993) 146.

[46] R. F. Egerton, *Electron Energy Loss Spectroscopy in the Electron Microscope*, Plenum, New York, (1996), pp. 330-334.

[47] F. Hofer, P. Warbichler, and W. Grogger, Ultramicroscopy, **25** (1995) 15.

[48] R. F. Egerton, *Electron Energy Loss Spectroscopy in the Electron Microscope*, Plenum, New York, (1996), pp. 120-123.

Chapter 4

Structural studies of InAlAs-InGaAs capping layer on InAs/GaAs quantum dots with 1.3-μm emission

4.1 Introduction

Investigation of self-assembled QDs grown via the S-K growth mode has been extensively carried out to study both the physics and potential optoelectronic device applications of zero-dimensional semiconductor structures [1]. Indeed, the formation of the dots themselves has been shown [2, 3] to be driven by the surface segregation of the misfitting element: in the case of dots in the In(Ga)As/GaAs system, this is elemental indium (see Section 2.10.2). Research on GaAs-based QD lasers emitting at the important telecommunication wavelength of 1.3-μm has progressed rapidly [4-7] because the loss in optical fibers has window minima at around 1.3-μm, as shown in Fig. 4.1. However, their performances are being hampered by gain saturation caused by low dot density, and increased temperature sensitivity.

During the growth of QDs, there is a minimum separation between islands (inter-island distance, d) due to the repulsive strain field in the underlying layers, hence limiting the density of dots [8]. In addition, the strain-induced interaction is proportional to the square of the lattice mismatch between the QDs and the underlying buffer layer. In other words, this interaction will decrease drastically when a strained buffer layer is utilized and hence, increasing the dot density significantly [9]. Indeed, the growth of InAs QDs directly deposited on an InGaAs strained buffer layer (SBL) has been widely utilized to increase the QD

density [9-12]. However, the InGaAs SBL decreases the confinement potential, resulting in a reduction of energy separation between the discrete energy level of the QDs [13]. This leads to a degradation of the laser performance, notably increasing temperature sensitivity due to thermal carrier escape. In order to rectify this detrimental effect, Liu *et al.* proposed using a combined InAlAs-GaAs SBL to both increase the lattice parameter and the potential barrier of the buffer layer [14].

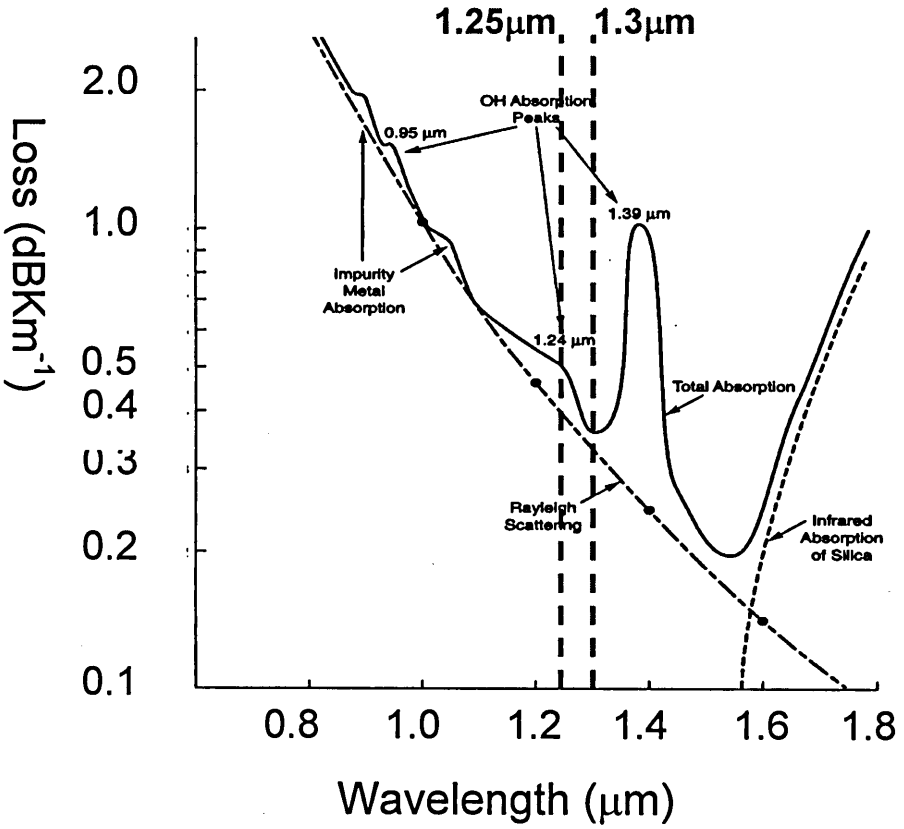

Fig. 4.1 Fiber loss versus wavelength in optical fibers.

The deposition of an InGaAs strain-reducing capping layer (SRL) above the InAs/GaAs QDs has been widely employed in order to extend the emission wavelength to 1.3-μm or longer [4, 5, 15, 16]. Just like the InGaAs SBL, this growth technique results in a decrease in the confinement potential barrier which consequently reduces the energy separation between the QD ground and first-excited states [13]. Instead of using a conventional InGaAs or GaAs

capping layer, an InAlAs-InGaAs combined two-level capping layer has been developed to increase the confinement of the InAs QDs for advanced laser applications [17-20]. As shown in Fig. 4.2, Liu *et al.* [17] have demonstrated that the room-temperature ground-state PL intensity of 1.3-μm InAs/GaAs QDs is increased substantially, by a factor of approximately 450, when the InAlAs layer thickness was increased from 1.5 to 6.0 nm. A large energy separation between the ground and the first-excited state of 108 meV has been obtained by this growth technique [21]. In addition, the increasing ground-state emission wavelength has been demonstrated by using an AlAs capping layer, instead of GaAs or InGaAs [22].

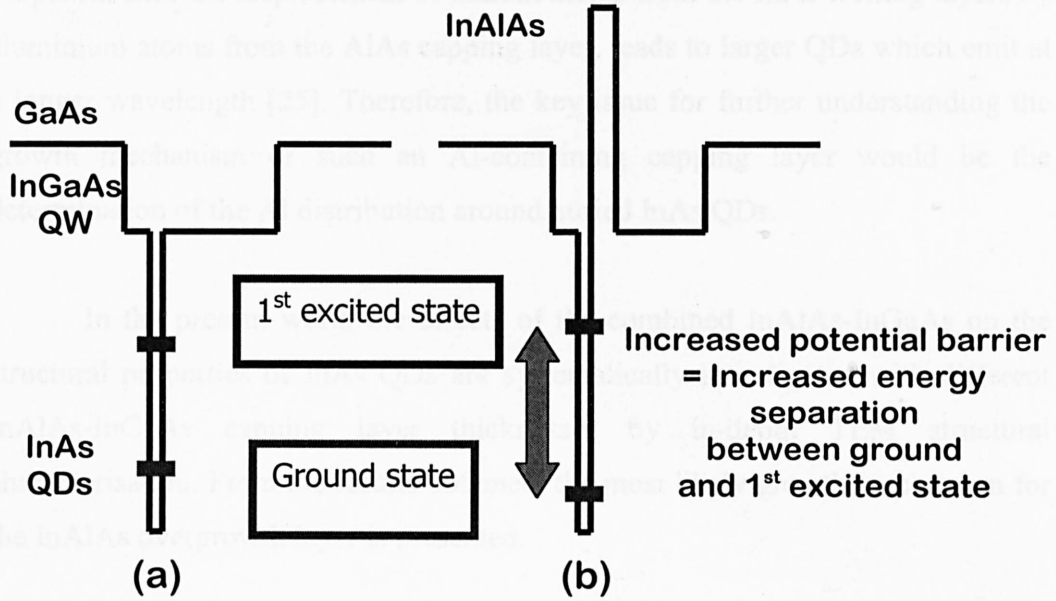

Fig. 4.2 The bandstructure of the QD active region with (a) InGaAs capping layer, compared with (b) combined InAlAs-InGaAs capping layer.

However, the precise origin of these optical improvements due to the Al-containing capping layer overgrowth process remains somewhat unclear. Likewise, the growth mechanism responsible for the increased or decreased emission wavelength after the deposition of the Al-containing capping layer is still uncertain since three competing models have previously been proposed. The

suppression of indium segregation and In-Ga intermixing at the interface between the QDs and overlaying Al-containing layers was initially proposed to account for the longer emission wavelength of InAs QDs with an AlAs capping layer [22]. However, the difference of the indium segregation between the InAs/AlAs and the InAs/GaAs interface is relatively small [23]. Following the use of atomic force microscopy (AFM), it has been suggested that the presence of aluminium atoms on top of the InAs QDs reduces the strain relaxation at the edges of the QDs, which prevents indium atom migration from the QDs [24]. As a consequence, a longer emission wavelength and stronger PL intensity was attributed to a better preservation of QD height and a higher QD density after capping with InAlAs [24]. An alternative explanation based on cross-sectional TEM images has been proposed: here the displacement of indium atoms from the InAs wetting layers by aluminium atoms from the AlAs capping layer, leads to larger QDs which emit at a longer wavelength [25]. Therefore, the key issue for further understanding the growth mechanism of such an Al-containing capping layer would be the determination of the Al distribution around buried InAs QDs.

In the present work, the effects of the combined InAlAs-InGaAs on the structural properties of InAs QDs are systematically investigated with different InAlAs-InGaAs capping layer thicknesses by in-depth TEM structural characterisation. From the results obtained, the most likely growth mechanism for the InAlAs overgrowth layer is presented.

4.2 Experimental procedure

The samples under investigation were grown on Si-doped GaAs (001) substrates in a VG Semicon V80H molecular beam epitaxy system. The schematic layer structure is as illustrated in Fig 4.3. 2 nm of $In_{0.2}Al_{0.8}As$ and 4 monolayers (MLs) of GaAs were employed as a SBL before 3.2-MLs of InAs were deposited with associated QD formation. The combined InAlAs-GaAs SBL was used, instead of a more conventional GaAs buffer layer or InGaAs

SBL was used, instead of a more conventional GaAs buffer layer or InGaAs SBL, to increase both the matrix and confinement potential of the buffer layer [26]. The capping layers deposited comprised x nm of $In_{0.2}Al_{0.8}As$ and (6 - x) nm of $In_{0.2}Ga_{0.8}As$, where x = 1.5, 3.0 and 6.0 nm. The growth temperature for the InAs QDs and the combined InAlAs-InGaAs capping layer was 510 °C. These layers were embedded between 150 nm of GaAs, grown at 580 °C, and were further confined by 100 nm $Al_{0.37}Ga_{0.63}As$ layers, grown at 610 °C. The surface evolution was monitored *in situ* by RHEED, where the formation of three-dimensional islands was indicated by the abrupt change from streaky RHEED pattern to a spotted one.

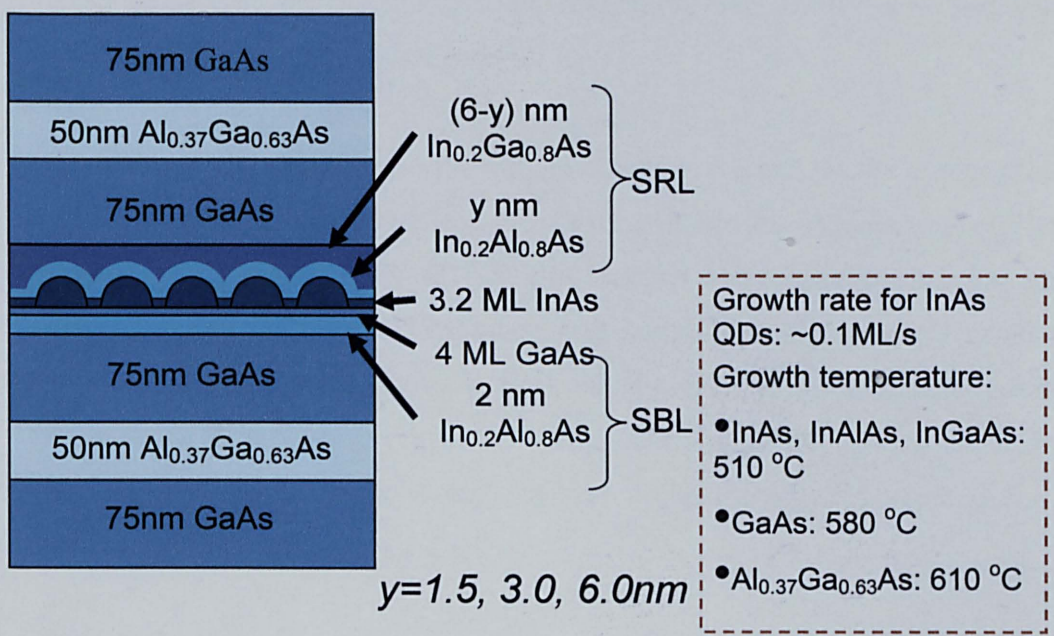

Fig. 4.3 Schematic diagram of the epitaxial layer of the QD structure

The cross-sectional TEM specimens, with [110] surface normal orientation, were thinned to electron transparency by conventional mechanical polishing and ion milling as described in Section 3.4 and 3.5. These specimens were examined using a JEOL 2010F field emission gun TEM/STEM operating at 200kV (Refer to Section 3.6).

Structural and compositional studies on cross-sectional QDs have typically been conducted using diffraction-contrast TEM [27-29] and HRTEM [30-32]. However, the accuracy and resolution of compositional analysis derived from conventional diffraction-contrast dark-field (200) TEM imaging can be limited due, for example, to the complex strain-induced lattice distortion in the vicinity of the QDs [33]. Likewise, approaches which attempt to extract local compositional information from HRTEM images can suffer from severe ambiguities, for example due to modification of the strain field by thin foil relaxation [34]. Besides that, thinned cross-sectional specimen foil can tilt and buckle locally during sample preparation [35]. Moreover, HRTEM images can only give a rough estimate of the shape and crystallography of the interfaces, even though they provide high lateral resolution, because the size and lattice strain of a QD are always correlated [36].

Hence, in order to provide a more conclusive result on the compositional analysis around InAs QDs and the effects of different $In_{0.2}Al_{0.8}As$ capping layer thickness on the QD size, HAADF-STEM analysis was conducted. It is generally known that the HAADF-STEM incoherent imaging is highly sensitive to the atomic number (Z). As the inelastic scattering power of an atom is proportional to the square of Z, atoms with higher Z will appear brighter [37, 38]. Furthermore, the EFTEM imaging technique has also been applied to qualitatively map the Al distribution in the vicinity of the QDs.

4.3 Results and discussion

4.3.1 HAADF-STEM results

Fig. 4.4 shows the low magnification HAADF-STEM image of the overall structure of InAs QDs, in this instance, with a 6 nm InAlAs overgrowth layer. The active region containing the QDs is clearly visible between two thick GaAs layers. Figs. 4.5 (a)-(c) show a series of high magnification HAADF-STEM

layers. Figs. 4.5 (a)-(c) show a series of high magnification HAADF-STEM images of InAs QDs with an $In_{0.2}Al_{0.8}As$ capping layer thickness of 1.5, 3.0 and 6.0 nm respectively. All images were obtained using the <011> zone axis alignment. In each case the InAs QDs are shown as the regions of brightest contrast. The $In_{0.2}Al_{0.8}As$ layers from the SBL and capping layer are shown as lines of darkest contrast sandwiching the InAs wetting layer and the GaAs layer from the SBL.

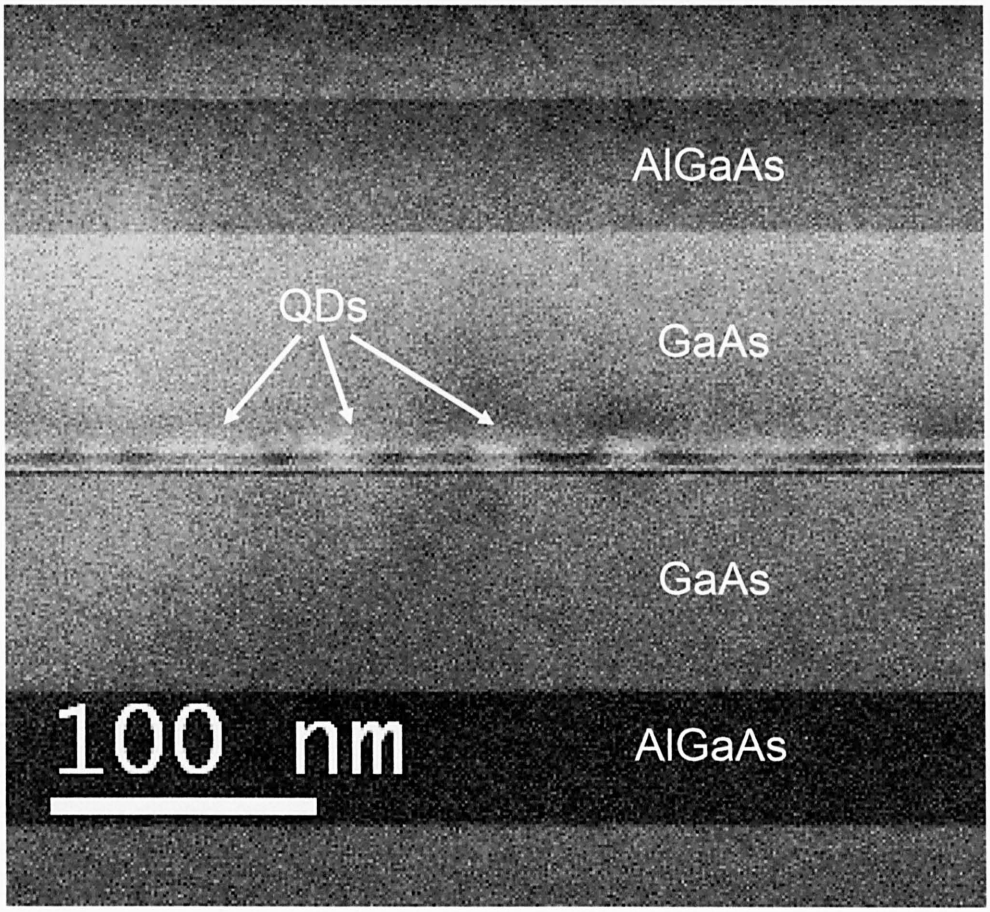

Fig. 4.4 Low magnification HAADF STEM image showing the epitaxial layers of the QD structure with 6 nm InAlAs capping layer. The growth direction is vertically upwards for the image.

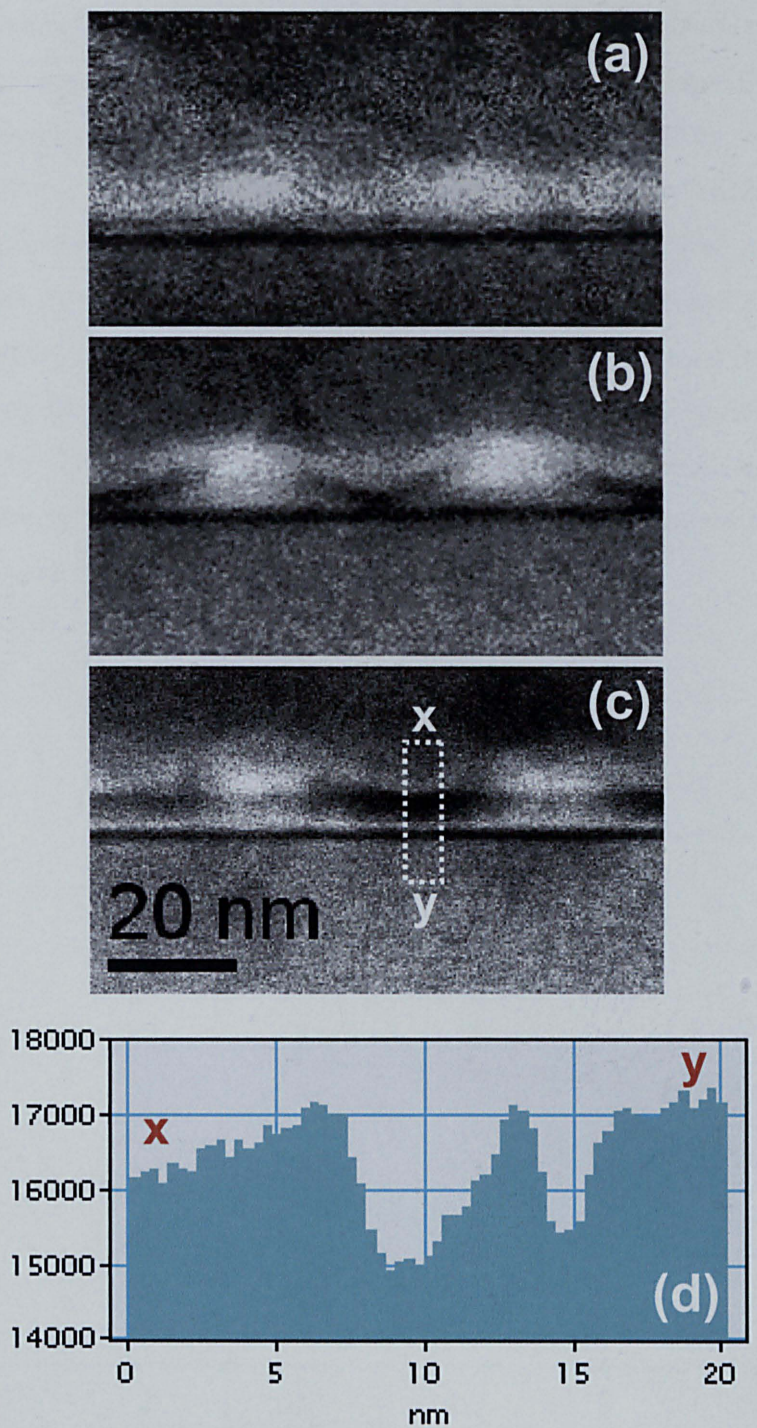

Fig. 4.5 Figs. 4.5 (a), (b) and (c) show high magnification HAADF STEM images of InAs QDs covered by 1.5, 3.0 and 6.0 nm InAlAs capping layer, respectively. Fig. 4.5(d) shows the brightness intensity profile of region x-y as shown in Fig. 4.5 (c).

A brightness profile labelled x-y shown in Fig. 4.5 (d) was obtained across the region adjacent to the embedded QD with a 6.0 nm InAlAs capping layer from Fig. 4.5 (c). Another notable observation is that the region of darker contrast above the wetting layer, which is attributed to the Al-rich region, was measured to be less than 5 nm, as opposed to the 6 nm of $In_{0.2}Al_{0.8}As$ deposit. This result suggests that there is significant elemental segregation in the InAlAs overgrowth layer where the aluminium adatoms have separated from the indium adatoms in the surface-strained InAlAs capping layer at the growth temperature of 510 °C. The regions of higher average atomic number, implied by the distinctly brighter contrast, above the region of darker contrast would indicate that profound indium segregation has occurred.

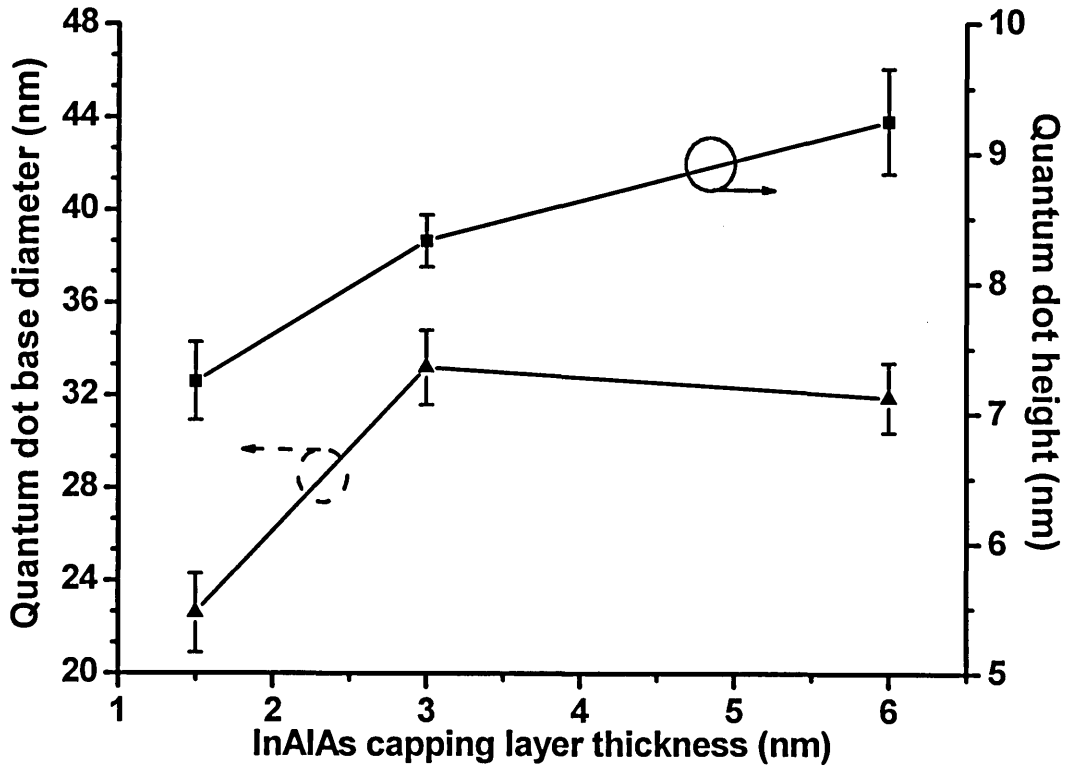

Fig. 4.6 Graph shows the average QD base diameter and height for different InAlAs capping layers, i.e. y = 1.5, 3.0 and 6.0 nm.

As shown in Fig. 4.6, the InAs QDs with 1.5, 3.0 and 6.0 nm $In_{0.2}Al_{0.8}As$ capping layer exhibited a lens cross-sectional shape, with an average base diameter of (22.6, 33.18, 31.85) nm and average height of (7.25, 8.33, 9.25) nm, respectively. Nonetheless, the contrast is not very distinct at the apex region of the QDs. This is probably due to the elemental intermixing between In, Ga (and possibly Al) atoms at the periphery of the QDs. The base diameter of the QDs has increased substantially with increasing thickness of the $In_{0.2}Al_{0.8}As$ capping layer from 1.5 to 3.0 nm, but decreased slightly when a 6 nm $In_{0.2}Al_{0.8}As$ capping layer was deposited. However, a subsequent increase of $In_{0.2}Al_{0.8}As$ capping layer thickness resulted in a corresponding significant increase in the height of QDs, in agreement with previous work on similar materials using atomic force microscopy (AFM) [21].

It has been previously reported that the increased volume of InAs QDs after the deposition of an InAlGaAs capping layer is attributed to the directional migration of indium adatoms from the InAs wetting layer to the QDs [25]. However, this would imply that capped QDs would be larger than uncapped ones. Using measurements from HRTEM images of uncapped QDs grown under the same conditions as the capped QDs, we have observed that the average height and base diameter, as shown in Fig 4.7, were ~10 nm and 33 nm, respectively, which clearly shows that the uncapped QDs are significantly larger than capped specimens [40].

Moreover, it has been stated that the better-preserved InAs QD height was due to aluminium accumulation on top of the InAs QD, which prevents the indium atoms from diffusing to the WL [21, 24]. The mechanism explains that the redshift of PL emission after the deposition of a thin AlAs capping layer on top of InAs QDs is due to reduced indium segregation and In-Ga intermixing between the QDs and capping layer [22]. However, the contrast modulation observed in the HAADF STEM images shown in Figs. 4.5 (a)-(c) suggests a significant reduction or absence of aluminium on top of the QDs. Nonetheless, HAADF STEM only shows the mean Z value of the layer. Due to the complex quaternary

structural composition, consisting of Al, In, Ga and As, it is difficult to give a definitive measure of aluminium concentration. Therefore, EFTEM elemental imaging was applied to map the aluminium distribution in the vicinity of the QDs.

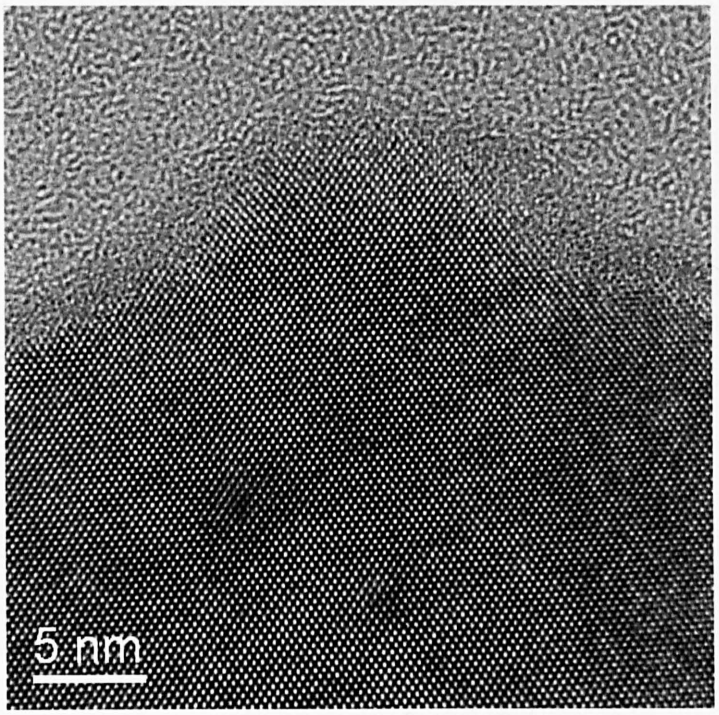

Fig. 4.7 High resolution TEM image of an uncapped InAs QD grown on the InAlAs-GaAs strained buffer layer.

4.3.2 EFTEM results

The EFTEM aluminium maps shown in Figs. 4.8 (a) & (b) were obtained using the aluminium $L_{2,3}$ edge at 73eV, with the specimen tilted (3 ± 1) degrees off the <110> zone axis to avoid electron channelling and to minimize diffraction contrast contributions. The three-window background subtraction method as described in Section 3.6.5 was employed to obtain an aluminium map around the QDs [39]. However, since the Al $L_{2,3}$ edge has a delayed peak, the post-edge image is taken at around 90eV. The zero loss peak of the EELS spectrum, also described in Section 3.6.5, is used to measure the sample thickness. In this work,

the specimen thicknesses were measured to be approximately 60 nm. In Figs. 4.8 (a) & (b), the locations of InAs QDs are indicated with circles, while the bright contrast in the EFTEM images indicates the presence of aluminium.

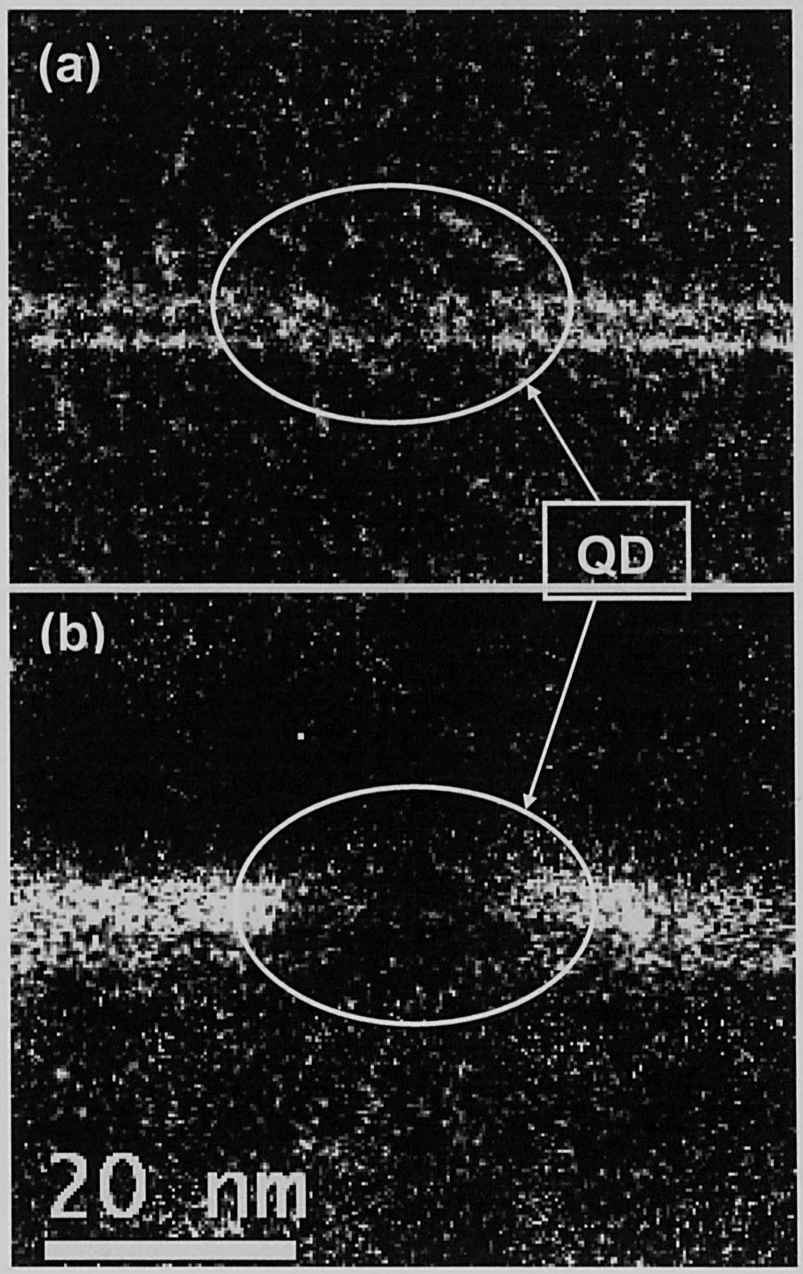

Fig. 4.8 The aluminium EFTEM maps show QDs with InAlAs/GaAs SBL and with (a) a 3.0 nm InAlAs + 3.0 nm InGaAs capping layer and (b) a 6.0 nm InAlAs capping layer.

In Fig. 4.8 (a) the Al signals deriving from the SBL and the capping layer are quite distinct and while the Al content within the lower SBL is relatively uniform the Al concentration above the region of the QD is reduced. On the other hand, the distinction between the Al signals deriving from the SBL and the capping layer is much less obvious in Fig. 4.8 (b). This is a likely consequence of the thicker Al-containing capping layer and the degree of specimen tilt away from the [110] zone axis, although one must also remember that the maximum spatial resolution of EFTEM imaging is limited to about 1 nm.

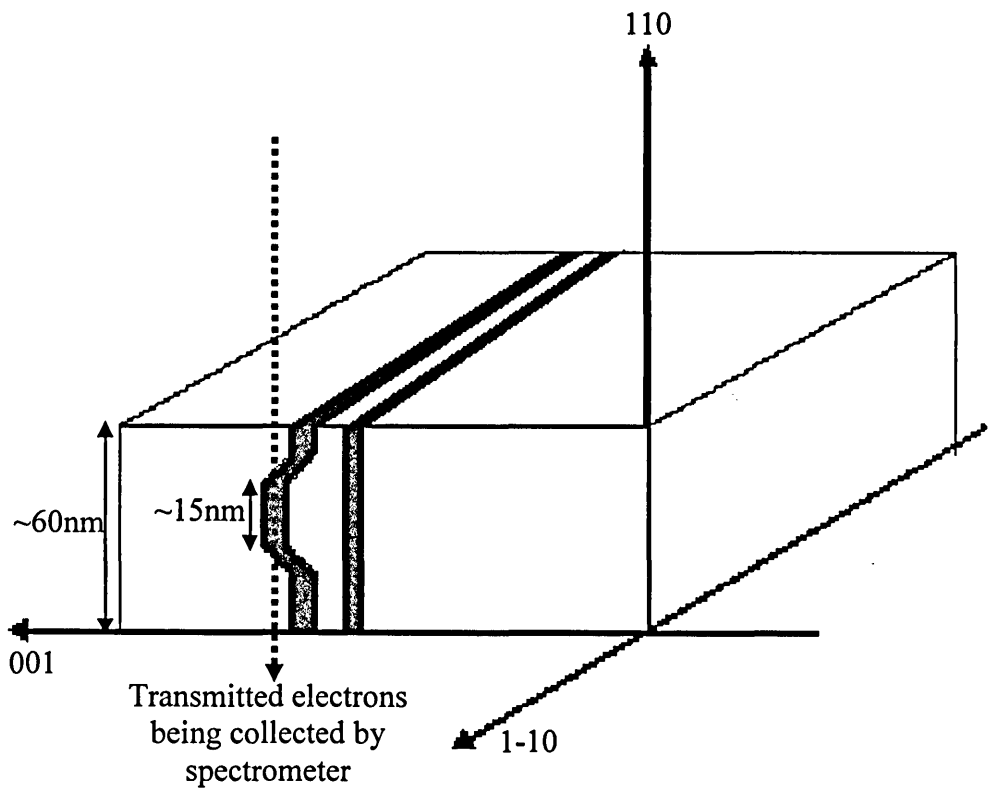

Fig. 4.9 Schematic diagram showing the trajectory of transmitted electrons, projecting through the TEM sample, before being collected by spectrometer.

At this point, we need to discuss the sensitivity of the EFTEM to detect Al atoms at the apex of the QDs, since the volume density of Al atoms on top of the QDs is clearly less than that in the InAlAs capping layer. Firstly, the shape

of the InAs QD is well understood to be a truncated pyramid [41]. Hence there is a finite thickness of material at the apex of the QD for the transmitted electrons to produce an Al signal, as shown in Fig. 4.9. Secondly, the EFTEM technique has a minimum detection limit of approximately 1% and the spatial resolution is around 1 nm [42]. Therefore, we believe that if Al is present above a QD, as suggested by some authors [21, 22, 24], then we should be able to detect an Al signal at the apex of a QD.

From Figs. 4.8 (a) and (b), what is apparent is a significant reduction in the Al signal on top of the InAs QDs, in particular in the case of the 6.0 nm InAlAs capping layer, with most of the aluminium apparently segregated laterally to the periphery of the QDs. Therefore, the notion of suppressed segregation or In-Ga intermixing does not explain the formation of larger QDs, since the Al-containing layer does not cover a significant fraction of the QD. Contrary to the work in Ref [21] which reported that Al adatoms are deemed immobile at the growth temperature of 510 °C, our results corroborate the findings of Xie *et al.* [43] which suggests that mobile surface Al adatoms migrate away from the apex of the InAs QDs. This can be understood through the presence of energetically unfavourable nucleation sites for aluminium adatoms at the facets of the apex of the elastically relaxed InAs islands as a result of the large differences in lattice constant between InAs and AlAs, as well as the effect of strain-driven migration [25, 43].

4.3.3 Surface chemical potential model

As an alternative to explain the QD height increase after an InAlAs capping layer was deposited, a model based on surface chemical potential was proposed. The surface chemical potential, first proposed by Srolovitz, is defined as the derivation of the free energy with respect to the number of atoms, where the change in energy associated with the addition of an atom to a stressed environment which depends on the magnitude and nature of the stress [44]. The

transport of materials away from the InAs QDs is caused by the gradient of the surface chemical potential, leading to directional migration of adatoms to the surface [43, 45, 46]. Ledentsov *et. al.* proposed that the surface chemical potential of In atoms can be described as [45, 46]:

$$\mu^{In}(r) = \mu_0^{In} + \gamma\Omega\kappa(r) + \Omega E_s(r) - \frac{\zeta\Omega\vartheta(r)}{\alpha} \qquad (4.1)$$

where μ_0^{In} is the chemical potential of In adatoms on the unstressed surface. The second term is the surface energy, where γ is the surface energy per unit area and $\kappa(r)$ is the surface curvature. The third term describes the contribution of the surface elastic energy, $E_s(r)$,where Ω is the atomic volume. The last term of Eq. (4.1) represents a modification of the chemical potential due to a wetting process, where ζ is the energy benefit resulting from the formation of a new wetting layer on the capping layer, α is the lattice parameter and $\vartheta(r)$=1 for a GaAs surface , $\vartheta(r)$=0 for an InAs surface, and 0< $\vartheta(r)$ <1 for either InGaAs or InAlAs capping layer.

It is well known that strain driven migration is the dominant factor resulting in the morphological evolution of the QD during the overgrowth process, generally resulting in a change in the lateral dimensions and a reduction in the height of the QD [45, 46]. Assuming that the surface curvature remains unchanged while the capping layer is deposited, the latter two terms of Eq. (4.1) dominate the effects of the capping layer on the chemical potential, as shown in Fig. 4.10. According to Ledentsov *et al.*, the deposition of a GaAs capping layer on the facets of elastically relaxed InAs QDs is energetically unfavourable, resulting in a directional migration of Ga adatoms away from the QDs and covers the InAs wetting layer [46]. As a result, the edges of InAs QDs become more compressed by the surrounding GaAs and increase the surface elastic energy [45]. The increase of surface elastic energy causes In atoms to detach from the QDs [45, 47]. The detached In adatoms then preferentially migrate towards the GaAs capping layer surface, where $\vartheta(r)$=1 and hence there is a lower

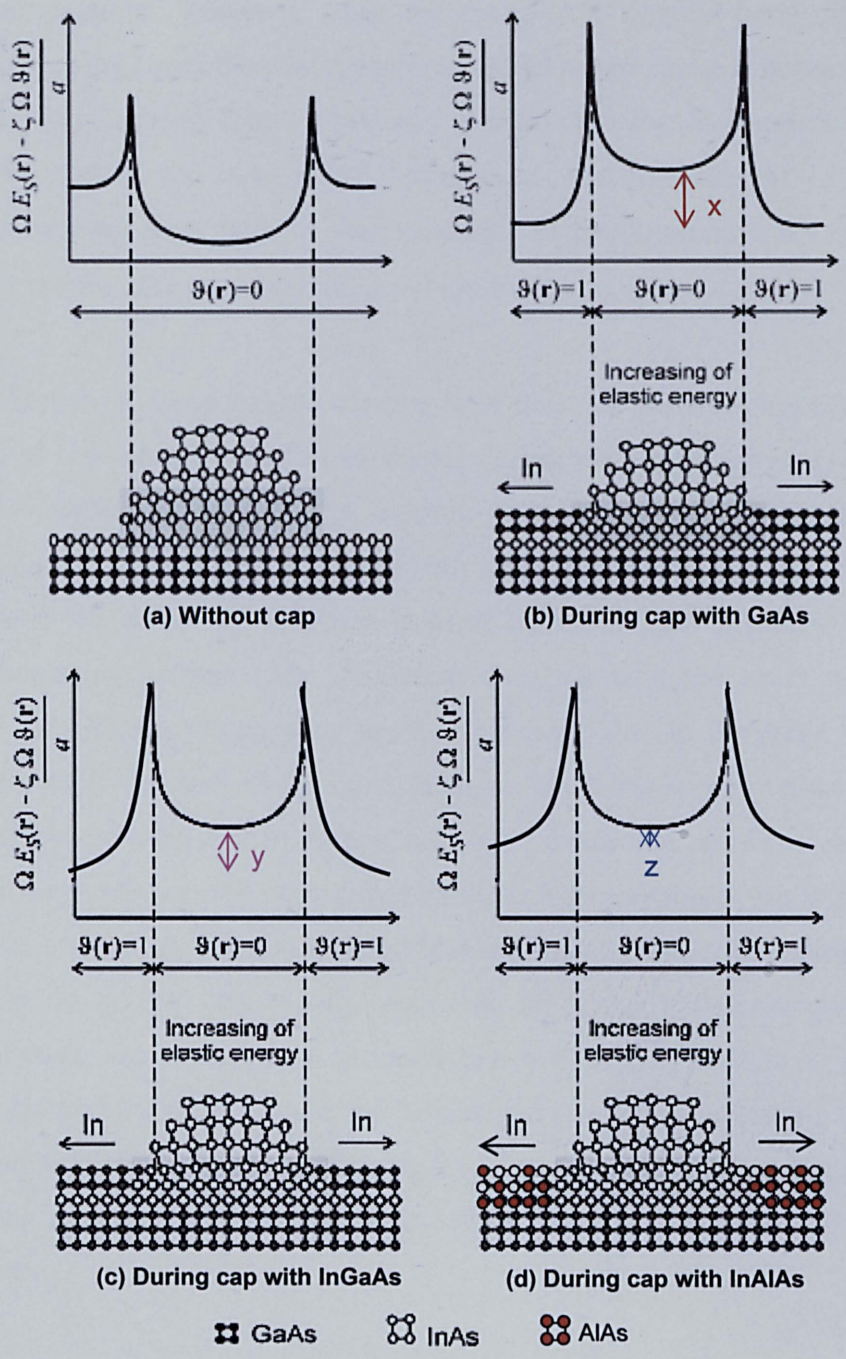

Fig. 4.10 Schematic diagrams of the term $\Omega E_s(r) - \frac{\zeta \Omega \vartheta(r)}{\alpha}$, modified from Ref [45], for (a) uncapped, (b) partially capped with GaAs, (c) partially capped with InGaAs and (d) partially capped with InAlAs, where the energy difference is x>y>z.

chemical potential. However, when the overgrowth layer is being replaced by InGaAs capping layer, the elastic energy induced by the lattice mismatch between the QD and capping layer is reduced, hence reducing the probability of In detachment from the InAs QDs. Furthermore, the high content of In in the InGaAs capping layer reduces the probability of In migration from the QDs as $\vartheta(r)<1$ reduces the chemical potential gradient.

However, for an InAlAs capping layer there are more indium atoms on the surface of the layer between InAs islands during the capping process compared with the surface of an InGaAs capping layer due to the enhanced indium segregation within the InAlAs overgrowth layer. Elemental aluminium is known to enhance the phase separation in strained $In_xAl_yGa_{1-x-y}As$ quantum wells [48, 49]. Replacing gallium with aluminium does not alter the strain distribution around the QD. However, poor In-Al intermixing due to the large difference between the In-As and Al-As bond energies could cause alloy clustering and composition modulation [50]. Hence, the higher concentration of indium adatoms on the overgrowth surface, contributed by the InAlAs capping layer, will decrease the surface chemical potential gradient between the QDs and the capping layer, as shown in Fig. 4.10(d) [40, 45, 46]. Moreover, the surface elastic energy is further reduced due to the lower lattice mismatch between the QDs and the capping layer surface layer. As a consequence, the detachment rate of indium atoms from InAs QDs and the subsequent migration to the capping layer surface is suppressed. Thus, the height of the QDs is more efficiently preserved during the InAlAs overgrowth.

4.3.4 PL results

The structural analysis of InAs QDs capped with an $In_{0.2}Al_{0.8}As$ capping layer implies that there are two significant, but opposing effects on optical properties. Firstly, we expect a redshift of the PL peak if the increased QD height is observed as a result of a reduced indium detachment rate for the InAs

QDs. Secondly, however, the lateral carrier-confining potential barrier of the InAs QDs, due to aluminium segregation to the periphery of the QDs, should decrease the wavelength of the PL peak. Room temperature PL analysis of QDs with identical growth structure, analysed by I. R. Sellers [18], is shown in Fig. 4.11. The wavelength of the InAs QD ground-state emission decreased slightly from 1.36-μm to 1.31-μm, whilst the PL intensity was increased by a factor of 450, as the thickness of $In_{0.2}Al_{0.8}As$ capping layer increased from 1.5 nm to 6.0 nm [26]. Therefore, a thicker $In_{0.2}Al_{0.8}As$ capping layer has increased the confinement of carriers in QDs and hence suppressed the thermal excitation of carriers from the InAs QDs, which would contribute to the greater room temperature PL efficiency.

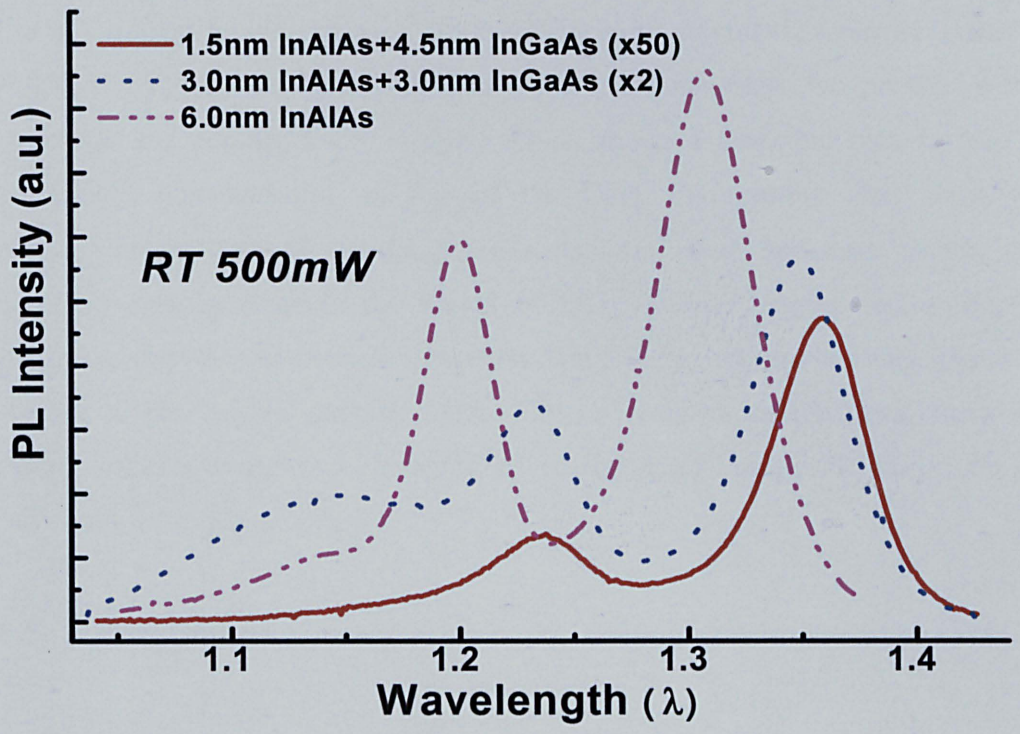

Fig. 4.11 Room temperature PL spectra for InAs QDs with x nm of $In_{0.2}Al_{0.8}As$ and (6 - x) nm of $In_{0.2}Ga_{0.8}As$, where x = 1.5, 3.0 and 6.0 nm, excited with a power density of 3kW/cm^2. (PL measurements obtained from Ref [17]]

From Fig. 4.11, the effect of increased lateral confinement potential appears to outweigh the effect of increased QD size in our structures, since the wavelength appears to be blue-shifted. Nonetheless, the effects of strain distribution and chemical composition both within the QDs and within the capping layer upon the emission wavelength may also be significant and require further investigation.

4.4 Conclusions

In conclusion, driven by advanced 1.3-μm laser applications, a structural study on the effects of InAlAs-InGaAs capping layer on InAs QDs has been carried out. The results clearly show the structural property differences between the InAlAs and InGaAs overgrowth that have been previously reported. Based on HAADF STEM imaging and EFTEM elemental mapping, we provide a new structural and compositional analysis which shows a profound reduction in the aluminium concentration on top of the QDs. Our results also show that subsequent increase of the $In_{0.2}Al_{0.8}As$ capping layer thickness results in a corresponding increase in the height of QDs. Indium segregation within the InAlAs overgrowth has been suggested to increase the indium atom density on the surface of the InAlAs capping layer. Thus, a reduced indium detachment rate during InAlAs overgrowth is proposed as the most likely mechanism for the increased InAs QD height.

4.5 References

[1] D. Bimberg, M. Grundmann, and N. N. Ledentsov, *Quantum Dot Heterostructures*, John Wiley and sons, Chichester, (1999), and references therein.

[2] A. G. Cullis, D. J. Norris, T. Walther, M. A. Migliorato, and M. Hopkinson, Phys. Rev. B, **66** (2002) 081305(R)

[3] A. G. Cullis, D. J. Norris, M. A. Migliorato, M. Hopkinson, Appl. Surf. Sci., **244** (2005) 65.

[4] D. L. Huffaker, G. Park, Z. Zou, O. B. Shckenkin and D. G. Deppe, IEEE J. Sel. Top. Quantum Electron., **6** (2000) 452.

[5] V. M. Ustinov and A. E. Zhukov, Semicond. Sci. Technol., **15** (2000) R41.

[6] H. Y. Liu, I. R. Sellers, T. J. Badcock, D. J. Mowbray, M. S. Skolnick, K. M. Groom, M. Gutierrez, M. Hopkinson, J. S. Ng, J. P. R. David, R. Beanland, Appl. Phys. Lett., **85** (2004) 704.

[7] H. Y. Liu, I. R. Sellers, M. Gutierrez, K. M. Groom, W. M. Soong, M. Hopkinson, J. P. R. David, R. Beanland, T. J. Badcock, D. J. Mowbray, M. S. Skolnick, J. Appl. Phys., **96** (2004) 1998.

[8] A. Ponchet, D. Lacombe, L. Durand, D. Alquier, and J.-M. Cardonna, Appl. Phys. Lett., **72** (1998) 2984.

[9] H. Y. Liu, M. Hopkinson, C. N. Harrison, M. J. Steer, R. Frith, I. R. Sellers, D. J. Mowbray, and M. S. Skolnick, J. Appl. Phys., **93** (2003) 2931.

[10] V. M. Ustinov, N. A. Maleev, A. E. Zhukov, A. R. Kovsh, A. Yu. Egorov, A. V. Lunev, B. V. Volovik, I. L. Krestnikov, Yu. G. Musikhin, N. A. Bert, P. S. Kop'ev, Zh. I. Alferov, N. N. Ledentsov, and D. Bimberg, Appl. Phys. Lett., **74** (1999) 2815.

[11] J. X. Chen, U. Oesterle, A. Fiore, R. P. Stanley, M. Ilegems, and T. Todaro, Appl. Phys. Lett., **79** (2001) 3681.

[12] G. Park, O. B. Shchekin, D. L. Huffaker and D. G. Deppe, IEEE Photonics Technol. Lett., **13** (2000) 230.

[13] K. Mukai, Y. Nakata, K. Otsubo, M. Sugawara, N. Yokohama and H. Ishikawa, Appl. Phys. Lett., **76** (2000) 3349.

[14] H. Y. Liu, M. Hopkinson, Appl. Phys. Lett., **82** (2003) 3644.

[15] O. B. Shchekin, J. Ahn, and D. G. Deppe, Electron. Lett., **38** (2002) 712.

[16] H. Y. Liu, M. Hopkinson, C. N. Harrison, M. J. Steer, R. Frith, I. R. Sellers, D. J. Mowbray, M. S. Skolnick, J. Appl. Phys., **93** (2003) 2931.

[17] H. Y. Liu, I. R. Sellers, M. Hopkinson, D. J. Mowbray and M. S. Skolnick, Appl. Phys. Lett., **83** (2003) 3716.

[18] I. R. Sellers, H. Y. Liu, M. Hopkinson, D. J. Mowbray and M. S. Skolnick, Appl. Phys. Lett., **83** (2003) 4710.

[19] R. Jia, D. S. Jiang, H. Y. Liu, Y. Q. Wei, B. Xu and Z. G. Wang, J. Cryst. Growth, **234** (2001) 354.

[20] Z. Y. Zhang, B. Xu, P. Jin, X. Q. Meng, Ch. M. Li, X. L. Ye, and Z. G. Wang, J. Appl. Phys., **92** (2002) 511.

[21] Y. Q. Wei, S. M. Wang, F. Ferdos, J. Vukusic, A. Larsson, Q. X. Zhao and M. Sadeghi, Appl. Phys. Lett., **81** (2002) 1621.

[22] M. Arzberger, U. Käsberger, G. Bőhm, and G. Abstreiter, Appl. Phys. Lett., **75** (1999) 3968.

[23] M. Schowalter, A. Rosenauer, D. Gerthsen, M. Arzberger, M. Bichler, and G. Abstreiter, Appl. Phys. Lett., **79** (2001) 4426.

[24] F. Ferdos, S. M. Wang, Y. Q. Wei, M. Sadeghi, Q. X. Zhao, A. Larsson, J. Cryst. Growth, **251** (2003) 145.

[25] A. F. Tsatsul'nikov, A. R. Kovsh, A. E. Zhukov, Yu. M. Shernyakov, Yu. G. Musikhin, V. M. Ustinov, N. A. Bert, P. S. Kop'ev, Zh. I. Alferov, A. M. Mintairov, J. L. Merz, N. N. Ledentsov, and D. Bimberg, J. Appl. Phys., **88** (2000) 6272.

[26] H. Y. Liu and M. Hopkinson, Appl. Phys. Lett., **82** (2003) 3644.

[27] R. Beanland, Ultramicroscopy, **102** (2005) 115.

[28] X. Z. Liao, J. Zou, D. J. H. Cockayne, and S. Matsumura, Ultramicroscopy, **98** (2004) 239.

[29] W. Neumann, H. Kirmse, I. Häusler, R. Otto and I. Hähnert, J. Alloy Compd., **382** (2004) 2.

[30] D. J. H. Cockayne, X. Z. Liao, and J. Zou, Inst. Phys. Conf. Ser. **169** "*Microscopy of Semiconducting Materials 2001*" edited by A. G. Cullis and J. L. Hutchison (IOP Publishing, Bristol and Philadelphia, 2001) p.77.

[31] V Grillo, L Lazzarini, and T Remmele, Mat Sci Eng B-Solid, **91** (2002) 264.

[32] M. Arlery, J. L. Rouvière, F. Widmann, B. Daudin, G. Feuillet, and H. Mariette, Appl. Phys. Lett., **74** (1999) 3287.

[33] P. Werner, K. Scheerschmidt, N. D. Zakharov, R. Hillebrand, M. Grundmann and R. Schneider, Cryst. Res. Technol., **35** (2000) 759.

[34] M. M. Treacy and J. M. Gibson, J. Vac. Sci. Technol. B, **4** (1986) 1458.

[35] T. Walther, C. B. Boothroyd, C. J. Humpreys, and A. G. Cullis, Proc. ICEM-13, **1** (1994) 365.

[36] P. Werner, K. Scheerschmidt, N. D. Zakharov, R. Hillebrand, M. Grundmann and R. Schneider, Cryst. Res. Technol., **35** (2000) 759.

[37] S. J. Pennycook, Ann. Rev. Mat. Sci., **22** (1992) 171.

[38] E. M. James, N. D. Browning, Ultramicroscopy, **78** (1999) 125.

[39] R. F. Egerton, *Electron Energy Loss Spectroscopy in the Electron Microscope*, Plenum, New York, (1996).

[40] H. Y. Liu, C. M. Tey, I. R. Sellers, T. J. Badcock, D. J. Mowbray, M. S. Skolnick, R. Beanland, M. Hopkinson, and A. G. Cullis, J. Appl. Phys., **98** (2005) 083516.

[41] D. M. Bruls, J. W. A. M. Vugs, P. M. Koenraad, H. W. M. Salemink, J. H. Wolter, M. Hopkinson, M. S. Skolnick, F. Long, S. P. A. Gill, Appl. Phys. Lett., **81** (2002) 1708.

[42] R. Brydson, *Electron Energy Loss Spectroscopy*, Bios, Oxford, (2001), p. 106.

[43] Q. H. Xie, P. Chen, and A. Madhukar, Appl. Phys. Lett., **65** (1994) 2051.

[44] D. J. Srolovitz, Acta Metall., **37** (1989) 621.

[45] R. Songmuang, S. Kiravittaya, and O. G. Schmidt, J. Cryst. Growth, **249** (2003) 416.

[46] N. N. Ledentsov, V. A. Shchukin, M. Grundmann, N. Kirstaedter, J. Böhrer, O. Schmidt, D. Bimberg, V. M. Ustinov, A. Yu. Egorov, A. E. Zhukov, P. S. Kop'ev, S. V. Zaitsev, N. Yu. Gordeev, Zh. I. Alferov, A. I.

Borovkov, A. O. Kosogov, S. S. Ruvimov, P. Werner, U. Gösele, and J. Heydenreich, Phys. Rev. B, **54** (1996) 8743.

[47] A. L. Barabasi, Appl. Phys. Lett., **70** (1997) 2565.

[48] M. V. Maximov, A. F. Tsatsul'nikov, B. V. Volovik, D. S. Sizov, Yu. M. Shernyakov, I. N. Kaiander, A. E. Zhukov, A. R. Kov, S. S. Mirkhirn, V. M. Ustinov, Zh. I. Alferov, R. Heitz, V. A. Shchukin, N. N. Ledentsov, D. Bimberg, Yu. G. Musikhin, and W. Neumann, Phys. Rev. B, **62** (2000) 16671.

[49] I. L. Krestnikov, A. V. Sakharov, N. N. Ledentsov, I. P. Soshnikov, Yu. G. Musikhin, A. R. Kovsh, V. M. Ustinov, I. V. Kochnikov, P. S. Kop'ev, Zh. I. Alferov, and D. Bimberg, in *Proceeding of the 6th International Symposium on Nanostructures: Physics and Technology*, St. Petersburg, Ioffe University (1998) p.257.

[50] E. Tournie, Y. H. Zhang, N. J. Pulsford, and K. Ploog, J. Appl. Phys., **70** (1991) 7362.

Chapter 5

Influence of growth temperature on near 1.55 μm GaInNAs/GaAs multiple quantum well

5.1 Introduction

It is clear that semiconductor lasers emitting at 1.3 μm and 1.55 μm wavelengths are important for optical fibre telecommunication networks due to their operation within the minimum loss and dispersion waveband window, as shown in Fig 4.1 [1]. Conventionally, the (In)GaAs(P)-InP materials system used for these applications has the disadvantages of high threshold current and relatively low characteristic temperature T_o due to poor carrier confinement [2]. Hence, a novel material, nitrogen containing GaAs-based III-V ternary and quaternary alloys, generically named GaInNAs (GINA), have been proposed to solve this problem [3, 4]. Furthermore, a GINA based long-wavelength VCSEL allows long wavelength GaAs/AlAs distributed Bragg reflectors to be used [5].

To date, several research groups have successfully demonstrated high performance 1.3 μm GINA/GaAs quantum well lasers using epitaxial growth techniques like MBE [6, 7] and MOVPE [8, 9]. At present however, there are numerous difficulties in obtaining good quality near 1.55 μm GINA materials and devices, which is further described in Section 2.7. Nitrogen incorporation in excess of 1 % has been shown to cause strong quenching of the PL intensity and a broadening of PL linewidth due to N-related defects [10, 11]. The crystal quality of GINA materials deteriorates drastically with increasing N, in order to reach the long wavelength range, due to the large miscibility gap which leads to phase separation [12-14]. Hence, the problem of phase separation in near 1.55 μm GINA QWs is partially suppressed by growing the GINA QWs at

a much lower growth temperature compared to the 1.3 μm [15-17]. Jaschke *et al.* has reported the optimization of growth temperature on the growth of 1.55 μm GINA QWs and their effects on lasers [15]. However, there are as yet no studies in detail yet investigating the growth mechanism and the basic physics understanding as to the effect of growth temperature upon the crystal quality of GINA.

In this present work, the effects of growth temperature on the structural properties of GINA QWs are systematically investigated by in-depth TEM and high resolution x-ray diffraction (XRD) analysis, while being compared with PL results. From the results obtained, the most likely growth mechanism based on growth temperature for the GINA QWs are presented.

5.2 Experimental procedure

The GINA MQW were grown on (001) on-axis GaAs substrates in a VG Semicon V80H molecular beam epitaxy system equipped with conventional Knudsen effusion cells for group-III, an EPI cracker source for As, and an Oxford Applied Research HD25 radio-frequency plasma source for nitrogen. The N composition was controlled by monitoring the intensity of the N plasma emission and calibrated using x-ray diffraction analysis of bulk materials, ie. GaAsN, grown under similar growth condition. The growth rate of the quaternary GINA wells and the (In)GaAs(N) barrier layers were 0.714 ML/s and 0.5 ML/s, respectively. The schematic layer structure is as illustrated in Fig 5.1. The optically active regions, i.e. three 8-nm $Ga_{0.6}In_{0.4}N_{0.03}As_{0.97}$ QWs embedded in between 52-nm $Ga_{0.97}In_{0.03}N_{0.01}As_{0.99}$ barrier layers are grown on GaAs substrate. The idea of using a (In)GaAs(N) quaternary barrier layer was conceived by Liu *et al.* to reduce the mole fraction of nitrogen in the MQW and hence improve its optical properties [18].

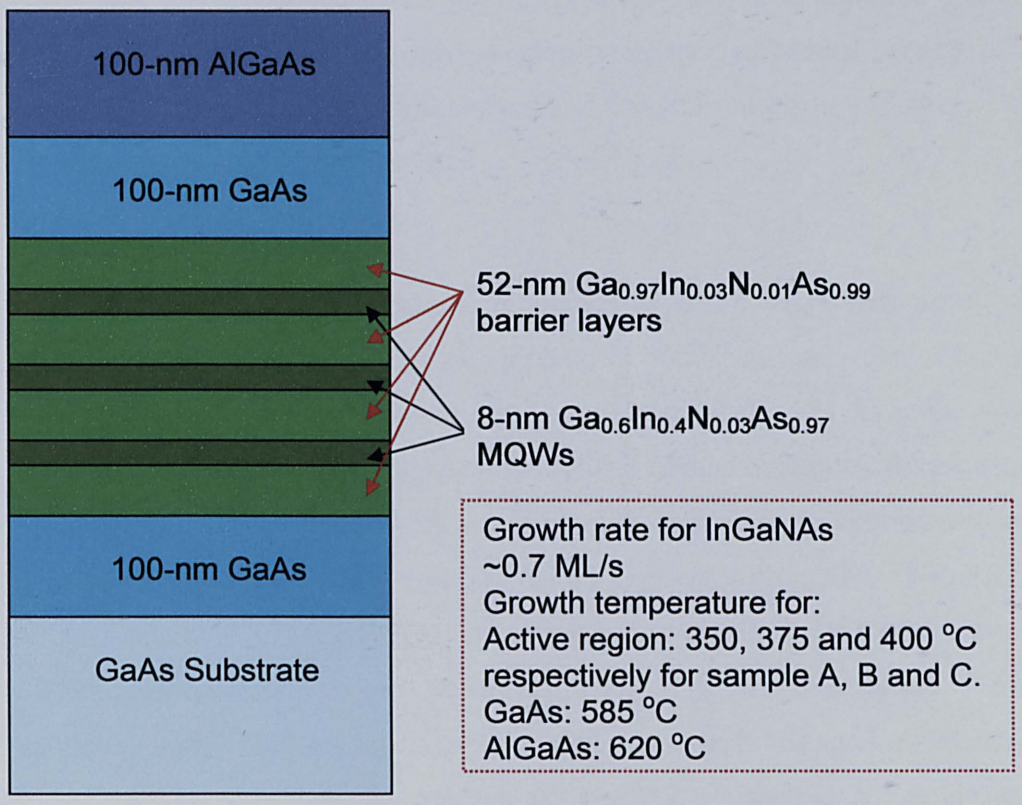

Fig. 5.1 Schematic diagram of the epitaxial layer of the GINA/GaAs MQW structure.

In order to avoid strain relaxation and its associated structural defects, three samples were prepared with the optically active regions grown at 350, 375, and 400 °C, respectively. The growth temperature on the substrate is very difficult to measure directly since there is a temperature difference between the thermocouple and the substrate. Infra-red detector measurements used by some researchers might be flawed due to interference from other heating elements in the MBE reactor. It is generally known that the oxide layer of the GaAs substrate desorbs from the flat surface (revealed with RHEED) when the substrate temperature reaches 580 °C. Hence, in order to achieve low temperature growth of 350 °C, for example, we can extrapolate the growth temperature from $\frac{T_o}{580^\circ C} = \frac{T^*}{350}$ where T_o is the thermocouple temperature when the oxide layer of the GaAs substrate

desorbs and T* is the thermocouple temperature needed to achieve growth temperature of 350 °C [19]. The active regions were then embedded between 200 nm GaAs layers, which were further confined by 100 nm AlGaAs layers. The III/V flux ratio is 1.6 for all N-containing layers.

In order to improve the optical properties of GINA MQW structures, all the samples were annealed *in situ* for one hour at 660 °C in the growth chamber with high As_2 background pressure after the growth of the top AlGaAs layer. The annealing process improves the structural and optical quality by the removal of defects and dislocations which act as non-radiative recombination centers [20]. The structural properties were studied by high-resolution XRD (HR-XRD) and cross-sectional TEM. HR-XRD measurements were carried out with a Bede QC200 high-resolution x-ray diffractometer. The cross-sectional TEM specimens, with [110] surface normal orientation, were thinned to electron transparency by conventional mechanical polishing followed by argon ion milling as described in Section 3.4 and 3.5. These specimens were examined using a JEOL 2010F field emission gun TEM operating at 200kV (Refer to Section 3.6). PL spectra were excited by an Ar^+ laser emitting at 532 nm and detected with a Ge detector.

5.3 Results and discussion

5.3.1 PL results

Three separate GINA/GaAs samples were grown under basically identical conditions, but at different growth temperatures of 350, 375, and 400 °C, respectively. Room temperature PL spectra are shown in Fig 5.2. The peak of RT PL emission is blueshifted slightly from 1.6-μm to 1.55-μm as the growth temperature decreases from 400 °C to 350 °C. This is probably due to the In-Ga interdiffusion effects at higher growth temperature at the interfaces of the

GINA/GaAs (mainly group-III atoms) i.e. indium atoms would diffuse into the GaAs barrier, which lowers the barrier bandgap. Besides that, the gallium atoms would diffuse into the GINA QWs, which increases the QW bandgap [21, 22]. The full width at half maximums (FWHM) of the PL spectra ranges from 50.2 meV for 350 °C to 56.4 meV for 400 °C respectively. More importantly, there is a substantial difference in the PL intensity between the samples with different growth temperatures. The strongest RT PL efficiency is obtained from the sample grown at 375 °C, which is about 4 times stronger than that of the sample grown at 350 °C and 60 times stronger than that of the sample grown at 400 °C. These indicate that the growth temperature window resulting in good optical efficiency of GaInNAs MQWs is much narrower than traditional InGaAs MQWs.

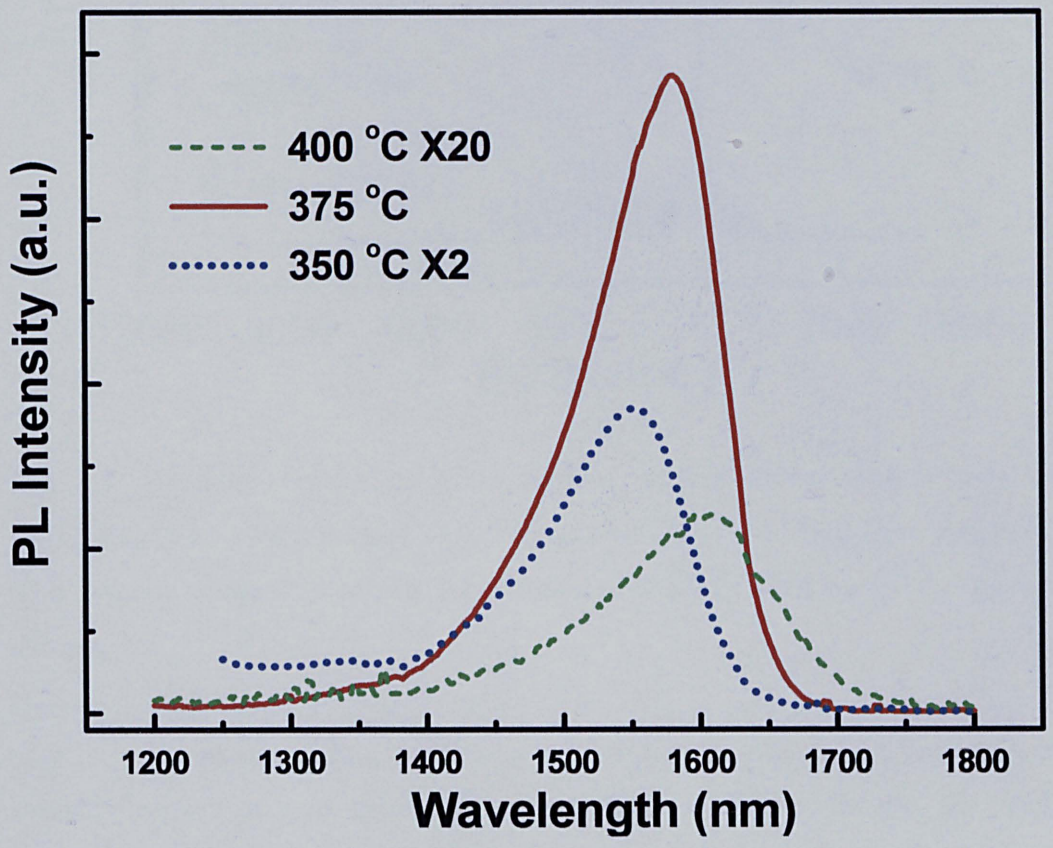

Fig. 5.2 Room-temperature PL spectra of GINA/GaAs MQWs grown at different temperatures of 350, 375 and 400 °C. (Modified from Ref [23].)

5.3.2 XRD results

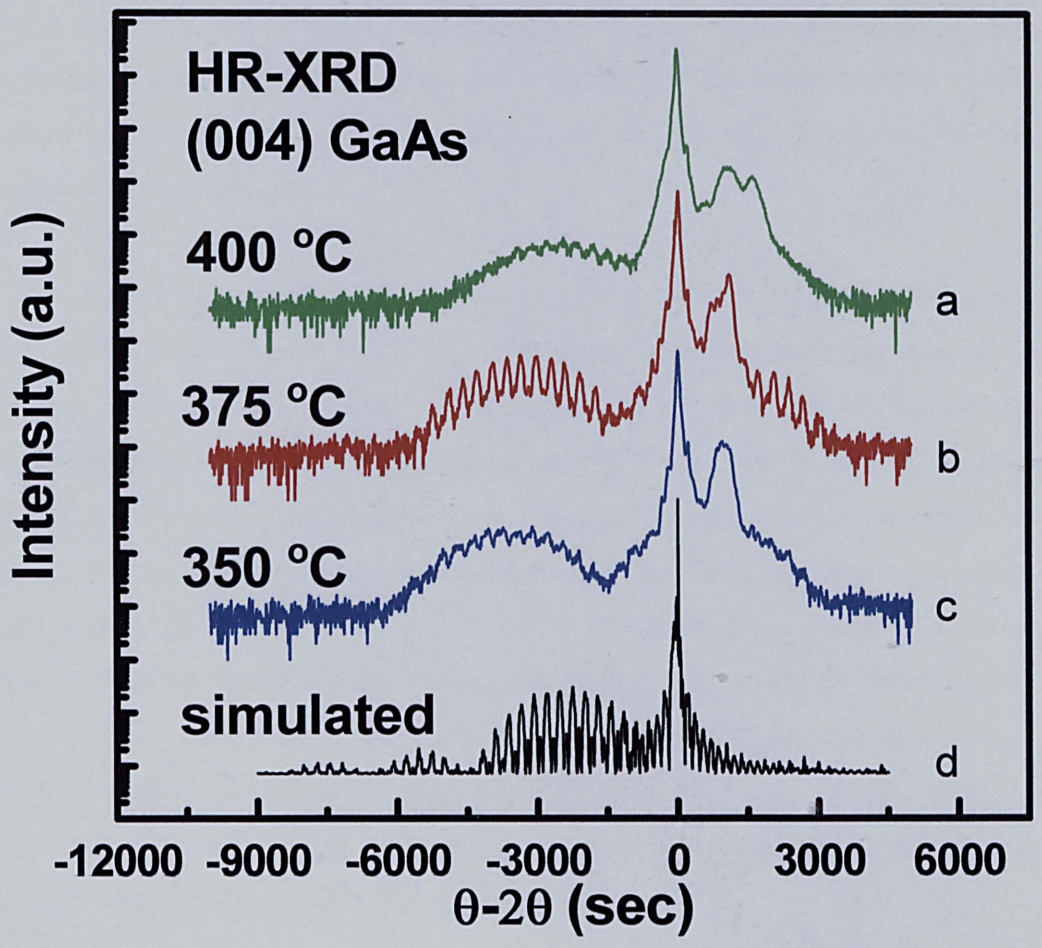

Fig. 5.3 High-resolution XRD rocking curves measurement (a-c) for GINA/GaAs MQWs grown at 350, 375 and 400 °C. (Modified from Ref [23].) The bottom curve (d) shows the simulated XRD according to the growth sample.

It is well established that the optical properties of the GINA materials are strongly related to their structural properties. [24, 25] Nonetheless, the origin and effect of the optical improvements due to the growth temperature remains unclear. In order to further understand the structural effect of growth temperature on the optical properties of GINA MQWs, HR-XRD measurements were performed to compare the structural characteristics of the three samples.

The (004) theta-2theta rocking curve profiles of these samples are shown in Fig. 5.3. The XRD simulated curve in Fig. 5.3 (d) is used as a comparison. The theta-2theta scan is performed by scanning the sample through the Bragg angle whilst simultaneously scanning the detector through twice the Bragg angle. The theta-2theta scan technique reduces the sensitivity of the rocking curve to tilts caused by mosaic spread while maintaining the sensitivity of the scan to stratified layer strain [26].

Compared with the sample grown at 350 °C and 400 °C, the satellite peaks from GINA MQW grown at 375 °C is much narrower and more pronounced in intensity, thus indicating better crystallinity. The degradations in the satellite peaks of GINA MQW for samples grown at 350 °C and 400 °C indicate that the crystal quality of the material is poor. This phenomenon could be related to several factors; such as compositional inhomogeneity, interface roughness, and/or high density of defects within GINA QWs. However, these factors cannot be distinguished by the XRD measurements alone and will be further discussed later with the TEM studies in the following section. Another notable observation is that as the growth temperature increases from 350 °C to 400 °C, the satellite peaks of the GINA MQWs shifted closer to the main peak. This phenomenon is attributed to strain relaxation in the GINA MQWs.

5.3.3 CTEM results

In order to further investigate the effects of growth temperature on the structural properties of GINA MQWs, TEM measurements were performed to study the interface quality and the compositional homogeneity of the GINA MQW for all three samples. Bright-field (g=200) TEM images for the samples grown at 350, 375, and 400 °C are shown in Fig. 5.4(a), (b), and (c), respectively. For the GINA MQW samples grown at 350 and 375 °C, the growth appears to be two-dimensional Frank-van der Merwe without any obvious surface

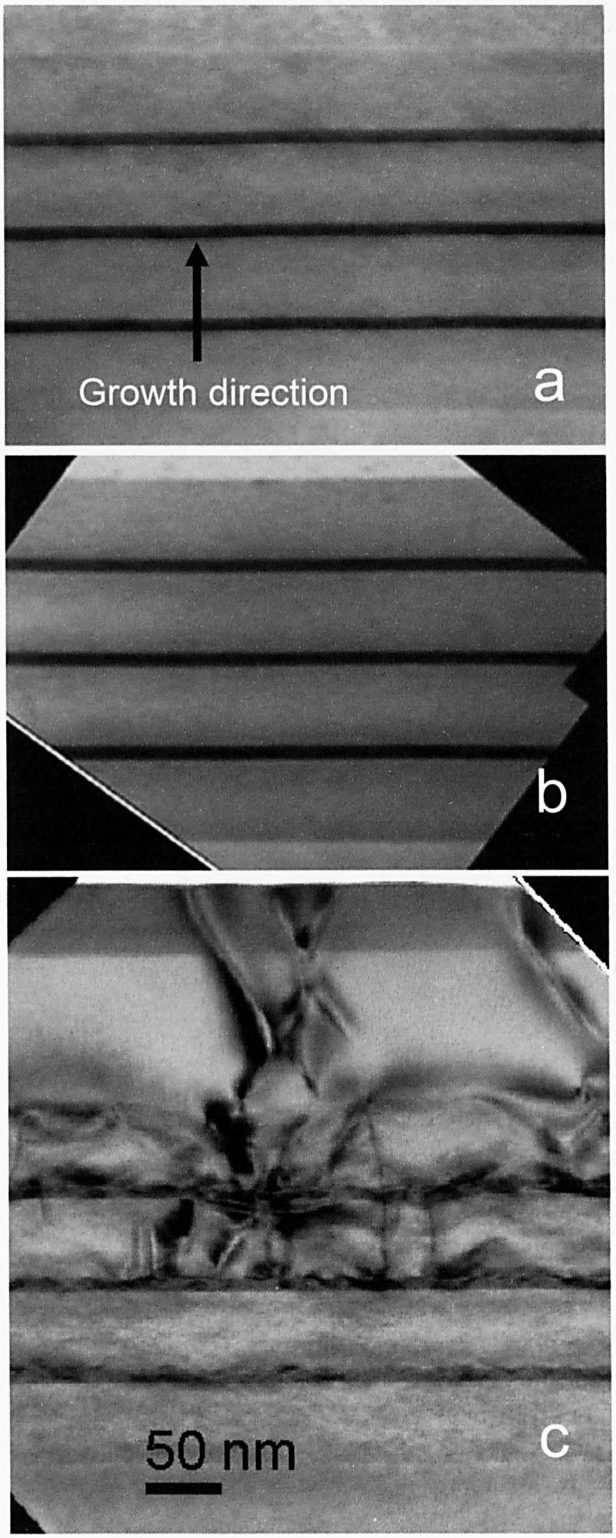

Fig. 5.4 Cross-sectional bright field TEM micrographs obtained with 002BF reflection of the GINA/GaAs MQWs grown at 350 (a), 375 (b), and 400 °C (c). All three images shares the same scale marker.

roughness or interdiffusion. However, the sample grown at 400 °C shows a significant increase of surface roughness in the first well similar to the three-dimensional or Stranski-Krastanow growth mode, as reported by Herrera *et al.* [27]. Further surface roughness was introduced within the second well which leads to more severe morphological instabilities in the third well. Threading dislocations are formed in the second and third QWs, and further extend towards the sample surface.

5.3.4 BF/HAADF STEM results

The compositional inhomogeneity and defects in QWs are further investigated by STEM. BF STEM images, shown in Fig 5.5 (a), were used to determine the density of dislocations. The threading dislocations found in the 400 °C sample have a non-uniform density of approximately 2.5 x 10^{15} cm^{-3}. The high magnification HAADF images for the samples grown at 350 and 375 °C are shown in Figs. 5.5 (b) and (c), respectively. These images are obtained using the <011> zone axis alignment. The GINA QWs are shown as bright regions in these images, with the GINA spacer and barrier layers appearing as dark bands.

There are no obvious compositional modulations observed in the HAADF images for the samples grown at 350 and 375 °C. This is clearly proven using the brightness profile for the HAADF STEM images, shown in Figs. 5.5 (d) and (e), which illustrates that the GINA/GaAs MQW interfaces are relatively symmetrical. These results indicate that the increase of growth temperature from 375 to 400 °C leads to compositional variation, surface roughness, and even the formation of dislocations. However, there is no notable structural difference between the conventional TEM and STEM images for samples grown at 350 and 375 °C, even though there are significant differences for the RT PL efficiency

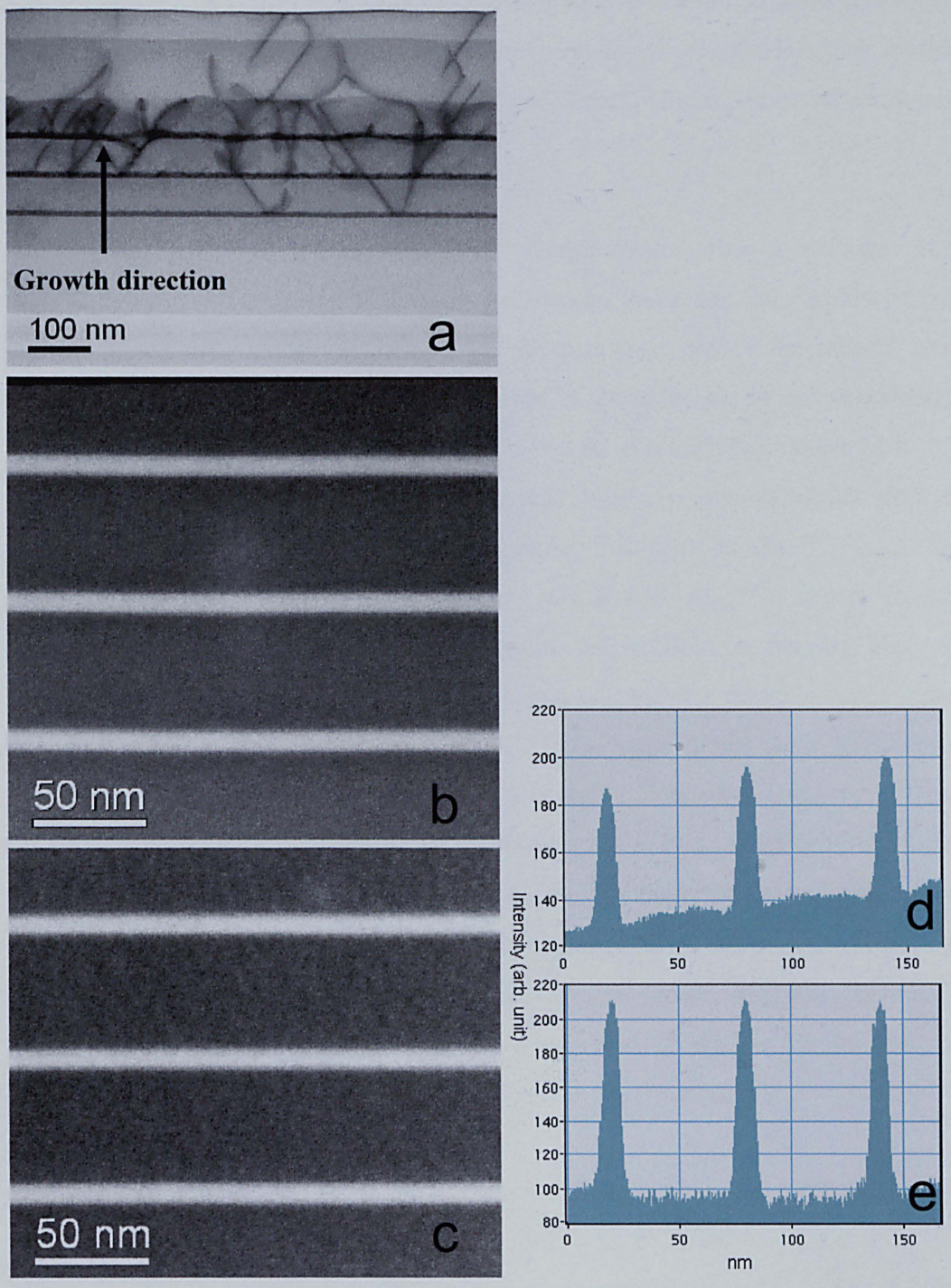

Fig. 5.5 Low magnification BF STEM showing the overall structure of GINA MQWs grown at 400 °C (a). Figs. 5.5 (b) and (c) show high magnification HAADF STEM images GINA MQWs grown at 350 and 375 °C respectively. Fig. 5.5 (d) and (e) shows the brightness intensity profile of Figs. 5.5 (b) and (c) respectively.

and wavelength in Fig. 5.2 and the structural properties obtained from HR-XRD measurements (see Fig. 5.3). But weak contrast modulation in the HAADF image of the sample grown at 400 °C indicates small compositional fluctuations along the QWs.

Indeed, while in ternary alloys the compositional ratio x indicates the number of bonds of each type, i.e. the ratio between In-As and Ga-As pairs in the $In_xGa_{1-x}As$ material system is x:(1-x), but in quaternary alloys the ratio is less certain [28]. For $In_xGa_{1-x}As_{1-y}N_y$, the number of In-As bonds is not necessarily $x*(1-y)*M$ nor is the number of Ga-N bonds equals to $(1-x)*y*M$, where M is the total number of bonds. Furthermore, it is not known if the equimolar system $Ga_{0.5}In_{0.5}As_{0.5}N_{0.5}$ is to be thought of as Ga-As + In-N or as Ga-N + In-As or alternatively, equal share of Ga-As + In-N + Ga-N + In-As [29]. Therefore, the ratio of the nearest-neighbour bond configuration in GINA quaternary alloy is very ambiguous. However, it is generally known that the development of the nearest-neighbour bond configuration in GINA quaternary alloy is largely determined by the competition between local strain and cohesive bond energy [29, 30]. The local strain is determined by the differences of bond lengths between the corresponding bond configurations. During the epitaxial growth process, the configuration of nearest-neighbour bonds is adjudged to be driven by maximizing the cohesive bond energy instead of minimizing the strain [31]. This is mainly because at the growth surface, the adatoms can relax freely, hence the nearest-neighbour bond configuration is unaffected by the local strain.

The cohesive energies of the various bond configurations for Ga-N, In-N, Ga-As, and In-As are 2.24, 1.93, 1.63, and 1.55 eV/bond, respectively [32]. Consequently, the preferred configuration, in terms of bond energy, is Ga-N + In-As during growth. However, since Ga and N are smaller atoms than In and As, the Ga-N + In-As bond configuration will cause higher epitaxial strain energy in comparison with the Ga-As + In-N configuration [29, 30]. Hence, the resulting elastic strain energy accumulated during growth causes compositional modulation and surface roughness (two-dimensional to three-dimensional growth transition,

see Section 2.10.2), and even dislocation formation when the accumulated strain is over the critical value. The schematic diagram of the strained lattice-mismatched heterostructure and a relaxed lattice-mismatched heterostructure is as shown in Fig. 5.6. To reduce the possibility of generation of the bond-energy-preferred Ga-N + In-As configuration during growth, it is necessary to decrease the growth temperature to reduce the adatom mobility. Thus, in comparison with the sample grown at 400 °C, the compositional modulation and surface roughness will be profoundly reduced and the formation of dislocations will be suppressed for the samples grown at lower temperatures of 350 and 375 °C.

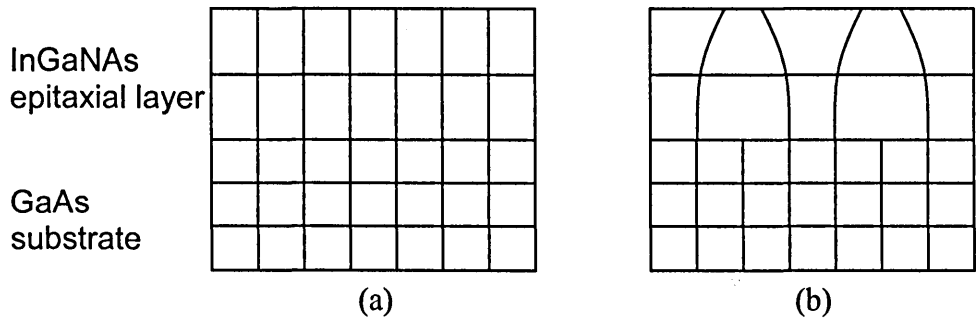

Fig. 5.6 (a) Pseudomorphic strained lattice-mismatched epitaxial layer. (b) Relaxed lattice mismatched epitaxial layer with misfit dislocations introduced.

5.3.5 HRTEM results

In order to further investigate the structural property differences for the samples grown at 350 °C and 375 °C, high-resolution TEM measurements have been performed. The images of the bottom QW for the both samples grown at 350 °C and 375 °C are shown in Figs. 5.7 (a) and (b), respectively. Compared with the sample grown at 375 °C, there are stronger contrast modulations observed within the QW for the sample grown 350 °C, where local regions appear almost amorphous. As the sample is grown at a temperature as low as 350 °C, we tentatively attribute these contrast modulations in Fig. 5.7 (b) to the agglomeration of point defects resulting from the excess As. Although zero dimensional point

defects are generally not visible in TEM images, the strain effects around nanoscale chemical zones, such as clusters of atoms or vacancies, can be imaged and understood semi-quantitatively [33].

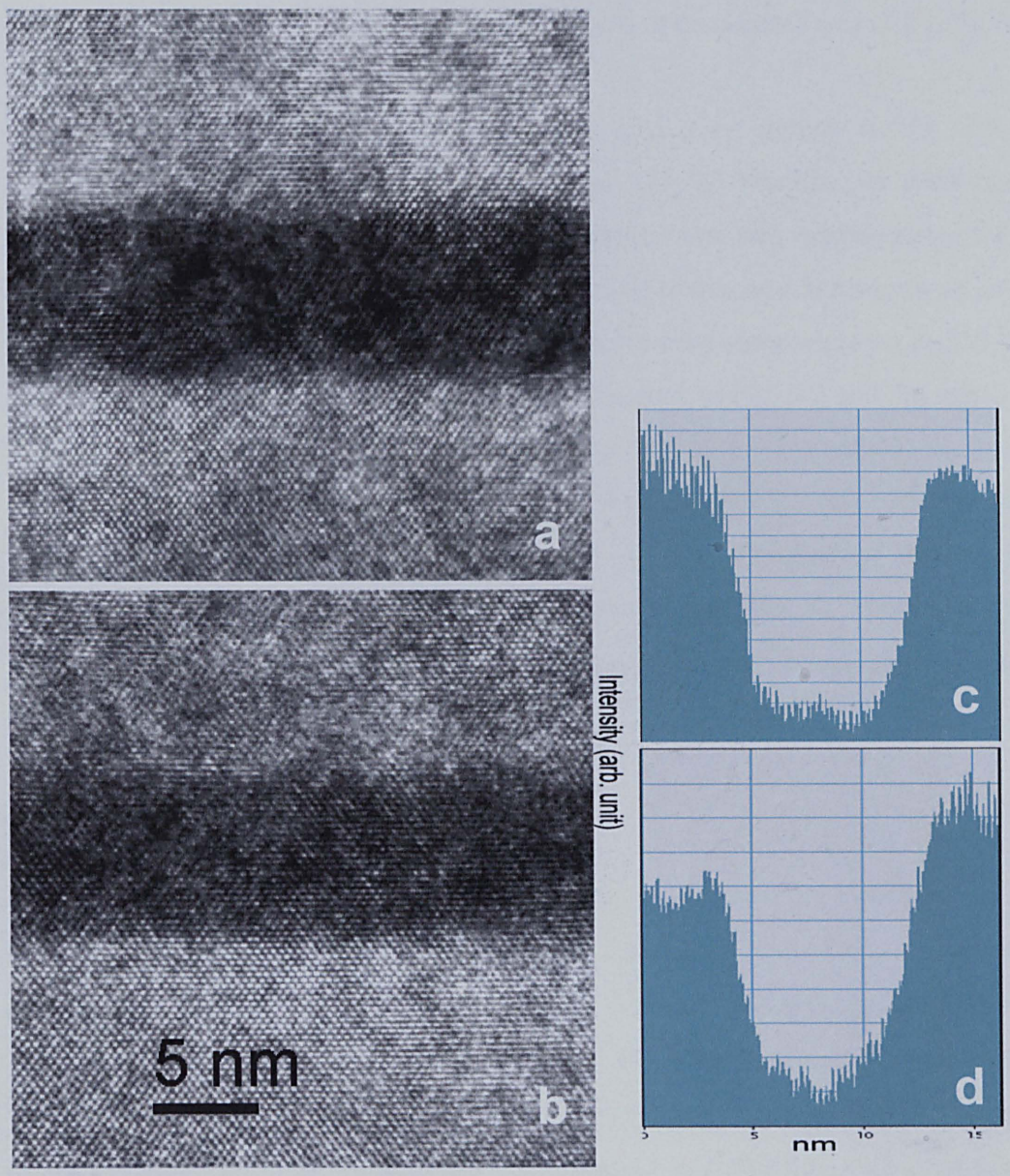

Fig. 5.6 High-resolution cross-sectional TEM images of the bottom QW for the samples grown at 350 (a) and 375 °C (b) along with their associated brightness profile (c) and (d), respectively.

It is well known that the relative desorption rates of As_2 dimers and As_4 tetramers for an incident As_2 flux will be reduced with temperature in the growth temperature range of these samples. Hence, the desorption rate of As_4 molecules will be decreased acutely when the temperature falls to the low-temperature region of 350 °C or below [34]. The excess As could cause several types of point defects, such as antisite defects, interstitial defects, and gallium vacancies [35].

Therefore, there will be a higher density of point defects in the GINA MQWs grown at 350 °C than those grown at 375 °C, resulting in a stronger contrast modulation in the HRTEM images. Similar contrast modulations of the GINA QWs have been observed in TEM images of low-temperature-grown GaAs layers [36, 37]. A higher density of point defects in the sample grown at 350 °C could also well explain the degraded RT PL efficiency in Fig. 5.2 and the reduced satellite peak intensity in Fig. 5.3 for this sample. Figs. 5.6 (c) and (d) illustrate the brightness profile of the samples grown at 350 and 375 °C, respectively. The brightness profiles clearly showed that the GINA/GaAs interfaces of the sample grown at 350 °C are more abrupt as compared to the 375 °C sample, which exhibits a more gradual slope. This reaffirms that higher temperature growth increases elemental intermixing.

5.4 Conclusions

In conclusion, driven by the need to investigate the effects of growth temperature, optical and structural studies on 1.6-μm GINA/GaAs MQWs has been carried out. A significantly stronger RT PL efficiency has been obtained from the sample grown at 375 °C, as compared to the samples grown at 350 and 400 °C. Meanwhile, the peak of RT PL emission is redshifted with increasing temperature due to In-Ga interdiffusion.

From the CTEM and STEM images, composition modulations, interface roughness, and even threading dislocations have been observed in the sample

grown at 400 °C. This could be understood by the development of the preferred Ga-N and In-As bond configuration on the growing surface at this growth temperature. For the sample grown at 350 °C, the relatively strong contrast modulation within GINA QW has been observed in high-resolution TEM images. We tentatively attribute these contrast modulations to the agglomeration of point defects due to excess As in GINA QWs. These results indicate that the growth temperature is critical to obtain high-quality 1.55-μm GINA MQWs, and hence high-performance from GaInNAs/GaAs MQW devices.

5.5 References

[1] J. S. Harris Jr., Semicon. Sci. Tech., **17** (2002) 880.

[2] H. Temkin, D. Coblentz, R. A. Logan, J. P. Van der Ziel, T. Tanbun-Ek, R. D. Yadvish, and A. M. Sergent, Appl. Phys. Lett., **62** (1993) 2402.

[3] M. Kondow, K. Uomi, A. Niwa, T. Kitatani, S. Watahiki, and Y. Yazawa, Proc. 1995 Solid State Device and Mat., Osaka, Japan (1995) 1016.

[4] M. Kondow, K. Uomi, A. Niwa, T. Kitatani, S. Watahiki, and Y. Yazawa, Jpn. J. Appl. Phys., **35** (1996) 1273.

[5] T. Miyamoto, T. Takada, K. Takeuchi, F. Koyama, and K. Iga, Quantum Opt., **9** (1997) 126.

[6] J. O. Mitomo, M. Yokozeki, Y. Sato, Y. Hirano, T. Hino, and H. Narui, IEEE J. Sel. Top. Quant. El., **11** (2005) 1099.

[7] K. S. Kim, S. J. Lim, K. H. Kim, J. R. Yoo, T. Kim, Y. J. Park, J. Cryst. Growth, **273** (2005) 368.

[8] S. M. Wang, Y. Q. Wei, X. D. Wang, Q. Zhao, M. Sadeghi, and A. Larsson, J. Cryst. Growth, **278** (2005) 734.

[9] H. Riechert, A. Ramakrishnan, and G. Steinle, Semicond. Sci. Tech., **17** (2002) 892.

[10] H. P. Xin and C. W. Tu, Appl. Phys. Lett., **72** (1998) 2442.

[11] S. G. Spruytte, C. W. Coldren, J. S. Harris, W. Wampler, P. Krispin, K. Ploog, and M. C. Larson, J. Appl. Phys., **89** (2001) 4401.

[12] I. A. Buyanova, W. M. Chen, G. Pozina, J. P. Bergman, B. Monemar, H. P. Xin, and C. W. Tu, Appl. Phys. Lett., **75** (1999) 501.

[13] Z. Pan, L. H. Li, W. Zhang, Y. W. Lin, and R. H. Wu, Appl. Phys. Lett., **77** (2000) 1280.

[14] S. R. Bank, H. B. Yuen, M. A. Wistey, V. Lordi, H. P. Bae, and J. S. Harris, Jr. Appl. Phys. Lett., **87** (2005) 021908.

[15] G. Jaschke, R. Averbeck, L. Geelhaar, and H. Riechert, J. Cryst. Growth, **278** (2005) 224.

[16] M. Gutierrez, J. S. Ng, and J. P. R. David, Appl. Phys. Lett., **83** (2003) 4951.

[17] M. Herrera, D. Gonzalez, M. Hopkinson, P. Navaretti, M. Gutierrez, H. Y. Liu, and R. Garcia, Semicond. Sci. Technol., **19** (2004) 813.

[18] H. Y. Liu, M. Hopkinson, P. Navaretti, M. Gutierrez, J. S. Ng, and J. P. R. David, Appl. Phys. Lett., **83** (2003) 4951.

[19] H. Y. Liu, *private communication.*

[20] Z. Pan, L. H. Li, W. Zhang, Y. W. Lin, and R. H. Wu, Appl. Phys. Lett., **77** (2000) 1280.

[21] M. C. Y. Chan, C. Surya, P. K. A. Wai, J. Appl. Phys., **90** (2001) 179.

[22] T. Kitatani, K. Nakahara, M. Kondow, and C. W. Tu, J. Cryst. Growth, **202** (2000) 345.

[23] H. Y. Liu, C. M. Tey, C. Y. Jin, S. L. Liew, P. Navaretti, M. Hopkinson, A. G. Cullis, Appl. Phys. Lett., 88 (2006) 191907.

[24] C. S. Peng, E.-M. Pavelescu, T. Jouhti, J. Konttinen, I. M. Fodchuk, Y. Kyslovsky, and M. Pessa, Appl. Phys. Lett., **80**, 4720 (2002).

[25] J.-M. Chauveau, A. Trampert, K. H. Ploog, M.-A. Pinault, and E. Tournie, Appl. Phys. Lett., **82**, 3451 (2003).

[26] R. J. Lynch, Thesis (Ph.D.), University of Sheffield, Department of Electronic and Electrical Engineering (2005) 47.

[27] M. Herrera, D. Gonzalez, M. Hopkinson, P. Vavaretti, M. Gutierrez, H. Y. Liu, and R. Garcia, Semicond. Sci. Technol., **19** (2004) 813.

[28] M. Ichimura and A. Sasaki, Phys. Rev. B, **36** (1987) 9694.

[29] K. Kim and A. Zunger, Phys. Rev. Lett., **86**, 2609 (2001).

[30] X. Kong, A. Trampert, E. Tournie, and K. H. Ploog, Appl. Phys. Lett., **87** (2005) 171901.

[31] T. Matsuoka, T. Sasaki, A. Katsui, Optoelectron. Devices Technol., **5** (1990) 53.

[32] W. A. Harrison, *Electronic Structure and the Properties of Solids*, Dover, New York, (1989), pp. 175-176.

[33] B. Fultz and J. Howe, *Transmission Electron Microscopy and Diffractometry of Materials*, Second Edition, Springer, New York, (2002), p. 340.

[34] B. A. Joyce, Rep. Prog. Phys., **48** (1985) 1637.

[35] X. Liu, A. Prasad, J. Nishio, E. R. Weber, Z. Liliental-Weber, and W. Walukiewicz, Appl. Phys. Lett., **67** (1995) 279.

[36] N. A. Bert, A. A. Suvorova, V. V. Chaldyshev, Yu. G. Musikhin, V. V. Preobrazhenski, M. A. Putyato, B. R. Semyagin, and R. Werner, Semiconductor, **32** (1998) 683.

[37] I. S. Gregory, C. M. Tey, A. G. Cullis, M. J. Evans, H. E. Beere, and I. Farrer, Phys. Rev. B., **73** (2006) 1.

Chapter 6

Two-trap model for precipitate formation in partially-annealed low-temperature-grown GaAs

6.1 Introduction

The growth of low-temperature-grown GaAs by MBE has been extensively carried out to study both the physics and potential optoelectronic device applications, owing to its unique combination of physical properties [1-5]. MBE grown GaAs, which is normally formed at around 600 °C, is grown at low temperature (190-350 °C) in order to incorporate a high concentrations of excess As (up to 1.5 %) which leads to an increase of the lattice parameter (up to 0.15 %) [6]. Low temperature growth of GaAs suppresses the out-diffusion of arsenic, allowing an excess to be incorporated. The excess arsenic may be manifested as three distinct types of point defects: arsenic antisites (As_{Ga}), arsenic interstitial (As_i) and gallium vacancies (V_{Ga}) [7].

In as-grown (i.e. unannealed) LT-GaAs, the electron trapping lifetime may be as short as 90 fs [8], due to the rapid trapping of carriers by intermediate energy levels (traps) introduced by point defects [9]. However, the need of a high unilluminated bulk resistivity is very important for photoconductive applications (e.g. terahertz photodetector). As-grown LT-GaAs material tends to have a low resistivity (<10 Ωcm) due to the hopping conduction between the mid-gap trapping states introduced by point defects [10]. Nonetheless, the saturation of defect states is problematic since each carrier captured from the conduction band neutralizes a trap. This occurs because the electron-hole recombination rate maybe several orders of magnitude slower than the trapping time [11].

The low resistivity problem is typically overcome by annealing the LT-GaAs material at high temperatures, creating precipitates from the migrating point defects. The elemental arsenic precipitates act as buried Schottky barriers with spherical depletion regions [12]. The material becomes "semi-insulating" when the arsenic precipitate number density is high enough to allow the overlapping of depletion regions [12, 13]. Furthermore, the saturation effects may be compensated by the relatively high density of states in the precipitates. Typically, annealing is performed at around 600 °C for between 10 to 15 mins, resulting in almost total removal of point defects. This is known to increase the resistivity of the material by approximately five orders of magnitude [14]. However, the trapping lifetime is affected by annealing due to the removal of point defects to around 500 fs – 1 ps, although it is partially compensated by the high cross section of precipitates for carrier capture [15].

It is clear that optimization of the LT-GaAs material must involve tuning the anneal parameters to obtain the best compromise between a high resistivity and a low lifetime, where both unique material properties are important for LT-GaAs device applications. Due to this belief, as well as the lack of experimental and theoretical work on "partially-annealed" LT-GaAs, a series of LT-GaAs samples annealed at different temperature was systematically characterized by XRD, TEM, TRPR and resistivity. The anneal temperature between the as-grown temperature (~200 °C) and 600 °C, where point defects and precipitates co-exist, is known as the "partially-annealed" regime. Furthermore, a model based on the effects of both point defects and precipitates is presented. The "two-trap" quantitative model is shown to successfully interpret the observed unusual trends of the measured results.

6.2 The two-trap model

There remains much debate regarding the type of traps responsible for the lifetime of LT-GaAs. According to *Gupta et al.* [9] and Wang *et al.* [16],

precipitates play no part in the trapping of carriers. Hence the concentration of antisite defects is solely responsible for the trapping lifetime, and the Shockley-Read-Hall (SRH) model [17] is used to relate the trapping lifetime to the concentration of antisite defects. However, Gregory *et al.* shows that the trapping lifetime, although it follows the SRH model initially as-grown, falls below the SRH prediction for annealed LT-GaAs material [18]. This is solid evidence that the trapping mechanism must be different for annealed material. The hypothesis that arsenic precipitates contribute towards the trapping of carriers corroborates with the findings by Kawasaki *et al.* [19] and Harmon *et al.* [20].

The two-trap model proposes to treat the point defects and precipitates as co-existing and independent entities, whereby the 'one-trap' SRH model must be modified to accommodate multiple trap types. According to the vacancy-assisted diffusion model proposed by Bliss *et al.* [21], the concentration of excess arsenic remains fairly constant throughout annealing because the migration of vacancies to voids reduces the diffusion coefficient of arsenic antisites. It is energetically more favorable for Ga atom to swap with V_{Ga} rather than for As atom. When the anneal temperature is maintained long enough for an equilibrium state to be achieved, the number density of point defects is given by:

$$N(T_A) = N_0 \exp\left[-\frac{\tau_V(T_A)}{\tau_{As}(T_A)}\right] \tag{6.1}$$

where N_0 is the as-grown defects number density, which is determined from the XRD parameter for as-grown material. τ_V and τ_{As} are the characteristic diffusion time of vacancy and antisite defects, respectively, which are both functions of the anneal temperatures, T_A [18].

At any given anneal temperature, the precipitate diameter, D_{ppt}, can be determined by [18]:

$$D_{ppt}(T_A) = D_{ppt}^0 + D_{ppt}^1 \exp\left(\frac{3T_A}{T_A^0}\right) \tag{6.2}$$

The exponential relationship in the function is consistent with the notion that precipitate diameter is determined by thermodynamic considerations. The mechanism for change in diameter of precipitates is Ostwald ripening, in which larger precipitates grow at the expense of many smaller ones as the anneal temperature increases, driven by the transport of material along the gradient of chemical potential [22]. The mechanism is also driven by a thermodynamic driving force to reduce the surface to volume ratio which lowers the interfacial energy [23].

From Eq. (6.1) and (6.2), $N(T_A)$ and D_{ppt} can be deduced by the conservation of the total arsenic atomic content. Assuming no loss of excess arsenic during annealing and little or no precipitation for as-grown material, the precipitate number density, N_{ppt} and the inter-precipitate spacing can be deduced. Based on the two-trap model, the derivation of carrier trapping lifetime is based on the assumption that both the point defects and precipitates are able to capture carriers independently, and in the latter case, with an effective cross-sectional function of the precipitate diameter [18]. The numerical model uses three different trapping mechanisms: trapping by antisite defects and precipitates are denoted as τ_1 and τ_2, respectively, and τ_3 for recombination across the band gap. The trapping times for τ_1 and τ_1 are given by the modified SRH model as:

$$\tau_1 = \frac{1}{\sigma v_{th}\left(N - n_1\right)} \tag{6.3}$$

$$\tau_2 = \frac{1}{\sigma_{ppt} v_{th} N_{ppt}} \tag{6.4}$$

The occupation of the point defect states, n_1, and the precipitate cross section, σ_{ppt}, is described by:

$$\frac{dn_1}{dt} = \frac{n}{\tau_1} - \frac{n_1}{\tau_2} - \frac{n_1}{\tau_3} \tag{6.5}$$

$$\sigma_{ppt} = \pi\left(\frac{D_{ppt} + D_{dep}}{2}\right)^2 \tag{6.6}$$

D_{dep} represents the extent of the depletion region and υ_{th} is the thermal velocity at room temperature. τ_3 is fixed at 50 ps, as typically measured in SI-GaAs [24].

Similarly, the bulk resistivity of as-grown or annealed LT-GaAs can be derived from the physical point defect and precipitate parameters. Carrier conduction in LT-GaAs can take place using different channels, depending upon the energy of the charge carriers. The hopping resistivity associated with antisite defects, ρ_{hop}, is given by [14]:

$$\rho_{hop} = \left(\frac{32\pi\alpha}{N}\right)^{\frac{1}{2}} \frac{kT}{e^2\delta} \exp\left(2.1\frac{\alpha^3}{N}\right)^{\frac{1}{4}} \tag{6.7}$$

where α is the inverse wavefunction decay distance, and δ is the hopping attempt frequency. The conduction contribution via tunneling between precipitates is negligible (i. e. associated resistivity is very high) as the spacing between precipitates is too large. The conduction band resistivity, ρ_{cb}, arises from the conventional scattering of carriers in the conduction band, as a result of the ionization of defects and thermal excitation. The conduction band resistivity, which is a function of the total occupation of the band, including intrinsic carriers, n_i, extrinsic carriers by ionized defects, n_e, and the photoexcited carriers, n, is given by [18]:

$$\rho_{cb} = \frac{1}{(n_i + n_e + n)e\mu_e} \tag{6.8}$$

6.3 Experimental procedure

In order to test the two-trap model, a series of LT-GaAs samples, annealed at different "partially-annealed" temperatures, were systematically characterized

by XRD, TEM, TRPR and resistivity tests. The LT-GaAs was grown by MBE onto undoped (001) semi-insulating (SI)-GaAs substrates. An epitaxial buffer layer of GaAs was grown at high temperature before a layer of 100 nm AlAs was grown to insulate the active LT epilayer from the conductive GaAs substrate. Subsequently, 1 μm of GaAs active layer was grown at a nominal temperature of between 200 and 230 °C at a rate of approximately 1 μm per hour, with the substrate temperature estimated using a thermocouple.

The samples were subsequently annealed *ex situ* by RTA under a nitrogen atmosphere to avoid oxidation, and in contact with SI-GaAs wafers to reduce arsenic loss. For each anneal, the annealer was stabilised at 150 °C for 30s before being ramped to the desired temperature over a 30s interval. The temperature was varied from sample to sample in 25 °C increments, covering the range between 250 °C and 600 °C. Once the annealing duration was achieved, the annealer was rapidly ramped back to room temperature with an inflow of N_2 gas. Ten-minute anneals were used throughout to ensure that quasi-equilibrium states were achieved. Because various defect types migrate at different rates, the samples were soak-annealed for a long period of time to stabilise defects against further anneal at increased temperatures [21]. Furthermore, this technique allows the precipitates to achieve equilibrium with the surrounding lattice at the given anneal temperature, meaning that the evolution of precipitates was governed by energetic, instead of kinetic, considerations [18].

In order to obtain the lifetime and resistivity parameters, we have measured the point defect and precipitate concentrations independently, using XRD measurements and TEM images, respectively. The XRD rocking curves were collected for each sample using a Bede model 200 double-axis x-ray diffractometer, referenced to a GaAs crystal and diffracted from the (004) plane of the LT-GaAs sample. The diffraction peak from the LT-GaAs layer was compared in each case to the corresponding Bragg maximum from the SI-GaAs substrate to generate the fitting parameter, $\Delta\theta$.

Since the As-As interatomic bond length exceeds that of the Ga-As, a positive strain is associated with both As_{Ga} and As_i defects. The net strain relative to the substrate may be measured using XRD and yield a useful parameter that can be used to characterise the total defect concentration present. The increased lattice parameter (strain) may be found from the peak separation of the LT-GaAs and GaAs substrate layers using:

$$n\lambda = 2a_0 \sin\theta_B \tag{6.9}$$

$$\frac{\Delta a}{a_0} = \frac{-\Delta\theta}{\tan\theta_B} \tag{6.10}$$

where a_0 is the unstrained lattice constant, 5.65 Å, and λ is the wavelength of the diffracted x-rays (1.54 Å for the CuK line). For diffraction from the (004) surface (n=4), the Bragg angle for GaAs, θ_B, is 33.15°. Liu *et al.* has demonstrated the linear correlation between the lattice strain using XRD and the As_{Ga} point defect concentration using near-infrared absorption spectroscopy [7]. This indicates that the As_{Ga} is the main source of lattice strain. The curve-fitting of the data yields:

$$\frac{\Delta a}{a_0} = 1.24\times10^{-23}[As_{Ga}] \tag{6.11}$$

For both annealed and as-grown LT-GaAs materials, the net strain may be measured using XRD, subsequently extrapolating the approximate As_{Ga} antisite defect concentration. Using the calibration found by Liu *et al.* gives [7]:

$$[As_{Ga}] = -5.9\times10^{17}\Delta\theta \text{ cm}^{-3} \tag{6.12}$$

where $\Delta\theta$ is the splitting parameter in units of arcseconds.

TEM images were used to characterize the mean diameter, spacing and number density of precipitates where these three physical parameters are sufficient to describe the precipitation process completely. Samples of an LT-GaAs wafer were annealed over a range of temperatures, and prepared for TEM imaging as described in Section 3.4 and 3.5. These specimens were examined with

conventional TEM and HRTEM using a JEOL 2010F field emission gun TEM operating at an accelerating voltage of 200 kV (Section 3.6).

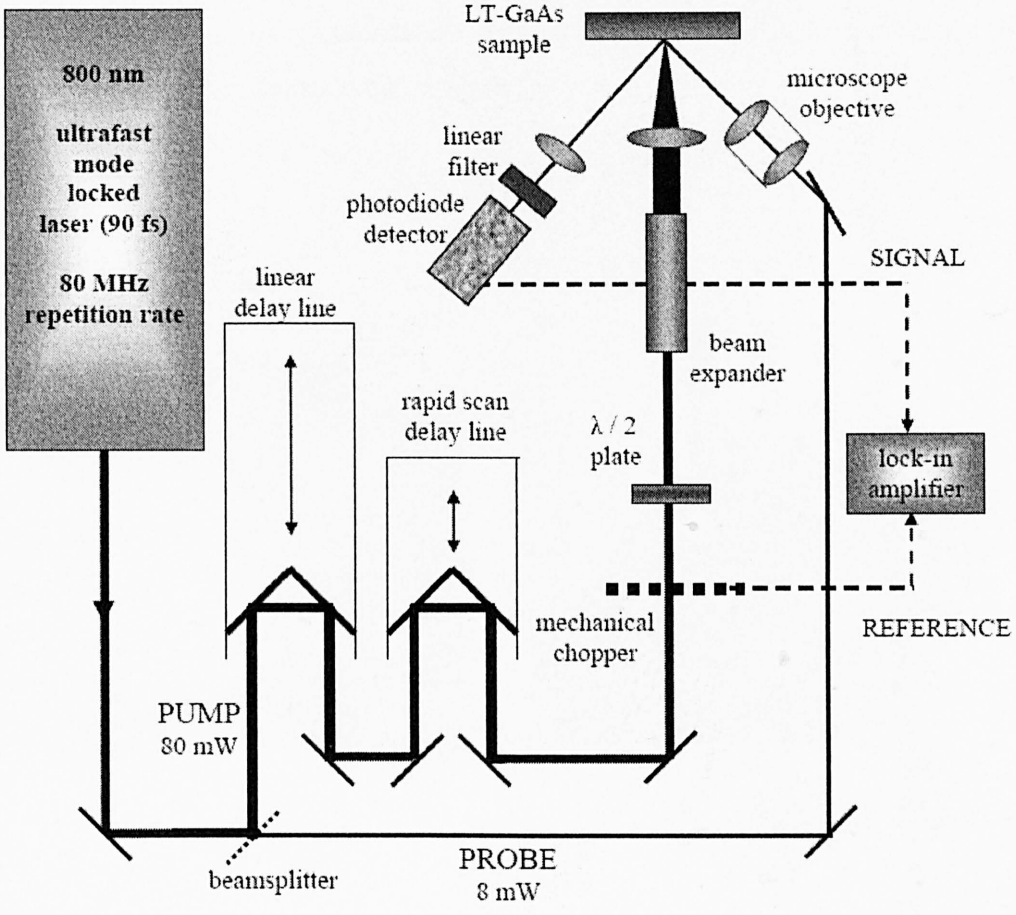

Fig. 6.1 Schematic diagram of the TRPR apparatus [25], including the femtosecond laser. The beam is divided at the beam splitter, with the pump beam passed through two time delay stages before being focussed onto the sample. The reflected probe beam is then detected using a photodiode detector.

The lifetime was measured, by I. S. Gregory *et. al.* from the University of Cambridge, with TRPR using 90 fs pulses from a Ti:Sapphire laser operating at 800 nm, as shown in Fig 6.1. The laser beam was divided using a beamsplitter, and an optical time-delay stage allowed a pump-probe

measurement to be collected, indicating the carrier density as a function of time. The lifetime was then derived in each case by fitting to the exponential decay of the signal. The accuracy of such measurements is dependent upon the wavelength and power of the exciting laser, as well as the correct interpretation of various artifacts that can arise. However, the technique provides valuable and quantitative estimates for the lifetime, which are sufficient for comparative measurements.

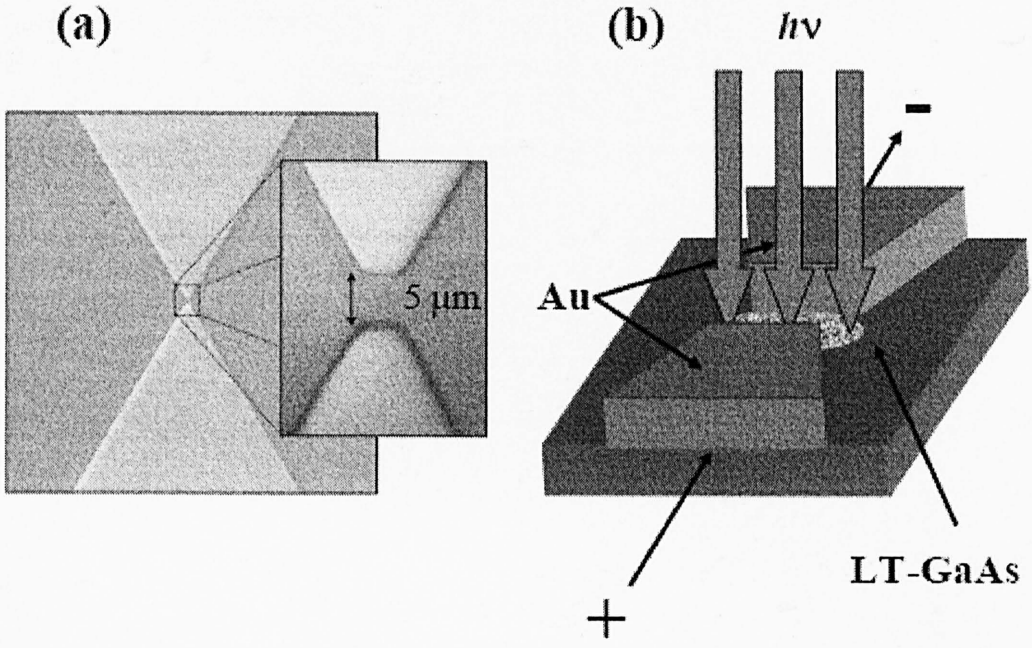

Fig. 6.2 The standard planar two electrode device adopted to assess the resistivity of the LT-GaAs wafers: (a) micrographs, and (b) schematic illustration. [26]

The resistivity was characterized through measurements of the two-terminal resistance of test devices, each with a 5 μm × 5 μm photoconductive gap as shown in Fig 6.2 (measured by I. S. Gregory *et. al.*). The device consists of two planar metal electrodes of 400 nm thickness (the contact resistance is negligible), lithographically patterned onto the surface of the material under test. A value for the resistance was derived using a source-measure unit in the ohmic (low bias) limit.

6.4 Results and discussion

In this section, the experimental results are compared with the model predictions. Using the aforementioned experimental techniques, six observable parameters are measured: the XRD peak separation, the precipitate mean diameter, the number density and spacing of the precipitates, the carrier lifetime and the resistivity. In each plot, the points correspond to individual experimental measurements, with the solid curves representing the model's predictions.

6.4.1 XRD results

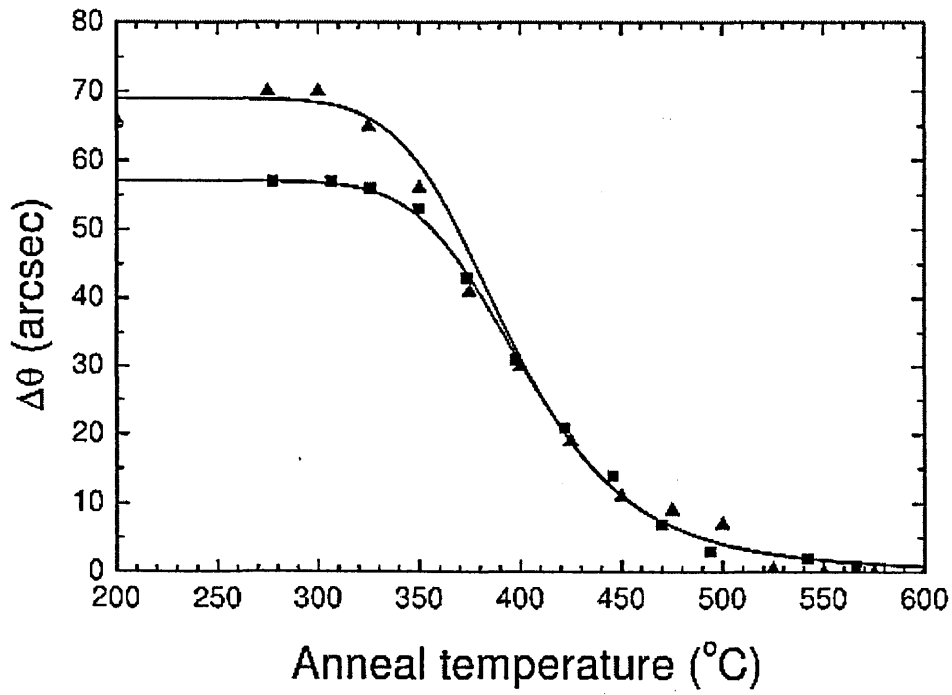

Fig 6.3 Plots of the XRD peak separation as a function of the anneal temperature. Experimental data from two LT-GaAs samples are plotted, with the solid line curves for the corresponding fits from the model [18].

The XRD spectra of two separately grown LT-GaAs wafers were evaluated for anneal temperatures across the range between 250 to 600 °C. The

peak separation between the SI-GaAs substrate (used to define $\Delta\theta=0$) and the LT-GaAs epilayer, $\Delta\theta$, is plotted as a function of the anneal temperature as shown in Fig 6.3. At temperatures below 300 °C, there is no significant removal of point defects. However, as the temperature increases from 350 °C to 450 °C, the LT-GaAs lattice parameter relaxation accelerates, as the majority of point defects are being removed. Beyond this, further increment of temperature results in little lattice parameter relaxations, with total extinction achieved at approximately 550 °C. This means that large excess of As_i and As_{Ga} is diminished dramatically, since these defects migrate to form arsenic precipitates [27, 28].

The simulated model derived from the diffusion lifetime functions from Eq. (6.1) is overlaid upon the experimental data points in Fig. 6.3 for the two LT-GaAs wafers. The fit is accurate across the entire range of anneal temperature. From Fig. 6.3, the original concentration of point defects in as-grown LT-GaAs varies between different wafers as a result of a small temperature or parameters aberration during growth. Nonetheless, the curves converge upon annealing and intersect at approximately 400 °C. This observation is probably attributed to the lattice vacancies acting to normalise the diffusivity of the antisite defects (vacancy-assisted diffusion) [14].

For most MBE chambers, measurement and control of the substrate temperature during low-temperature growth is extremely difficult, since the instruments will be operating beyond their designed temperature range. As a result, LT-GaAs wafers grown under nominally similar conditions are proven somewhat inconsistent, as shown in Fig. 6.3, where two separate LT-GaAs wafers grown under nominally similar conditions have dissimilar numbers of incorporated defects. However, since the annealing temperature can be accurately controlled, the LT-GaAs consistency may be improved by adopting this anneal process. Furthermore, as the anneal temperature increases, the concentration of antisites decreases whilst the total excess arsenic content is generally maintained, the diffusion of antisite defects produces arsenic precipitates during annealing.

6.4.2 TEM results

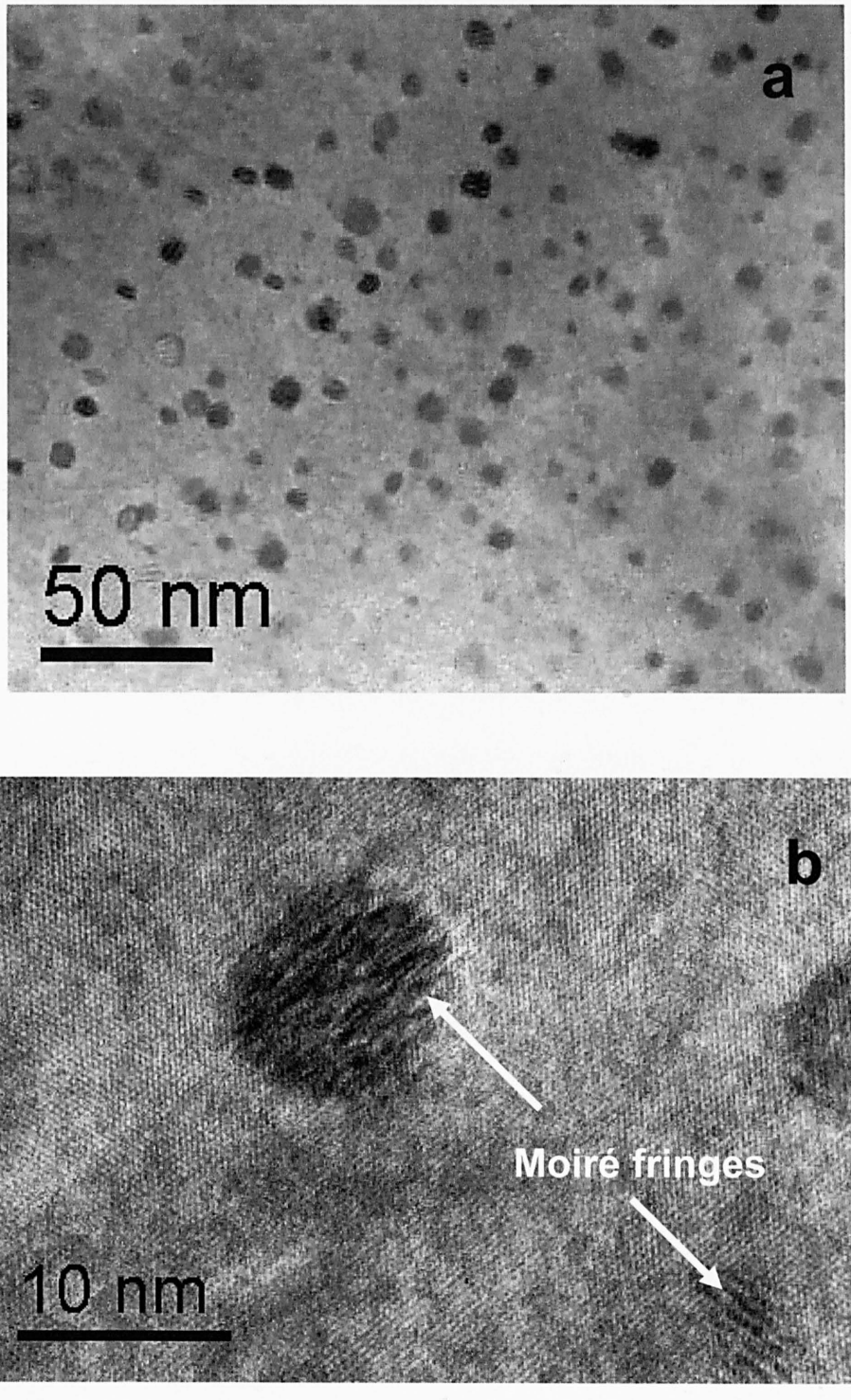

Fig 6.4 (a) Low magnification BF TEM image and (b) HRTEM image of a region from a LT-GaAs annealed at 600 °C.

Fig 6.4 (a) shows a BF TEM micrograph of a region from a LT-GaAs epilayer annealed at 600 °C. The elemental arsenic precipitates are shown as spherical particles with dark contrast [29]. The distribution of precipitates appears to be relatively uniform. The (200) BF TEM image was found to give excellent precipitate-to-matrix contrast. It is clear that a redistribution of excess arsenic has occurred during the annealing process, promoting the migration of point defects (excess As) to arsenic precipitates. Despite the presence of large numbers of precipitates, no dislocation loops were found in the sample. Fig. 6.4 (b) illustrates a HRTEM image of LT-GaAs region annealed at 600 °C, showing hexagonal crystalline arsenic precipitates. The overlapping of lattice fringes between the GaAs matrix and the arsenic precipitates results in Moiré fringes in the HRTEM images.

Compared to arsenic precipitates in higher temperature annealed samples, the HRTEM image of LT-GaAs annealed at 350 °C in Fig. 6.5 (a) shows that the arsenic precipitates has less well-defined boundaries with the surrounding GaAs matrix. Furthermore, the local regions in the LT-GaAs matrix appear amorphous-like. We tentatively attribute the phenomenon to the agglomeration of arsenic point defects, similar to the GINA structure grown also at 350 °C in Section 5.3.5. The diffraction pattern in Fig. 6.5 (b) shows that the specimen has good crystallinity.

A series of TEM images of LT-GaAs were obtained for anneal temperatures across the range between 250 to 600 °C, as shown in Fig. 6.6. The precipitates appear to crystallize between annealing temperatures 475 to 525 °C. The mean size, spacing and number density of precipitates as a function of annealed temperature were evaluated. The size of precipitates was measured directly from the from HRTEM images. The number density of precipitates, D_{ppt}, is the number of precipitates per unit volume V (where V is the product of the sampled area and the average sampled area thickness). An electron energy-loss spectroscopy (EELS) spectrum is used to measure the average thickness, t, as described in Section 3.6.3.

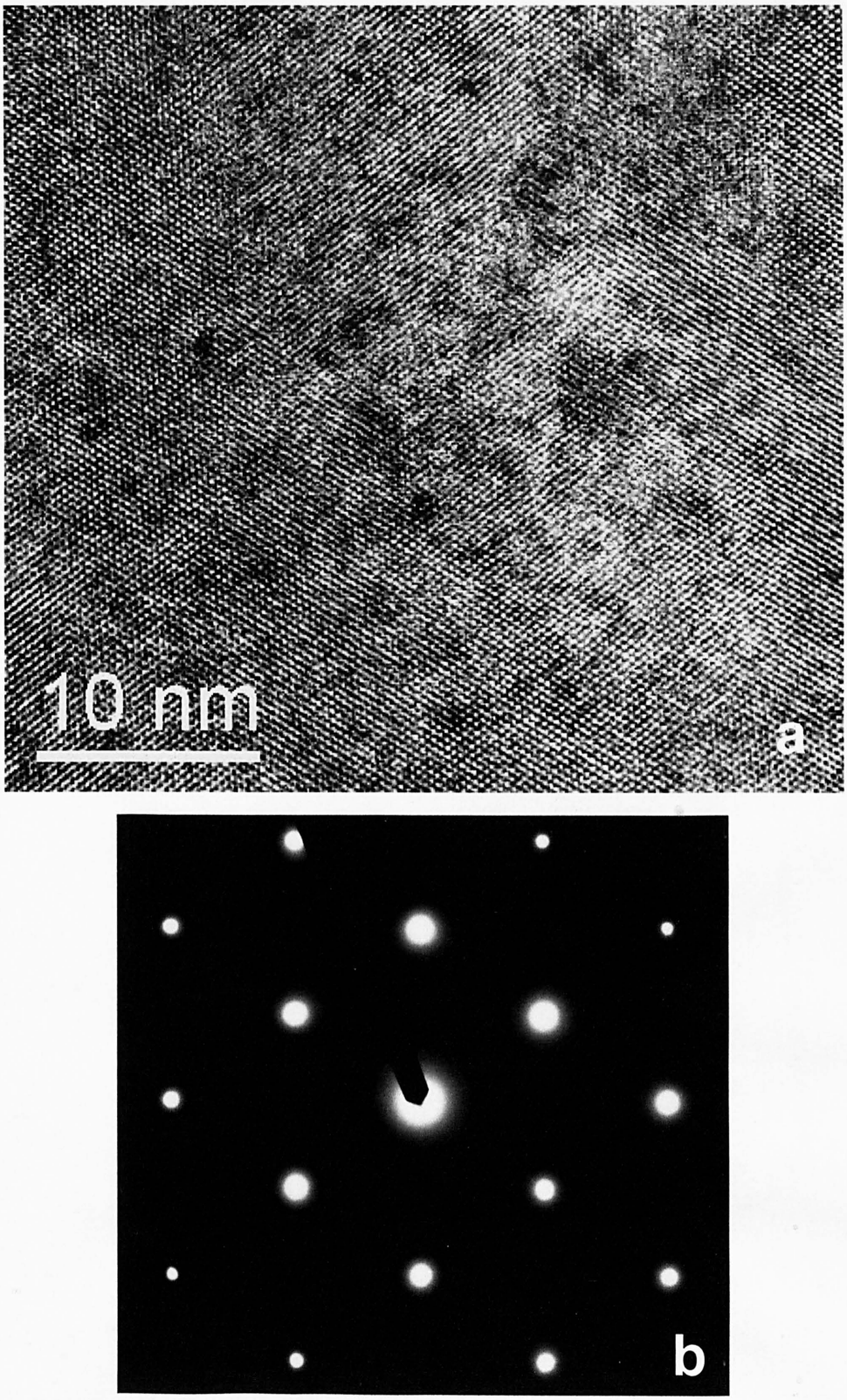

Fig. 6.5 (a) HRTEM image and (b) selected area diffraction pattern of a region from a LT-GaAs annealed at 350 °C.

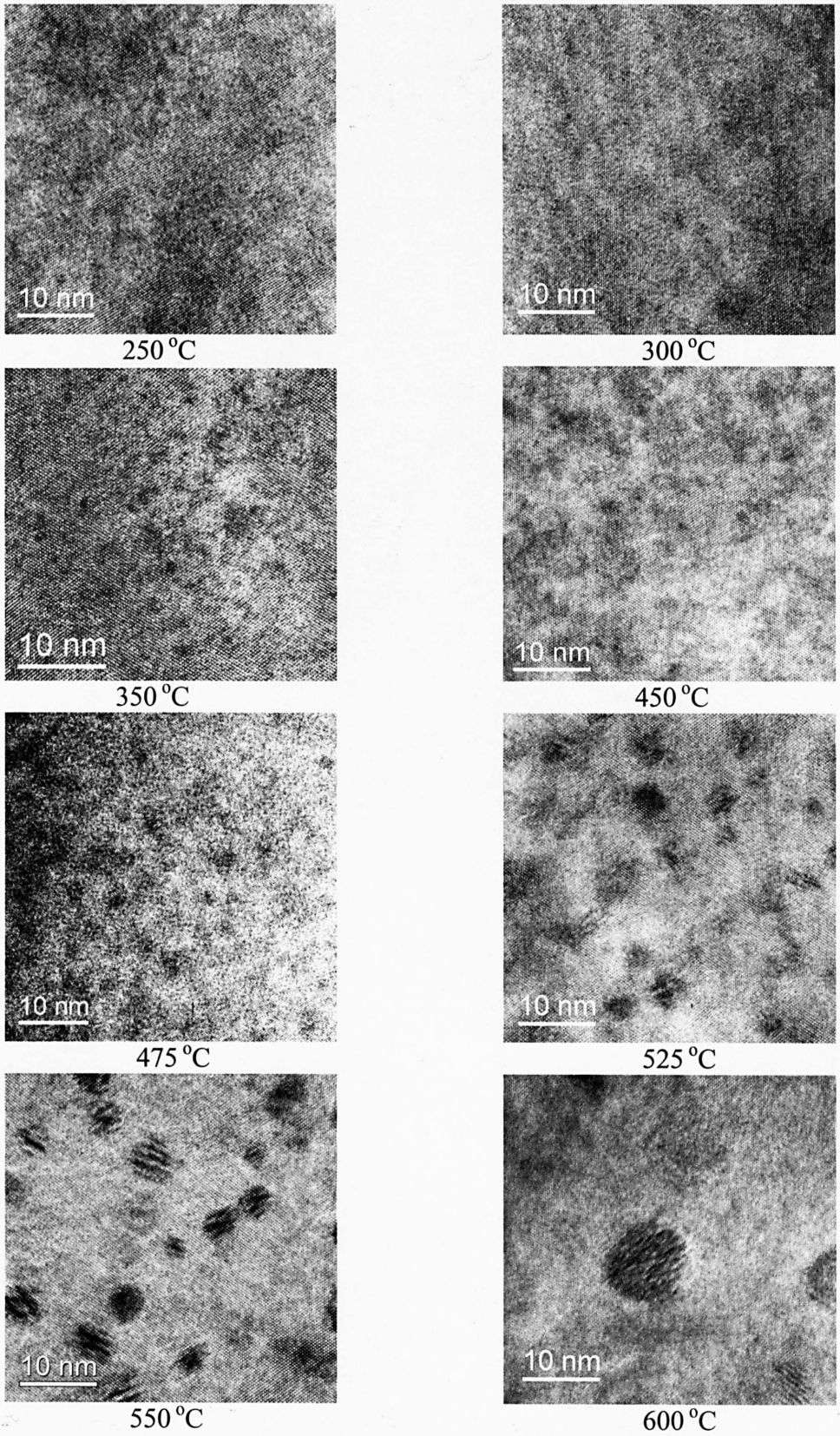

Fig. 6.6 HRTEM images of LT-GaAs annealed between 250 - 600 °C.

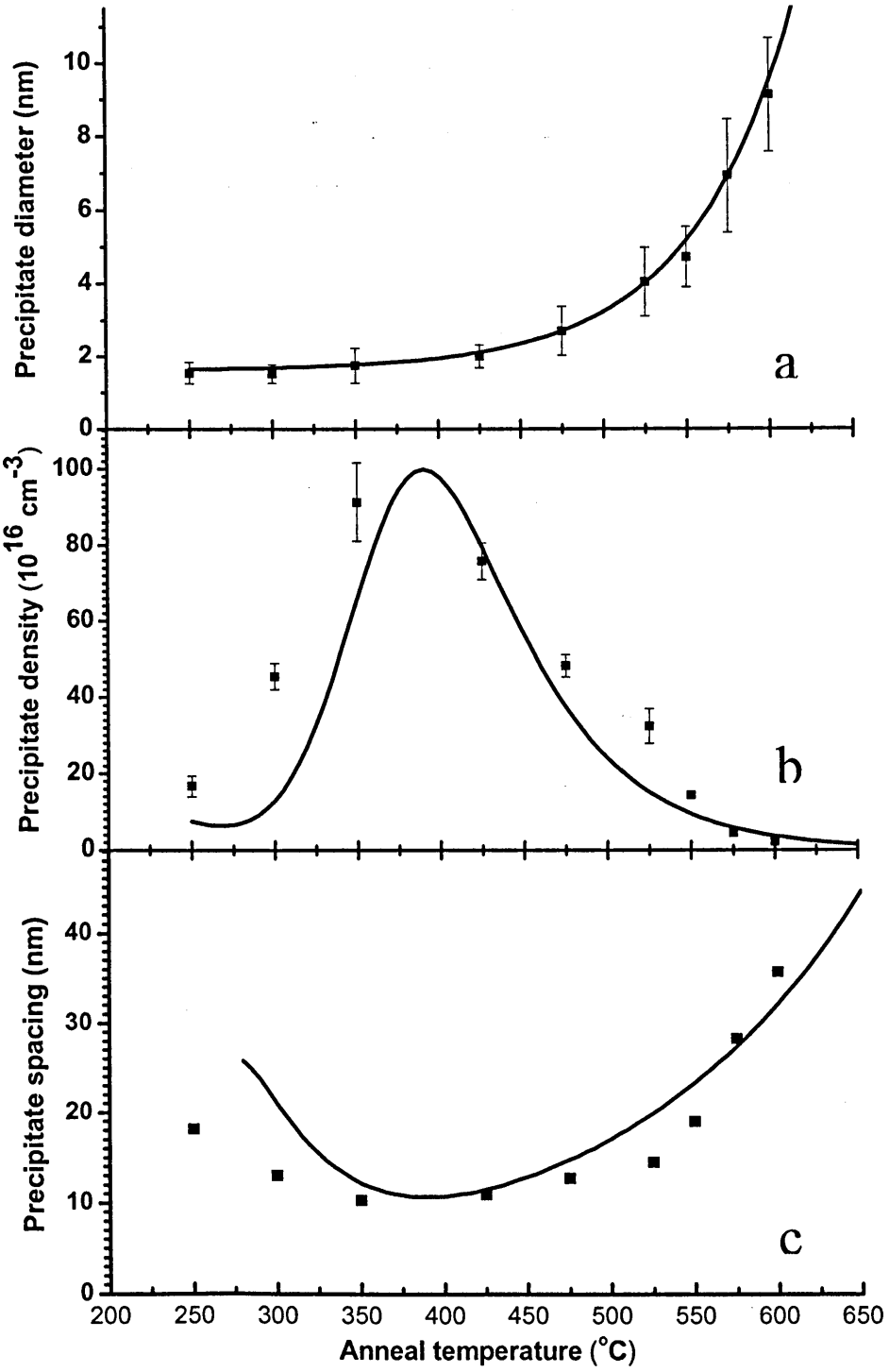

Fig. 6.7 Plots of the measured parameters from TEM images: (a) mean precipitate diameter, (b) mean precipitate number density and (c) mean precipitate spacing, as functions of the anneal temperature. The points are derived from TEM data. The curves plotted for the diameter, number density and spacing of the precipitates are derived using the model [18].

Fig. 6.7 shows the evolution of the equilibrium mean precipitate diameter, number density and spacing as functions of the anneal temperature. In Fig. 6.7 (a), the mean diameter increases exponentially from 1.5 nm at 250 °C to 9.1 nm at 600 °C. This compares well with the exponential growth curve, deduced from the predictions of Eq. (6.2), where D_{ppt}^{0}, D_{ppt}^{1} and T_A^{0} are fitting parameters obtained from the data. These parameters appear to adopt similar values for different LT-GaAs wafers with similar growth conditions but different initial point defect concentrations. One interesting observation is found where the size of precipitates fluctuates more as the anneal temperature increases. This is probably due to Ostwald ripening, in which the larger precipitates grow at the expense of the smaller ones as the temperature increases.

In Fig. 6.7 (b), the number density of precipitates increases to a maximum value between 350 and 425 °C, before falling to much lower values, in good agreement with the model. Initially, between 250 and 400 °C, the number density of precipitates increases rapidly with increases in anneal temperature. This observation suggests that excess arsenic from point defects condense to form small precipitates, stabilizing when the point defect concentration is depleted. However, larger precipitate diameters are energetically preferred at higher anneal temperature, thus reducing the number density as the smaller precipitates dissolve to provide material for the larger ones to grow. Whilst the formation of many small precipitates is kinetically favored, large precipitates are thermodynamically favored because their greater volume to surface area ratio, represent a lower energy state [30]. Finally, Fig. 6.7 (c) shows the corresponding mean precipitate spacing, again, in good agreement with the model.

Assuming spherical precipitates, the volume fraction of arsenic precipitates Γ are calculated using the measured precipitate volume, V_{ppt}, and number density of precipitates, N_{ppt},:

$$\Gamma = V_{ppt} \times N_{ppt} \times \frac{N_{As}}{N_{GaAs}} \qquad (6.14)$$

where N_{As} and N_{GaAs} are the number of arsenic atoms and GaAs molecules per unit volume, respectively. From Fig. 6.8, the increasing trend of the volume fraction of arsenic precipitates with increasing anneal temperature is apparent. Unexpectedly, comparisons between TEM and XRD data indicate that the precipitates contain far more arsenic than can be accounted for by the accretion of the antisite defects alone. This observation is made more surprising by the likely loss of arsenic from the crystal surface during anneal. One plausible hypothesis is that a significant proportion of the excess arsenic is incorporated as interstitial point defects [31] (this could be as high as 60 %, according to Yu *et al.* [2]), which are not thought to cause significant strain.

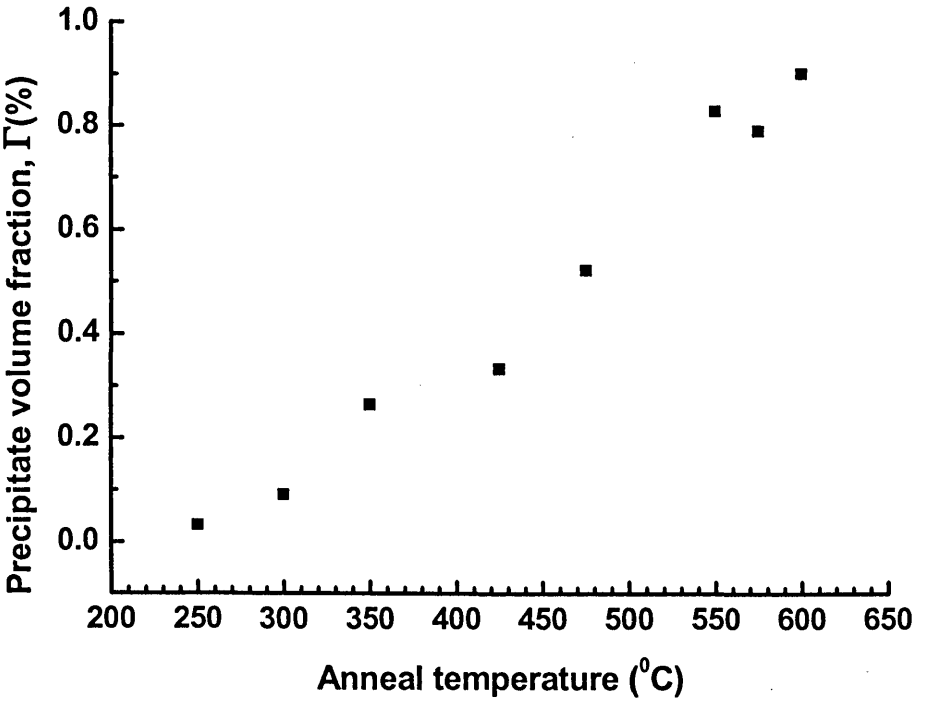

Fig. 6.8 Arsenic precipitate volume fraction as a function of anneal temperature. The data are obtained from TEM images.

Since the As_i defects are very much more mobile than the As_{Ga} defects, it is expected that they would diffuse to form precipitates at a much lower temperature than that required to cause significant migration of the As_{Ga}.

However, the presence and significance of this type of defect in LT-GaAs is still under dispute [9]. Another possibility is the presence of small arsenic precipitates, clusters and complexes even in the as-grown state. This is consistent with extrapolating the exponential curve in Fig. 6.7 (a) back to the growth temperature, which suggests that precipitates up to 1.6 nm are probably stable at the substrate growth temperature of ~200 °C.

6.4.3 Time resolved photoreflectance results

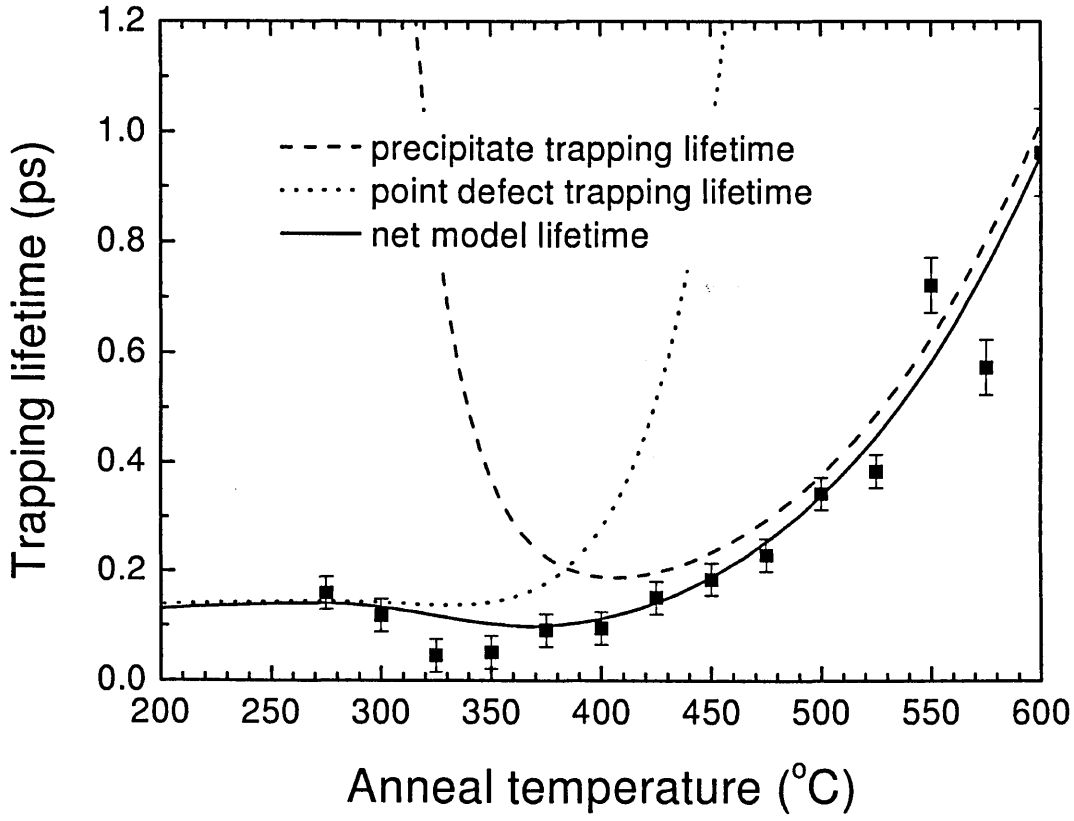

Fig. 6.9 Plots of both modeled and experimental trapping lifetimes for an LT-GaAs wafer as a function of the anneal temperature. The two components of the lifetime, τ_1 and τ_2, shown as dotted and dashed curves respectively, representing the trapping lifetimes owing to the point defects and precipitates. The net trapping time is shown as a solid curve, and is derived from the sum of both the trapping rates [18].

The carrier trapping lifetime, τ, is the time required for the concentration of excited carriers to fall to 1/e of its initial value. Fig. 6.9 shows the equilibrium 1/e trapping lifetime for LT-GaAs as a function of the anneal temperature. The dotted curve shows the predicted lifetime with respect to the trapping by the antisite point defects, τ_1. As might be expected from the XRD measurements, this rapidly increases beyond 350 °C as the point defects are eliminated. The dashed curve indicates the trapping lifetime with respect to the precipitate trapping, τ_2. In this case, the attractive potential is provided not by a point positive charge (as in the case of an antisite defect) but by the depletion region surrounding the elemental arsenic precipitate. This lifetime is seen to decrease as both the trapping cross section (precipitate diameter) and the number density of the precipitates increase owing to nucleation from clusters of point defects.

However, the subsequent increase in trapping lifetime occurs after 400 °C. One of the factors influencing this trend is the exponential increment of the arsenic precipitate volume to surface ratio due to the formation of larger precipitates, at the expense of smaller ones. Furthermore, the Ostwald ripening process causes a net decrease in the precipitate number density. The overall lifetime based on the two-trap model is plotted as a solid curve in Fig. 6.9. The measured carrier lifetimes are in good agreement with the modeled data over the temperature range shown. The lifetime decreases to a minimum of ~50 fs at an anneal temperature of 325 °C, before rising rapidly as the temperature is increased further.

The above is evidence that macroscopic precipitates play a major role in the trapping process, and dominate the trapping rate at higher annealing temperature. Although contrary to the findings of Gupta *et al.* [9], the trapping process of precipitates is in agreement with Harmon *et al.* [20]. Nonetheless, the lifetimes observed in unannealed or low temperature annealed material may be explained by the trapping of carriers by ionized antisite defects. The result clearly shows that partially-annealed material exhibits carrier trapping by both the remaining antisite defects and precipitates, hence the two-trap model.

6.4.4 Resistivity test

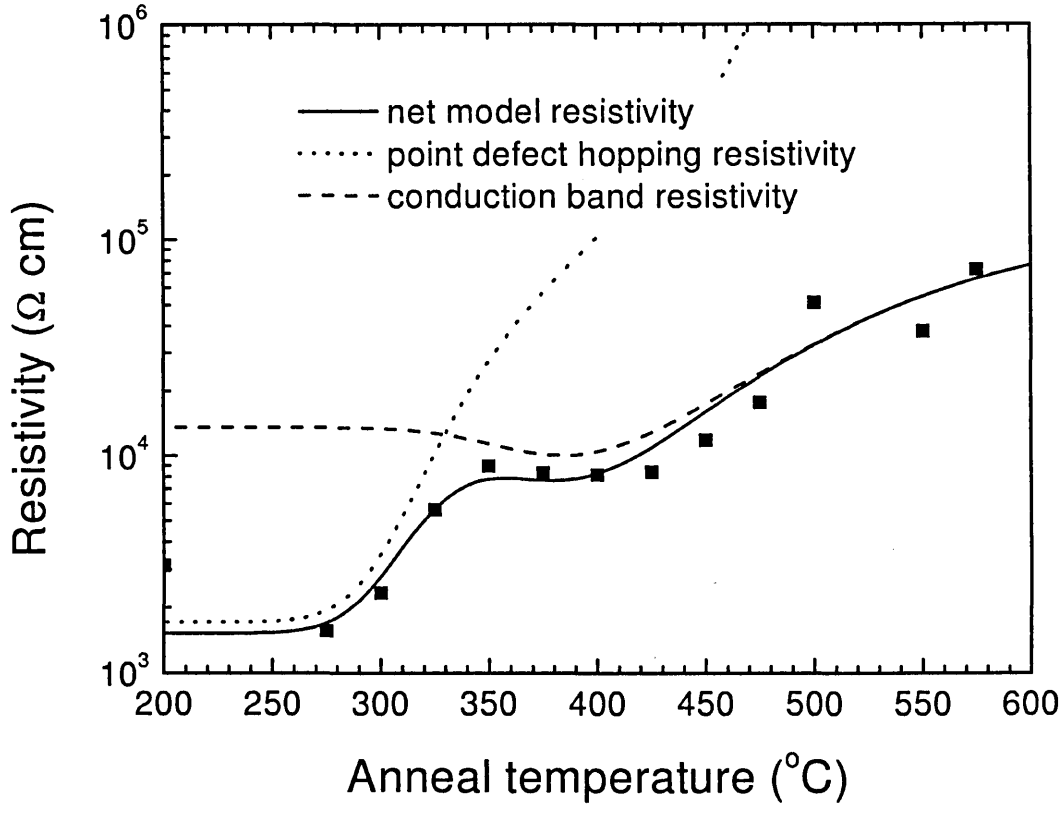

Fig. 6.10 The bulk resistivity plotted as a function of the anneal temperature showing both experimental data and predictions from the model. Again, the model data may be shown in terms of the individual contributions from the conduction band scattering, ρ_{cb}, (dashed curve), and hopping in the point defects, ρ_{hop} (dotted curve). Significantly, the resistivity plateau between 325 and 400 °C is predicted by the model [18].

Fig. 6.10 shows the measured and modeled resistivity as a function of the anneal temperature. The modeled resistivity of the material is plotted in terms of its two components: the hopping resistivity and the conduction band resistivity. The hopping resistivity (dotted line) associated with the point defects increases

tremendously at around 275 °C, once significant depletion of the antisite defects occurs. The conduction band resistivity (dashed line) is a function of the total occupation of the band, including intrinsic carriers and extrinsic carriers supplied by ionized donors.

The conduction band resistivity initially decreases with anneal temperature, contributed by the increased carrier mobility. However, this effect is more than offset by the increase in size of the precipitates following the increase of anneal temperature, which expands the depletion regions, causing a substantial increase in the conduction-band resistivity [14, 32]. Furthermore, subsequent increases in anneal temperature result in the removal of donors. The net resistivity, shown by the solid curve, is seen to increase monotonically with temperature, reaching a plateau in the range 350-425 °C after rising by approximately one order of magnitude. A further rise in temperature leads to an exponential increase without limit, giving another order of magnitude at 600 °C. It is worth noting that parallel conduction through the GaAs buffer layer can be neglected as the resistivity of the SI-GaAs is more than two orders of magnitude greater than LT-GaAs [14].

6.5 Conclusion

Significant changes occur in both the carrier lifetime and the resistivity even for annealing temperatures as low as 275 °C, where no point defect migration is activated. During the annealing process, the average precipitate size increases as the Ostwald ripening mechanism is activated. At low annealing temperatures, this is able to occur even before the migration of antisite defects is activated. Thus, only precipitates can qualitatively explain the changes in the lifetime and resistivity for sub-300 °C anneal temperatures. Furthermore, the continued evolution of both the lifetime and the resistivity at temperatures beyond those at which all of the point defects are eliminated is evidence for the participation of precipitates in the carriers trapping mechanism.

In summary, a semi-quantitative model has been introduced to explain the hitherto anomalous annealing characteristics of LT-GaAs. Some of the experimental trends (namely the lifetime minima and the resistivity plateau) may be considered anomalous because they have been repeatedly observed elsewhere, but cannot be explained by simple diffusion of the point defects, or by the SRH theory. However, the two-trap model is able to explain the observed minimum in carrier lifetime, together with a plateau in the bulk resistivity. The mechanism depends upon a simultaneous presence and influence of both point defects and precipitates. An understanding of these processes in partially-annealed LT-GaAs would allow highly consistent material to be produced. Furthermore, a compromise between material properties of short carrier lifetime and high resistivity is realized in the partially-annealed temperature regime, between 350 to 450 °C.

6.6 References

[1] F. W. Smith, A. R. Calawa, C. L. Chen, M. J. Mantra, and L. J. Mahoney, IEEE Electron. Device Lett., **9** (1988) 77.

[2] K. M. Yu, M. Kaminska, and Z. Liliental-Weber, J. Appl. Phys., **72** (1992) 2850.

[3] D. C. Look, Thin Solid Films, **231** (1993) 61.

[4] K. Kaminska, E. R. Weber, Z. Liliental-Weber, R. Leon, and Z. Rek, J. Vac. Sci. Technol., **B7** (1989) 710.

[5] F. W. Smith, H. O. Le, V. Dialiuk, M. A. Hollis, A. r. Calawa, S. Gupta, M. Frankel, D. R. Dykov, J. Mourou, and T. Y. Hsiang, Appl. Phys. Lett., **54** (1989) 890.

[6] Z. Liliental-Weber, W. Swider, K. M. Yu, J. Kortright, F. W. Smith, and A. R. Calawa, Appl. Phys. Lett., **58** (1991) 2143.

[7] X. Liu, A. Prasad, J. Nishio, E. R. Weber, Z. Liliental-Weber, and W. Walukiewicz, Appl. Phys. Lett., **67** (1995) 279.

[8] K. A. McIntosh, K. B. Nichols, S. Verghese, and E. R. Brown, Appl. Phys. Lett., **70** (1997) 354.

[9] S. Gupta, M. Y. Frankel, J. A. Valdmanis, J. F. Whitaker, G. A. Mourou, F. W. Smith, and A. R. Calawa, Appl. Phys. Lett., **59** (1991) 3276.

[10] H. Yamamoto, Z. Q. Fang, and D. C. Look, Appl. Phys. Lett., **57** (1990) 1537.

[11] P. Grenier and J. F. Whitaker, Appl. Phys. Lett., **70** (1997) 1998.

[12] A. C. Warren, J. M. Woodall, J. L. Freeouf, D. Grischkowsky, M. R. Melloch, N. Otsuka, Appl. Phys. Lett., **57** (1990) 1331.

[13] S. Fleischer, C. D. Beling, S. Fung, W. R. Nieveen, J. E. Squire, J. Q. Zheng, and M. Missous, J. Appl. Phys., **81** (1997) 190.

[14] J. K. Luo, H. Thomas, D. V. Morgan, and D. Westwood, J. Appl. Phys., **79** (1996) 3622.

[15] P. A. Loukakos, C. Kalpouzos, I. E. Perakis, Z. Hatzopoulos, M. Logaki, and C. Fotakis, Appl. Phys. Lett., **79** (2001) 2883.

[16] H. H. Wang, J. F. Whitaker, A. Chin, J. Mazurowski, and J. M. Ballingall, J. Elec. Mater., **22** (1993) 1461.

[17] W. Shockley, W. T. Read, Phys. Rev., **87** (1952) 835.

[18] I. S. Gregory, C. M. Tey, A. G. Cullis, M. J. Evans, H. E. Beere, and I. Farrer, Phys. Rev. B., **73** (2006) 1.

[19] N. Kawasaki, T. Yoshimura, M. Tonouchi, M. Tani, K. Sakai, H. Katahama, Polycrystalline semicon. VII, Proc. Solid State Phenomena, **93** (2003) 367.

[20] E. S. Harmon, M. R. Melloch, J. M. Woodall, D. D. Nolte, N. Otsuka, and C. L. Chang, Appl. Phys. Lett., **63** (1993) 2248.

[21] D. E. Bliss, W. Walukiewicz, and E. E. Haller, J. Electron. Mater., **22** (1993) 1401.

[22] W. Ostwald, Z. Phys. Chem., **37** (1901) 385.

[23] http://www.chemicool.com/definition/ostwald_ripening.html

[24] I. S. Gregory, Thesis (Ph.D.), University of Cambridge, Semiconductor Physics Group, Cavendish Laboratory (2005), p. 134.

[25] I. S. Gregory, Thesis (Ph.D.), University of Cambridge, Semiconductor Physics Group, Cavendish Laboratory (2005), p. 100.

[26] I. S. Gregory, Thesis (Ph.D.), University of Cambridge, Semiconductor Physics Group, Cavendish Laboratory (2005), p. 106.

[27] M. R. Melloch, N. Otsuka, J. M. Woodall, A. C. Warren, and J. L. Freeouf, Appl. Phys. Lett., **57** (1990) 1531.

[28] Z. Liliental-Weber, A. Claverie, J. Washburn, F. Smith, and A. R. Calawa, Appl. Phys. A, **53** (1991)141.

[29] A. G. Cullis, P. D. Augustus, D. J. Stirland, J. Appl. Phys., **51** (1980) 2556.

[30] R. Boistelle, and J. P. Astier, 1988. J. Cryst. Growth, **90** (1988) 14.

[31] N. F. Chen, Y. T. Wang, H. J. He, L. Y. Lin, Jpn. J. Appl. Phys., **35** (1996) L1238.

[32] A. C. Warren, J. M. Woodall, P. D. Kirchner, X. Yin, F. Pollak, M. R. Melloch, N. Otsuka, and K. Mahalingam, Phys. Rev. B, **46** (1992) 4617.

Chapter 7

Conclusions and Outlook

7.1 Conclusions

This work has demonstrated the use of the JEOL JEM-2010F FEGTEM in the compositional and structural analysis of various III-V semiconductor material systems. Various TEM imaging techniques, such as CTEM, STEM, and HRTEM have been utilized to investigate the interface sharpness, the morphological and structural properties, and the defect of the materials. EFTEM imaging has been shown to provide excellent compositional two-dimensional maps. Indeed, the quality of the TEM images is heavily influenced by the quality of the sample preparation process. The cross-sectional TEM specimens, with [110] surface normal orientation, were thinned to electron transparency by conventional mechanical polishing followed by Ar^+ ion milling at 5 kV beam energy and grazing incident angles. In order to minimize radiation damage and contamination, the thinned samples were finally transferred to a low-energy ion beam miller operating at ~200 V.

In **Chapter 4**, the effects of the InAlAs-InGaAs combination on the structural properties of InAs QDs were systematically investigated with different InAlAs-InGaAs capping layer thicknesses. A HAADF STEM Z-contrast image of the InAs QD heterostructure indicated significant elemental segregation in the InAlAs overgrowth layer where the aluminium adatoms were separated from the indium adatoms, as well as showing a significant reduction of Al concentration on top of the QDs. This finding was validated by EFTEM aluminium elemental mapping which indicated much reduced Al concentration at the apex of the QD. These observations showed that the Al adatoms have migrated from the apex to the periphery of each QD. Furthermore, the HAADF STEM images showed an increase of InAlAs capping layer thickness resulting in a corresponding

significant increase in the height of QDs. Based on the findings, a growth mechanism model based on surface chemical potential effects was proposed. Due to the enhanced In segregation within the InAlAs overgrowth layer, there were more indium atoms on the surface of the capping layer between InAs islands compared with the surface of an InGaAs capping layer. In effect, the surface chemical potential gradient between the QDs and the capping layer was decreased, resulting in a suppressed detachment rate of In atoms from the InAs QDs to the capping layer surface. The PL intensity was shown to increase by a factor of 450 as the thickness of InAlAs capping layer was increased from 1.5-nm to 6.0-nm. This indicated that a thicker InAlAs capping layer has increased the confinement of carriers in QDs and hence suppressed the thermal excitation of carriers from the InAs QDs.

The optical and structural properties of near-1.55 μm GINA/GaAs MQW heterostructures grown at 350, 375, and 400 °C were investigated as described in **Chapter 5**. The room temperature PL emission wavelength was blueshifted slightly from 1.6-μm to 1.55-μm as the growth temperature was decreased from 400 °C to 350 °C. This is probably caused by the In-Ga interdiffusion effects at the interfaces of the GINA/GaAs MQWs. More importantly, the PL intensity for the sample grown at 375 °C was 4 times stronger than that of the sample grown at 350 °C and 60 times stronger than that of the sample grown at 400 °C. This indicates that the growth temperature window resulting in good optical efficiency of GaInNAs MQWs is much narrower than for traditional InGaAs MQWs. From the HR-XRD measurements, the satellite peaks from a GINA MQW grown at 375 °C was much narrower and more pronounced in intensity than for the other samples, thus indicating better crystallinity. Both the CTEM and HAADF STEM images of GINA MQW samples grown at 350 and 375 °C have shown good heterostructure planarity, whereas the sample grown at 400 °C exhibited morphological instabilities with threading dislocations within the wells. At 400 °C growth temperature, the configuration of nearest-neighbour bonds for the GINA QW is adjudged to be driven by maximizing the cohesive bond energy, ie. Ga-N + In-As, which caused higher epitaxial strain energy in comparison with the

Ga-As + In-N configuration. Hence, the resulting elastic strain energy accumulated during growth causes compositional modulation and surface roughness. The HRTEM images of samples grown at 350 and 375 °C have shown that the former yielded a higher concentration of point defect agglomerates.

In **Chapter 6**, a semi-quantitative two-trap model has been introduced to explain the hitherto anomalous annealing characteristics of LT-GaAs. The two-trap model proposed to treat the point defects and precipitates as co-existing and independent entities. Based on the two-trap model, both the carrier trapping lifetime and bulk resistivity are derived independently from the physical point defects and precipitates. In order to test the model, a series of LT-GaAs samples, annealed at different temperatures, were systematically characterized by XRD, TEM, TRPR and resistivity tests. The approximate As_{Ga} antisite defect concentration was extrapolated from the net strain measured using XRD. As the anneal temperature was increased, the diffusion of antisite defects and their incorporation into arsenic precipitates resulted in a reduction of antisite defect concentration. It was initially thought that different samples would exhibit different concentrations of point defects in as-grown LT-GaAs. However, XRD observations showed that the point defect concentration curves converged and intersected at the anneal temperature of 400 °C. The TEM images of the LT-GaAs samples were employed to characterize the mean precipitate diameter, spacing and number density, and the results were shown to be in good agreement with the two-trap model. However, it is observed that the arsenic precipitates contain far more arsenic than can be accounted for by the accretion of antisite defects alone. One plausible explanation is that a significant proportion of excess arsenic was incorporated as interstitial point defects, which are not thought to cause significant strain. The other possibility is the presence of small arsenic precipitates even in the as-grown state. The TRPR experiment has shown that the carrier lifetimes are in good agreement with the model, with the trapping by precipitates playing a major role. The resistivity test has shown that the overall resistivity, which is influenced by the hopping resistivity and

conduction band resistivity, increased monotonically with anneal temperature until reaching a plateau between 350 °C and 425 °C, followed by a further rise in resistivity with anneal temperature.

7.2 Suggestions for future work

Although TEM is an essential tool for structural analysis for semiconductor materials, the conventional method of specimen preparation is inflexible and slow (up to a week per sample). With the advent of the focused ion beam (FIB) as a TEM specimen preparation tool, the technology enables fast site-specific milling with high precision down to the nanoscale [1]. Furthermore, uniformly thinned and parallel-sided TEM specimen lamella can be produced, thus eliminating the effects of wedge-shaped TEM specimens prepared by conventional specimen preparation. Thus, as the FIB significantly reduces the preparation time (typically 5 hours) without much sacrifice to the quality of TEM specimen, it is a serious contender as the sample preparation tool of choice.

Chapter 4

It is worth noting that a QD laser capped with a combined InAlAs-InGaAs capping layer was successfully produced [2]. Three dot-in-a-well (DWELL) layers were grown, with each DWELL capped with 1 nm of $In_{0.2}Al_{0.8}As$ followed by 5 nm of $In_{0.15}Ga_{0.85}As$. However, further optimization of the composition and thickness of InAlAs capping layer, and the number of DWELL layers are needed to improve the performance of the QD laser. Furthermore, it would be interesting to look at the structural and optical properties of QDs with InAlAs capping layers grown at a lower temperature, where Al adatoms are immobile and thus likely to accumulate at the apex of the QDs.

By substituting the InAlAs capping layer with AlAs capping layer, the theoretical surface chemical potential should be similar with that of GaAs capping layer, since both lattice parameters are quite similar. However, further

experiments are needed to observe the effect of AlAs capping layer on InAs/GaAs QDs. The introduction of Sb into the upper part or lower part of the InAlAs capping layer on InAs QDs should also be investigated. The unique surfactant effects of Sb might affect the mobility of the Al adatoms or the elemental segregation of the InAlAs capping layer; as a result, modifying the gradient of the surface chemical potential of InAs QDs and its capping layer.

Chapter 5

The PL intensity generally increases with the number of periods of MQW. Hence, it would be interesting to investigate the structural properties of an increased number of tensile-strained GINA/GaAs MQW and the number of periods of GINA/GaAs MQW grown before morphological instabilities occurs. Besides growth temperature, structural studies on a series of GINA/GaAs MQW grown at different V/III flux ratio and composition should also be investigated.

Recently, there is much interest in the addition of Sb to improve the quality of GINA QWs, and hence producing a novel material: InGaAsNSb for long wavelength optoelectronic devices [3]. The addition of Sb has been shown to significantly improve the epitaxial growth and optical properties of the GINA material system; and broadens the range of In and N composition alloys that can be grown [4]. However, this will increases the complexity of its characterization. Hence, it would be difficult to distinguish the distribution of elements unless EFTEM is employed. As most GINA/GaAs MQW were grown by MBE, it would also be interesting to investigate the structural properties of the heterostructure grown by MOCVD.

Chapter 6

It may be noted that very few attempts have been made to relate the number and the type of point defects to the growth temperature. Furthermore, there are many ambiguities with the quoted number of certain point defects. For

example, the arsenic interstitial concentration has been given from zero [5] to 60 % [6]. As a result, alternative experimental techniques have to be employed to identify the different defect types. The employment of aberration-corrected SuperSTEM in the Daresbury Laboratory, UK, with computer simulated images might be able to identify qualitatively and quantitatively the concentrations of vacancies, antisites and interstitials separately.

Specimen heating by TEM electron beams might be a problem for the analysis of LT-GaAs as it promotes the migration of point defects thus promoting arsenic precipitation. Therefore, the use of TEM cold-stage sample holder would be encouraged for future works on LT-GaAs. On the other hand, a modified hot-plated TEM sample holder can be employed in order to observe *in situ* the migration of point defects, as well as the Ostwald ripening process during annealing. However, possible out-diffusion of arsenic might severely affect the UHV TEM column.

7.3 References

[1] S. Reyntjens and R. Puers, J. Micromech. Microengn., **11** (2001) 287.

[2] I. R. Sellers, H. Y. Liu, M. Hopkinson, D. J. Mowbray, and M. S. Skolnick, Appl. Phys. Lett., **83** (2003) 4710.

[3] X. Yang, J. B. Heroux, L. F. Mei, W. I. Wang, Appl. Phys. Lett., **78** (2001) 4068.

[4] J. S. Harris, Jr., S. R. Bank, M. A. Wistey and H. B. Yuen, IEE Proc.-Optoelectron., **151** (2004) 407.

[5] X. Liu, A. Prasad, J. Nishio, E. R. Weber, Z. Liliental-Weber, and W. Walukiewicz, Appl. Phys. Lett., **67** (1995) 279.

[6] K. M. Yu, M. Kaminska, and Z. Liliental-Weber, J. Appl. Phys., **72** (1992) 2850.